



저작자표시-비영리-변경금지 2.0 대한민국

이용자는 아래의 조건을 따르는 경우에 한하여 자유롭게

- 이 저작물을 복제, 배포, 전송, 전시, 공연 및 방송할 수 있습니다.

다음과 같은 조건을 따라야 합니다:



저작자표시. 귀하는 원저작자를 표시하여야 합니다.



비영리. 귀하는 이 저작물을 영리 목적으로 이용할 수 없습니다.



변경금지. 귀하는 이 저작물을 개작, 변형 또는 가공할 수 없습니다.

- 귀하는, 이 저작물의 재이용이나 배포의 경우, 이 저작물에 적용된 이용허락조건을 명확하게 나타내어야 합니다.
- 저작권자로부터 별도의 허가를 받으면 이러한 조건들은 적용되지 않습니다.

저작권법에 따른 이용자의 권리는 위의 내용에 의하여 영향을 받지 않습니다.

이것은 [이용허락규약\(Legal Code\)](#)을 이해하기 쉽게 요약한 것입니다.

[Disclaimer](#)

공학박사 학위논문

**Light extraction from transparent
electrode based organic light
emitting diodes with high efficiency
and high color quality**

고 효율 및 고 품질의 색 특성을 갖는 투명전극
기반의 유기발광소자의 광 추출

2015 년 2 월

서울대학교 대학원

재료공학부

김 정 범

Light extraction from transparent electrode based organic light emitting diodes with high efficiency and high color quality

지도 교수 김 장 주

이 논문을 공학박사 학위논문으로 제출함

2015 년 2 월

서울대학교 대학원

재료공학부

김 정 범

김 정 범 의 박사 학위논문을 인준함

2015 년 2 월

위 원 장 윤 재 루 (인)

부위원장 김 장 주 (인)

위 원 김 기 범 (인)

위 원 손 세 환 (인)

위 원 이 정 익 (인)

Abstract

Light extraction from transparent electrode based organic light emitting diodes with high efficiency and high color quality

Kim Jung-Bum

Department of Materials Science and Engineering

The Graduate School

Seoul National University

Organic light emitting diodes (OLEDs) are moving toward high efficiency and high color quality required to be used in solid state lighting and display industry. This thesis focuses on the investigation of the optical loss channels and introduces a simulation methodology of light extraction in OLEDs. In addition, the theoretical and experimental results of the inverted top emission and transparent OLEDs with light extraction structures are presented to reach high efficiency and high color quality.

Chapter 1 explains a basic principle of OLED operation and defines the factors which determine the internal and external efficiencies. Optical analysis method in OLEDs is introduced in terms of the all optical channels such as

out-coupled, guided, and lost lights. Especially, the suppression of plasmonic loss will be discussed by using mode analysis.

Chapter 2 represents the optical simulation method of the light extraction efficiency of organic light emitting diodes (OLEDs) with a light extraction structures based on the ray optics combined with the classical dipole model. Firstly, the angular distribution of emitted light from top emitting OLEDs (TEOLEDs) into the MLA was calculated by the classical dipole model and was taken as the input for the calculation of light propagation and extraction in the MLA. Secondly, the reflectance at the MLA/air interface of the OLEDs was calculated as functions of wavelength and incident angle of the incident light using the ray tracing Monte Carlo simulation. The enhancement ratio of external quantum efficiencies is calculated as functions of the refractive indices and structure of the MLA. The simulation method combining the classical dipole model and the ray tracing method described the experimental results very well including the external quantum efficiency and angle dependent intensities and spectra. Therefore the model can be utilized to the optimization of MLAs for light extraction.

In **chapter 3**, highly efficient phosphorescent green inverted top emitting OLEDs by using transparent top electrode and horizontally oriented emitter are represented.

A highly efficient phosphorescent green inverted top emitting organic light emitting diode with excellent color stability is fabricated by using the 1,4,5,8,9,11-hexaazatriphenylene-hexacarbonitrile/ indium zinc oxide top electrode and bis(2-phenylpyridine)iridium(III) acetylacetonate as the emitter in an exciplex forming co-host system. The device shows a high external quantum efficiency of 23.4% at 1,000 cd/m² corresponding to a current

efficiency of 110 cd/A, low efficiency roll-off with 21% at 10,000 cd/m² and low turn on voltage of 2.4 V. Especially, the device showed very small color change with the variation of $\Delta x=0.02$, $\Delta y=0.02$ in the CIE 1931 coordinates as the viewing angle changes from 0 to 60°. The performance of the device is superior to that of the metal/metal cavity structured device.

In addition, the phosphorescent green emitter of Ir(ppy)₂tmd [bis(2-phenylpyridine)iridium(III)(2,2,6,6-tetramethylheptane-3,5-diketonate)] as the horizontally oriented emitter in an exciplex forming co-host system is used in the inverted top emitting OLEDs. The device showed a maximum current efficiency of 120.7 cd/A, a maximum external quantum efficiency (EQE) of 27.6% and the power efficiency of 85.9 lm/W at 1000 cd/m². Moreover the efficiency roll off was small long-lasting to 20,000 cd/m² with EQE's and current efficiencies of 26.0% and 113.7 cd/A at 10,000 cd/m² and 24.5% and 107.6 cd/A at 20,000 cd/m², respectively. Based on the results, the optical analysis of the maximum achievable and measured EQE was performed using photoluminescence quantum yield (q_{PL}), horizontal orientation ratio (Θ) and electrical loss (Γ).

Highly efficient and high color quality white TEOLEDs by using the single layer broadband anti-reflection (AR) coating on the top of the TEOLEDs are represented in **chapter 4**. The white TEOLEDs with the broadband AR layer shows small variation of spectral change on viewing angles of $\Delta x = 0.02$, $\Delta y = 0.01$ at 0 ~ 60° compared to the reference device of $dx = 0.15$, $dy = 0.05$ for W1 (17wt% of B3PYMPM in buffer layer) and $\Delta x=0.14$, $\Delta y=0.03$ for W2 (15wt% of B3PYMPM in buffer layer). Furthermore, the white TEOLEDs with the broadband AR layer show the external quantum efficiencies increase due to the relaxation of the resonance effect of the device structure. As results,

the EQEs of 18.8% and 16.9% for W1 and W2 of the single junction white TEOLEDs are realized with the small color variation on viewing angles, resulting in the duv values of $-0.0014\sim 0.0009$ and $0.0041\sim 0.0058$ at $0\sim 60$ degrees. Correlated color temperatures of W1 and W2 are $\sim 2200\text{K}$ and $\sim 3000\text{K}$ satisfied with the blackbody radiation white within 5 steps of MacAdam ellipse for the requirement of the solid state lighting application.

In **chapter 5**, a highly enhanced light extractions from an inverted top emission organic light emitting diode with little image blurring and color variation on viewing angles is reported. Direct integration of a high refractive index micro lens array on the top of the transparent indium zinc oxide top electrode of a green phosphorescent OLED showed a significant enhancement of light extraction to get EQE of 44.7% from 27.6%, the power efficiency of 134.7 lm/w from 85.9 lm/W and the current efficiency of 217.2 cd/A from 120.7 cd/A without image blurring. In addition, the device showed excellent color stability on viewing angle with Commission Internationale de l'Eclairage (CIE) coordinate of $\Delta x = 0.01$, $\Delta y = 0.01$ as the viewing angle varied from 0 to 60. In addition, the simulation model for calculation of the light extraction efficiency of indium zinc oxide (IZO) top electrode based top emitting OLEDs (TEOLEDs) with directly formed organic MLAs fabricated using the thermal evaporation of α -NPD on top of the device is also represented. The angular intensity distribution of the light emitted by the TEOLEDs into the MLAs is investigated from the classical dipole model in the cases of 30, 50, and 70 nm thick electron injection layers (EILs), giving the most dramatically change of the angle dependent emission properties. These angle dependent emission properties are used as the light sources set in the calculation of light propagation and extraction to the air by Monte Carlo

ray tracing. This method combines coherent and incoherent light characteristics of OLEDs, resulting in the excellent agreement between theoretically calculated and experimentally measured the enhancement of the external quantum efficiencies.

In **chapter 6**, a transparent OLED with an extremely high EQE, achieved by reducing the surface plasmonic and intrinsic absorption loss is introduced, where the transparent indium zinc oxide (IZO) and indium tin oxide (ITO) layers were used as the top and bottom electrodes, respectively. We adopted a special chemical to get the high performance transparent OLED to protect organic layers from the sputtering damage during the deposition of top IZO electrode. To extract the confined light inside the device, a high refractive index micro-cone array was additionally fabricated on the transparent top electrode using a simple evaporation method and a micro-lens array (MLA) sheet was attached on the bottom side of the glass substrate. As a result, the EQE of the device increased from 18.2% to 47.3% by using both microstructures, and this was additionally enhanced to 62.9% by integrating a micro-cone array on one side and a half-sphere lens on the other side. In addition, 75.7% and 77.2% of the total extractable portions of emitted light are calculated from the classical dipole model and combined simulation method.

Keywords: Optical mode analysis, surface plasmonic loss, light extraction simulation, transparent electrode based inverted organic light emitting diode

Student Number: 2011-30932

Contents

List of figures.....	IX
List of Tables.....	IX
Chapter 1 Introduction	1
1.1 Organic light emitting diodes	1
1.2 Operating principle in OLEDs	3
1.3 External quantum efficiency of OLEDs.....	7
1.4 Optical loss modes in organic light emitting diodes ...	10
Chapter 2 Optical simulation method of light extraction in top emitting organic light emitting diodes.....	20
2.1 Introduction	20
2.2 Methodology of optical analysis of light extraction....	22
2.3 Result and Discussion	29
2.4 Conclusion	33
Chapter 3 Transparent top electrode based inverted top emitting organic light emitting diodes	34
3.1 Optical characteristics of transparent top electrode based inverted top emitting OLEDs.....	34
3.1.1 Introduction.....	34

3.1.2 Experiment.....	35
3.1.3 Results and Discussion.....	38
3.1.4 Conclusion.....	44
3.2 Transparent top electrode based inverted top emitting OLEDs using a horizontally oriented emitter.....	45
3.2.1 Introduction.....	45
3.2.2 Experiment.....	46
3.2.3 Results and Discussion.....	48
3.2.4 Conclusion.....	54

**Chapter 4 Inverted top emitting white organic light
emitting diodes with high color quality by using
broadband anti-reflection top electrode 55**

4.1 Introduction	55
4.2 OPTICAL SIMULATION ANALYSIS.....	59
4.3 Experiments	66
4.4 Results and Discussion.....	70
4.5 Conclusion	75

**Chapter 5 Highly enhanced light extraction from
inverted top emitting OLEDs with little image
blurring and good color stability..... 77**

5.1 Introduction	77
------------------------	----

5.2 Experiments	78
5.3 Results and Discussion.....	80
5.4 OPTICAL SIMULATION FOR LIGHT EXTRACTION	87
5.5 Conclusion	89
Chapter 6 Highly enhanced light extraction from surface plasmonic loss minimized OLEDs	90
6.1 Introduction	90
6.2 Experiments	91
6.2.1 Transparent device fabrication and measurement.....	94
6.2.2 Microstructure fabrication.....	96
6.3 Result and Discussion	97
6.4 Simulation method.....	106
6.5 Conclusion	108
Bibliography	110
초록.....	120

List of Tables

Table 3.1 Performances of inverted TEOLEDs with Ag and IZO top electrodes.	42
Table 3.2 Performances of inverted TEOLEDs.	51
Table 4.1 Performances of white inverted TEOLEDs.	76
Table 5.1 Performances of inverted TEOLEDs.	84
Table 5.2 Comparison of the measured and simulated enhancement ratio and external quantum efficiencies for the inverted TEOLEDs..	88
Table 6.1 Quantum efficiency & Power efficiency for devices.	107

List of figures

- Figure 1.1** (a) A schematic energy level diagram for an organic material with electrodes. (b) A schematic electrical process in multilayer structures in OLED. 4
- Figure 1.2** The schematic diagram of the energy transfer process for (a) Förster and (b) Dexter energy transfer. 6
- Figure 1.3** Contour plot of the simulation results of EQE as a function of q_{PL} , and θ . The two dashed lines indicates the locus of the EQE for $\theta = 0.77$ and $q_{PL} = 0.94$, respectively. In a similar manner, the dotted lines indicate the EQE for $\theta = 0.67$ (isotropic), 0.75, and 0.79, respectively..... 9
- Figure 1.4** Schematic for optical loss channels in OLEDs. 11
- Figure 1.5** Mode analyses in ray optics model.. 13
- Figure 1.6** Change of dissipated power and surface plasmon polaritons against the location of emitter.. 15
- Figure 1.7** Comparison of mode analysis of the thin metal and TCO top electrode based TEOLEDs..... 17
- Figure 1.8** Mode analysis of (a) fully horizontally oriented emitter and (b)

fully vertically oriented emitter from the transparent top electrode based TEOLEDs..... 19

Figure 2.1 (a) Device structure of the inverted TEOLED with light extraction structures and schematic for the optical analysis method combined with the classical dipole model and ray tracing model (b) Design of fully packed organic micro lens arrays of ray tracing simulation from LightTools® and inset image is the micro scope image of the structures.. 23

Figure 2.2 Angle dependent emission characteristics of the inverted TEOLEDs. (Parameters for the light source set up the ray tracing simulation) (a) the calculated results of the angle dependent intensity distribution from the devices with the 30, 50, and 70 nm thick EILs, emitting to the ambient surrounding of air and α -NPD. (b) (c) and (d) calculated intensity profiles with α -NPD ambient surrounding as a function of wavelength and emission angle from the devices with the 30, 50, and 70 nm thick EILs, respectively..... 25

Figure 2.3 Angle dependent light extraction efficiencies of fully packed MLAs. (a) is schematic for the simulation of angle dependent light extraction as functions of azimuthal angle of incident light and reflectance of reflector..... 26

Figure 2.4 Calculated results of angle dependent reflectance of the OLEDs

with metal electrode (incident light from α -NPD ambient surroundings) (a) (b) and (c) are reflectance with α -NPD ambient surrounding as a function of wavelength and emission angle from the devices with the 30, 50, and 70 nm thick EILs, respectively. 28

Figure 2.5 Calculated results of angle dependent reflectance of the OLEDs with metal electrode as a function of refractive index of ambient surrounding and incident angle. (a) (b) and (c) are calculated reflectance results from the devices with the 30, 50, and 70 nm thick EILs, respectively..... 30

Figure 2.6 (a) Simulation results of enhancement ratio of radiant flux as a function of radius of fully packed MLAs (b) values of radius of micro lens for calculation of fill-factor of MLAs. 31

Figure 2.7 Simulation results of outcoupling enhancement ratio by light extraction structures as functions of the refractive index and fill-factor of MLAs. (a) (b) and (c) are the results from the devices with the 30, 50, and 70 nm thick EILs, respectively..... 32

Figure 3.1 (a) Device structures of inverted TEOLEDs with Ag (left) and IZO (right) top anodes, respectively. (b) Molecular structures of organic materials in the emitting layer..... 37

Figure 3.2 Contour plots of efficiency of the inverted TEOLEDs as

functions of the thicknesses of n-doped electron injection layer (EIL) and p-doped hole injection layer (HIL); relative external quantum efficiencies (a,c) and relative current efficiencies (b, d) for the device with Ag (a,b) and IZO (c, d) top anodes, respectively. 39

Figure 3.3 Electrical and optical characteristics of inverted TEOLEDs; (a) current density–voltage–luminance (J–V–L) characteristics, (b) current and power efficiencies against current density, (c) external quantum efficiencies and (d) normalized electroluminescent intensities at different viewing angles which are compared with a Lambertian emitter..... 40

Figure 3.4 Angle dependent EL spectra of TEOLEDs with Ag (a) and IZO (b) top anodes. (c) Variation of CIE 1931 coordinates (x,y) with viewing angle for inverted TEOLEDs with Ag (rectangle) and IZO (triangle) top electrodes, respectively..... 43

Figure 3.5 Schematic diagram of the inverted TEOLEDs (a) device structures of inverted TEOLEDs (b) Molecular structures of organic materials in the emitting layer..... 47

Figure 3.6 Electrical and optical characteristics of inverted TEOLEDs; (a) contour plots of relative current efficiencies of the inverted TEOLEDs as functions of the thicknesses of EIL and HIL (b) current density–voltage–luminance (J–V–L) characteristics, (c)

normalized luminescent spectra of the devices with 30, 50, and 70 nm thick EILs: simulated (dashed lines) and measured (solid lines) values (d) normalized angle dependent intensity distributions of the devices: simulated (filled symbols) and measured (open symbols) values. 49

Figure 3.7 Performances of inverted TEOLEDs (a) current efficiencies against current density (b) power efficiencies and external quantum efficiencies against luminance. 50

Figure 3.8 Contour plots of the simulation results of EQE of the inverted TEOLED as a function of q_{PL} and Θ with the theoretical maximum value. The dashed lines indicate the EQEs with $q_{PL}=0.96$ and $\Theta=0.67$ (isotropic), 0.78 (Ir(ppy)₂tmd), respectively..53

Figure 4.1 (a) Schematic diagram of transparent conducting oxide top electrode based inverted TEOLED with broadband anti-reflection coating (b) reflectance data of Ag 20 nm, Ag 20 nm with TeO₂ 25 nm capping layer, IZO 60 nm, IZO 60 nm with LiF 100 nm capping layer.. 58

Figure 4.2 The comparison of the angle dependent spectral change influenced by the top electrode system and device structure. (under the assumption of constant quantum yield in all visible wavelength regions) The calculated results of the device with (a) Ag 20 nm, (b) IZO 60 nm, Ag 20 nm with the high refractive

index capping layer, and (d) IZO 60 nm with the low refractive index capping layer of single layer anti-reflection condition of top electrode system based TEOLEDs..... 60

Figure 4.3 The device structures of four types of TEOLEDs used for the optical analysis of the wavelength-dependent intensity characteristics. (a) Ag 20 nm, (b) Ag 20 nm with TeO₂ 25 nm, (c) IZO 60 nm, (d) IZO 60 nm with single layer anti-reflection coating top electrodes based inverted TEOLEDs.. 61

Figure 4.4 Device structures of phosphorescent blue, green, and red inverted TEOLEDs and molecular structures of the emitters represent (a), (b), and (c), respectively. External quantum efficiency influenced by capping layer in transparent conducting oxide top electrode based TEOLEDs. Simulation results of (a) the phosphorescent blue emitter of FIrpic. Quantum yield ($q_{PL} = 1$), the horizontal orientation factor ($\Theta = 0.76$). (b) the phosphorescent green emitter of Ir(ppy)₂tmd. Quantum yield ($q_{PL} = 0.96$), the horizontal orientation factor ($\Theta = 0.78$). (c) the phosphorescent red emitter of Ir(mphmq)₂tmd. Quantum yield ($q_{PL} = 0.96$), the horizontal orientation factor ($\Theta = 0.82$). Black dotted line through the contour plot is calculated thicknesses of $\lambda/4$ phase matching @ 550 nm according to the refractive index.. 63

Figure 4.5 Angle dependent spectral and color coordinate characteristics of

RGB inverted TEOLEDs. (a) Phosphorescent green emitter of Ir(ppy)₂tmd, (b) phosphorescent red emitter of Ir(mphmq)₂tmd, (c) phosphorescent blue emitter of FIrpic..... 64

Figure 4.6 The comparison between photoluminescent and electroluminescent spectral characteristics of the TCO top electrode based TEOLEDs with broadband anti-reflection... 65

Figure 4.7 (a) Device structure and materials of white inverted top emitting OLEDs (b) TEOLEDs and the schematic of the blackbody radiation white color design. (c) is energy diagram of consisting materials of white emitter. (d) is triplet energy levels of consisting materials of white emitter.. 67

Figure 4.8 (a) Emission spectra in normal direction of white inverted TEOLEDs and (b) Angle dependency of the color coordinate in white inverted TEOLEDs, while doping concentration of B3PYMPM in buffer layer was controlled from 1~17wt%..... 69

Figure 4.9 Angle dependent emission spectra of white inverted TEOLEDs (a) and (b) are reference devices of W1 and W2. (c) and (d) are devices with broadband AR layer of W1 and W2, respectively. (e) Angle dependent color coordinate of the devices from 0 to 60 degrees.. 71

Figure 4.10 (a) external quantum efficiencies and power efficiencies of the

white inverted TEOLEDs (b) normalized electroluminescent intensities at different viewing angles of reference devices and devices with broadband AR layer.. 72

Figure 4.11 (a) external quantum efficiencies and power efficiencies of the white inverted TEOLEDs (b) normalized electroluminescent intensities at different viewing angles of reference devices and devices with broadband AR layer.. 74

Figure 5.1 Inverted TEOLED & Microstructures. (a) Device structure of the inverted TEOLED and molecular structures of organic materials in the emitting layer. (b) Schematic diagrams of the bottom and top emission OLED with MLAs. (c) Optical microscope image and SEM cross section of the organic MLAs.. 79

Figure 5.2 Characteristics of the inverted TEOLEDs with and without organic MLAs. (a) Voltage dependent current density and corresponding luminance. (b) Normalized intensity spectra in normal direction with and without organic MLAs and the intrinsic PL spectrum of the Ir(ppy)₂tmd including the angle dependent intensity distribution of the devices in inset. (c) Calculated and measured spectra of the reference devices. (d) Calculated spectra from the TEOLED with α -NPD semi-infinite surroundings on the top of the device compared to the PL spectrum of the Ir(ppy)₂tmd..... 81

Figure 5.3 Device performance of the inverted TEOLEDs with and without organic MLAs. (a) Current efficiencies, and (b) external quantum efficiency and power efficiency of the devices with (red circle) and without (black rectangle) organic MLAs..... 83

Figure 5.4 Angular emission property of the inverted TEOLEDs with organic MLAs compared to the intrinsic PL spectrum of Ir(ppy)₂tmd. (a) Angle dependent emission spectra and (b) normalized spectra of the device with organic MLAs and PL spectrum of the Ir(ppy)₂tmd. (c) CIE 1931 color coordinates of the devices with organic MLAs and PL spectrum of the Ir(ppy)₂tmd..... 85

Figure 5.5 Comparison for the image blur of the bottom and top emission OLEDs. Photo images and intensity profile against the distance from OLED center of (a) the bottom emission OLED with and without MLAs on the glass substrate and (b) the top emission OLED with and without organic MLAs on top of the TCO electrode at same luminance of 500 cd/m². The cell size of the images was 2 mm x 2 mm..... 86

Figure 6.1. Transparent OLED & Microstructures. (a) Schematic diagrams of the structure of the transparent OLED and the microstructures for light extraction. (b) SEM images of the top side micro cone array. (c) SEM images of the bottom side micro lens array. (d) Optical microscope image of the top side micro

cone array. (e) Optical microscope image of the bottom side micro lens array..... 93

Figure 6.2 Fabrication of high refractive index microstructures. (a) Optical microscope image of shadow mask used for the fabrication of micro cone structures. (b) SEM image of the structure fabricated using two step deposition rate of ~5 nm/s for ~30 min followed by ~15 nm/s for ~10 min. (c) Cross section image of the structure grown by two step deposition rate with the taper angle of ~40° at the deposition rate of ~5 nm/s and the taper angle of ~60° at the deposition rate of ~15 nm/s. (d), (e). SEM images of the structure fabricated using two step deposition rate of ~20 nm/s for ~ 30 min followed by ~25 nm/s for ~ 30 min. (f), Cross section image of the structure grown by two step deposition rate with the taper angle of ~70° at the deposition rate of ~20 nm/s and the taper angle of ~80° at the deposition rate of ~25 nm/s.. 95

Figure 6.3 External quantum efficiencies and power efficiencies, angle dependent emission intensities and spectra of the OLEDs. (a)-(c) External quantum efficiencies (filled symbols) and power efficiencies (open symbols) as a function of current density for the total emission (triangle), bottom emission (rectangle) and top emission (circle) from the reference transparent OLED without any light extraction layers: in (a) with the micro-cone

array on the top side and the micro-lens array at the bottom side; in (b), with the micro-cone array on the top and a half sphere lens on the bottom side; and in (c), schematic diagrams of the structure of the OLEDs are displayed as the inset of (a)-(c). (d)-(e), Normalized angle dependent emission intensities from the (d) bottom and (e) top sides of the OLED with the microstructures on both sides (circle) are compared with the reference OLED (rectangle). Lambertian emission patterns are displayed as dashed lines. (f)-(g), Angle dependent emission spectra from the OLEDs (f) with the microstructures and (g) without the microstructures..... 98

Figure 6.4 Characteristics of the reference transparent OLED. (a) Voltage dependent current density and corresponding luminance. (b) Current and power efficiencies as a function of luminance..... 99

Figure 6.5 Mode analyses of the top emission, bottom emission and transparent OLEDs. The power coupling ratio simulated using the classical dipole model for (a) the top emission OLED with a metal cathode and anode, (b) the top emission OLED with a metal cathode and IZO anode, and (c) the transparent OLED with an ITO cathode and IZO anode. The photoluminescent quantum yield of the emitter is assumed to be 1 with a random orientation in the simulation. The device structures for the simulation are displayed in Figure S3. (d), simulated power coupling ratio of the reference transparent OLED where the

optical loss coming from the PL quantum yield of 0.91 and the electrical loss of 11% are included in the simulation to fit with the experimental EQE value of 18.2%..... 101

Figure 6.6 Geometry and results of 3 dimensional ray tracing. (a) Geometry of the ray tracing used for the simulation. A 2 mm x 2 mm planar light source on a 2.5 cm x 2.5 cm glass substrate is located at the center of an integrating sphere used as the detector. The planar light source consists of homogeneously spread 25,000 isotropic point sources in the square emissive area. (b)-(e), Ray tracing images of (b) the reference OLED, (c) the OLED with MCA/MLA, (d) the OLED with MCA/a half sphere, and (e) the OLED with 10 mm hemispheres on the both sides of the OLED. The simulation was performed using the LightTools.. 103

Figure 6.7 Simulation results of outcoupling enhancement ratio by the light extraction structures. Outcoupling enhancement ratios of the OLEDs with the MCA/MLA (a), (b) and with the MCA/half-sphere lens (c), (d) as functions of the height (a), (c) and the refractive index (b), (d) of the microcones, microlenses and the half-sphere. A 3 dimensional ray tracing simulation tool (LightTools) was used for the simulation. The MCA and MLA were assumed to have fill factors of 100% and 90%, respectively, and the diameter of the micro-cones was fixed to 60 μm in the simulation. A 2 mm x 2 mm planar light source

located in the middle of the organic layer was used for the ray tracing where the planar light source consisted of 25,000 homogeneously spread isotropic point sources in the square emissive area. Refractive indices of 1.52 and 2.0 were used for the glass substrate and IZO, respectively..... 105

Chapter 1 Introduction

1.1 Organic light emitting diodes

The emissive electroluminescence from organic materials was firstly observed in the middle of the twentieth century¹⁻² and since then, the importance of the work functions for hole and electron injection contact in organic single crystal was reported.³⁻⁴ Finally, in 1987, the thin film device based on the vapor deposition with double layers was firstly demonstrated by Tang and VanSlyke at Eastman Kodak.⁵ After that, OLEDs have been improved the life time and efficiency with great potentials for the future type of application in displays and solid state lightings.⁶⁻⁸ OLEDs are slim and lightweight, flexibility, transparency, and the light generation process of electroluminescence yields high electron-photon conversion efficiency. Moreover, the emission of the light in OLEDs is generated in sizable area to realize anti-glare illumination not only on glass substrate but also on flexible substrate leading to new innovative designs. Furthermore, organic materials allow the various processing techniques such as thermal evaporation⁵, spin coating⁹, ink-jet¹⁰ and screen printing¹¹, and roll to roll printing.¹² The possibility of a solution process promises lowering the fabrication costs toward realization of mass production.

Efficiency of OLEDs had a break through by using phosphorescent emitter to manipulate triplet exciton.¹³ Especially, strong spin-orbit coupling of organometallic compounds with heavy metal emitted phosphorescent light at room temperature which showed almost 100% internal quantum efficiency

of the OLEDs.^{14,15}

However, in planar device, external quantum efficiency is limiting the overall device performance because of the channels of confined and lost light. The photon energy of an excited emitter is radiated inside of the organic layer which has higher refractive index than ambient surroundings and only a small fraction of power can be extracted from the device due to the difference of the refractive indices at the interfaces and intrinsic optical properties of consisting materials.^{16,17}

The basic principle of OLEDs operation, out-coupling efficiency, optical loss channels and analysis method of light extraction in OLEDs will be further discussed in the next sections.

1.2 Operating principle in OLEDs

The basic structure of the simplest OLED consists of one organic layer between two electrodes. **Figure 1.1a** shows a schematic energy level diagram for the simplest OLED. Φ_{anode} and Φ_{cathode} are the work functions of the anode and cathode. Excess charge carriers from electrodes inject into an organic material at an applied bias voltage. Electron and hole energy barriers (Φ_e and Φ_h) are determined by the difference of the work function of the electrodes. Built-in potential ($\Phi_{\text{bi}} = \Phi_{\text{anode}} - \Phi_{\text{cathode}}$) is defined from the difference in the work function of the electrodes. In order to inject charge carriers from the electrode to organic, the external bias V must be larger than the built-in voltage. ($V_{\text{bi}} = \Phi_{\text{bi}}/e$, $V > V_{\text{bi}}$) Including functional layers such as electron, hole injection and transporting layer allows the better performance for the device efficiency and stability. The positively biased anode is required in order to inject holes into the hole transport layer (HTL) influenced by the work functions. Similarly, electrons are injected from the cathode into the electron transport layer (ETL).¹⁸⁻²⁰ In some cases, high-efficient OLEDs employ additional layers such as electron, hole injection and blocking layers. Figure 1.1b represents the operating processes in a multi-layered OLED. Anode is mostly used the transparent conducting metal oxide like indium tin oxide (ITO) in the conventional bottom emission OLEDs. By using hole injection layer (HIL) between anode and hole transport layer (HTL), the device has longer life time and the breakdown failure can be reduced by enhancing the stability. Electron injection layer (EIL) works to reduce the injection barrier between cathode and electron transport layer (ETL) which mostly influences

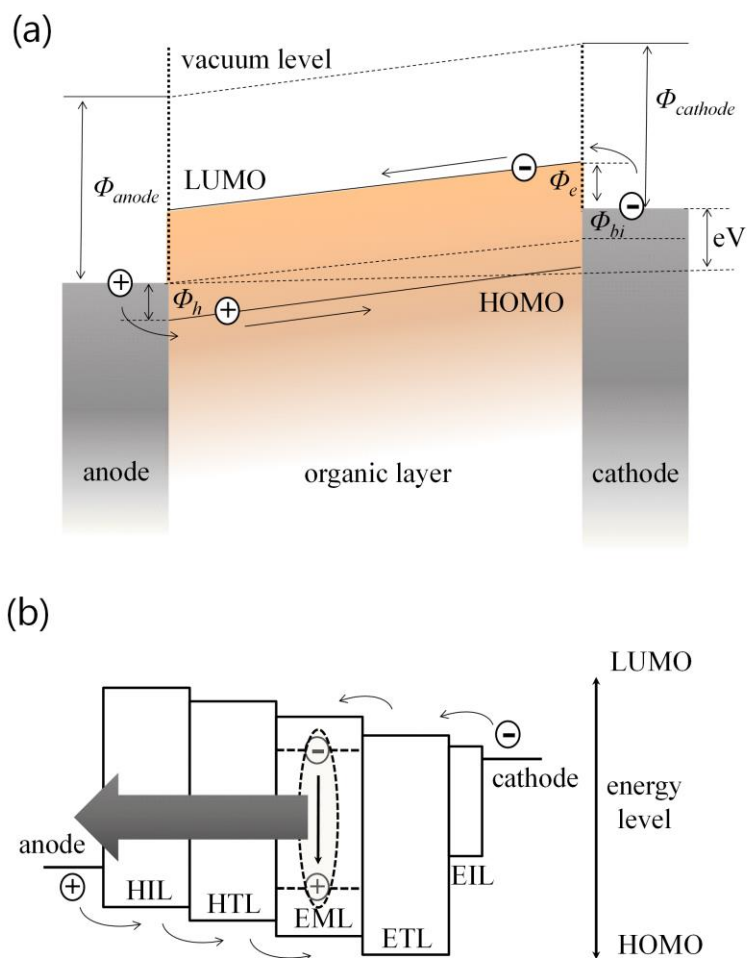


Figure 1.1 (a) A schematic energy level diagram for an organic material with electrodes. (b) A schematic electrical process in multilayer structures in OLED.

emitting layer (EML) is an important factor to decide high efficiency because driving voltage of the device. Electron and hole mobilities of transporting layers are important to balance charge carriers and reduce voltage drops. Exciton confinement in more electron-hole pairs can contribute the exciton generation by reducing the leakage current. The higher LUMO level of HTL and the lower HOMO level of ETL allow effective confinement of charge carriers in EML to avoid the electron-hole leakage current²¹⁻²³. In host, guest system of EML, electron-hole charge balance can be affected by polar or bipolar charge transport property of host material which is an important factor to decide recombination zone. Host materials also require a higher singlet level for fluorescent emitter and a higher triplet level for phosphorescent emitter. In addition, in order to achieve higher quantum yields, guest materials should have high quantum yields and well disperse in the host materials. There are two mechanisms of non-radiative energy transfer between host and guest materials. Energy transfer from an excited host to a dopant is Förster transfer in dipole interactions between host and dopant. Förster energy transfer is activated by the dipole-dipole interaction and the energy transfer rate can be expressed by the fluorescent lifetime of host materials. Förster energy transfer is a long range transfer about 100 Å. The channels of energy transfer are from the singlet of the host to the singlet of the dopant, from the singlet of the host to the triplet of the dopant, and from the triplet of the host to the triplet of the dopant. In addition, the emission spectrum of host and the absorption spectrum of dopant should have spectral overlap to achieve better energy transfer. Another mechanism of energy transfer is Dexter energy transfer. This energy transfer is processed by hopping which needs short range of inter-exciton distance within 10 Å. Dexter energy transfer acts from the singlet of

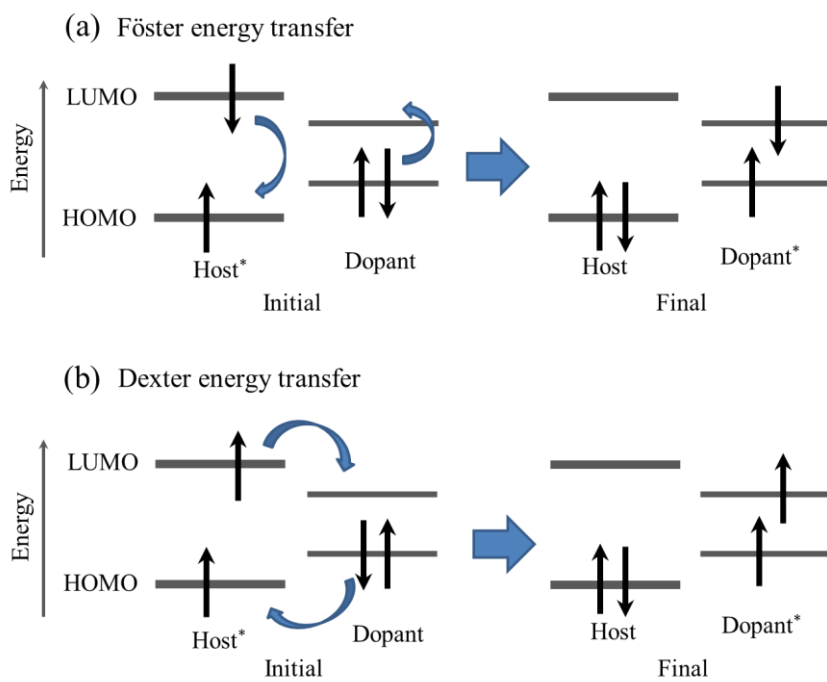


Figure 1.2 The schematic diagram of the energy transfer process for (a) Förster and (b) Dexter energy transfer

the host to the singlet of the dopant or from the triplet of the host to the triplet of the dopant. Förster and Dexter energy transfer represent in Figure 1.3.

1.3 External quantum efficiency of OLEDs

The external quantum efficiency (EQE) of OLEDs describes the ratio between the number of emitted photons and injected charge carriers. In general, EQE of OLEDs consists of internal quantum efficiency (IQE) and out-coupling efficiency and expresses as follows

$$\eta_{EQE} = \eta_{int} \times \eta_{out} = \gamma \times \eta_{S/T} \times q_{eff} \times \eta_{out} \quad (1)$$

Internal quantum efficiency is composed of three parameters, where γ is charge balance factor of injected carriers which means the portion of electrical loss, $\eta_{S/T}$ is the ratio of singlet and triplet radiation determined by spin statistics. Fluorescent emitter is limited to 25% of singlet emission but phosphorescent emitter with heavy metal complexes allows 100% of maximum radiation with triplet emission, q_{eff} represents the effective radiative photoluminescent quantum yields, and η_{out} is out-coupling efficiency. Recently, efficiency influenced by molecular orientation factor has been researched intensively. The parameters determining q_{eff} and η_{out} are modified. q_{eff} is the ratio on the number of emitted photons and number of absorbed photons under photoluminescent excitation described by radiative (b_r) and non-radiative decay rate (b_{nr}). Due to the fact that OLEDs have nano scale multi-layer structure, interference effect occurs and influences the

radiative decay rate ($b_r^* = F \cdot b_r$, F is Purcell factor). (Purcell effect) Under infinite surroundings of homogeneous medium, $b_r = b_r^*$ but non-radiative decay rate is not influenced by device geometry and simply lost the excitation energy into heat. Therefore, the effective quantum efficiency can be expressed as follows.

$$q_{eff} = \frac{b_r^*}{b_r^* + b_{nr}} = \frac{F \cdot b_r}{F \cdot b_r + b_{nr}} \quad (2)$$

In particular, the ratio of the horizontal-to-vertical dipole orientation can change the distribution of electric fields oscillation, where P_{\perp} and P_{\parallel} are the vertical and horizontal dipole ratio, respectively. Power dissipation with isotropic dipole orientation, the ratio between vertical and horizontal orientation simply represents

$$P_{iso} = \frac{1}{3}P_{\perp} + \frac{2}{3}P_{\parallel} \quad (3)$$

In recent progress of researches, anisotropic dipole emitters have been proposed. Orientation factor is determined by the horizontal orientation ratio defined by

$$\Theta = \frac{P_{\parallel}}{P_{\perp} + P_{\parallel}} \quad (4)$$

In addition, another parameter of PL emission property affected by microcavity effect is defined as Γ . These two parameters, orientation factor Θ , geometrical factor Γ also influence for out-coupling efficiency η_{out} .

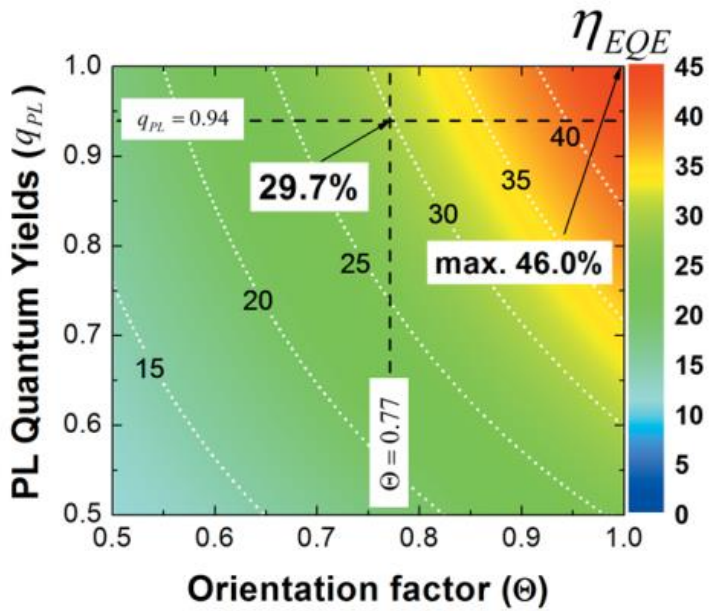


Figure 1.3 Contour plot of the simulation results of EQE as a function of q_{PL} , and Θ . The two dashed lines indicates the locus of the EQE for $\Theta = 0.77$ and $q_{PL} = 0.94$, respectively. In a similar manner, the dotted lines indicate the EQE for $\Theta = 0.67$ (isotropic), 0.75, and 0.79, respectively.

Therefore, the modified equation is expressed by

$$\eta_{EQE} = \eta_{int} \times \eta_{out} = \gamma \times \eta_{S/T} \times q_{eff}(q_{PL}, \Theta, \Gamma) \times \eta_{out}(q_{PL}, \Theta, \Gamma) \quad (5)$$

Parameters can be classified electrical loss and optical loss. Electrical loss is related to the balance of the charge carriers and is represented by γ . Optical loss is composed of material based and device geometry based characteristics. Material-related factors are $\eta_{S/T}$, q_{PL} , Θ and geometrical factor is Γ . Development of host-dopant system in phosphorescent emitter allows high radiative quantum efficiency and internal quantum efficiency close to 100%.^{13-15,22} Molecular orientation factor is related to not only internal quantum efficiency but also out-coupling efficiency when horizontally preferred oriented emitter can increase the efficiency. In addition, by using the optical parameters of photo induced photoluminescent quantum yield (q_{PL}) and horizontal orientation factor (Θ), theoretical prediction can be possible. Recently, theoretical limit of EQE has been reported possible to reach EQE of 46% in conventional ITO-based bottom emission OLEDs with the theoretical prediction in perfect quantum yield of $q_{PL} = 1$ and fully horizontally oriented emitter of $\Theta = 1$.²⁴ However, the planar device still has the limitation of extracting the light from the inside of the device because there are several optical loss modes, which will be discussed in the next section.

1.4 Optical loss modes in organic light emitting diodes

Conventional types of OLEDs consist of glass substrate, transparent

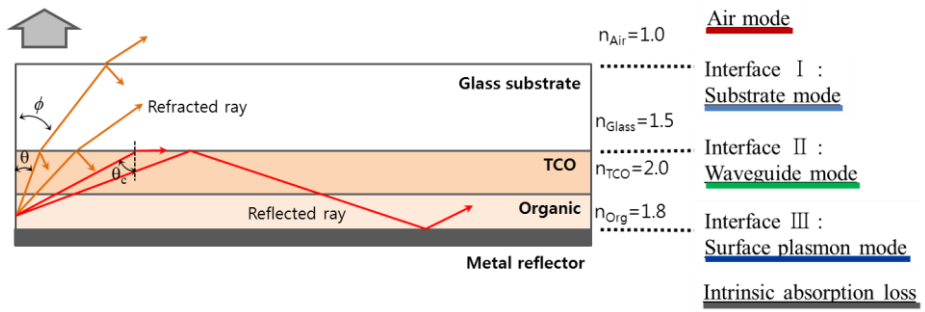


Figure 1.4 Schematic for optical loss channels in OLEDs

conducting oxide anode, and organic multi-layers, metal cathode. (Normally aluminum (Al)) However, light generated inside of high refractive index organic emitter, results in several photon energy loss channels such as confined light, intrinsic absorption, and surface plasmonic loss.¹⁶ Optical channels are commonly classified air mode, substrate mode, waveguide mode, surface plasmonic mode and intrinsic absorption mode as shown in the schematic picture in Figure 1.4. Air mode is the direct emission to air which is used for illumination. Without any out-coupling structure, radiation can only have small fraction, due to the differences of the refractive indices of the consisting materials in OLEDs. In first research for the analysis of optical modes in OLEDs, rough estimation of out-coupled light amount from a planar OLED was only correlated with the critical angle of interfaces determined by Snell's law. Under the assumption of isotropic molecular orientation and Lambertian emission, out-coupled total flux of light amount is roughly estimated by

$$F_{total} = 2\pi n^2 L_0 \quad (9)$$

$$F_{ext} = \int_0^{\pi/2} 2\pi L_0 \cos \theta \sin \theta d\theta = \pi L_0 \quad (10)$$

$$\eta_{out} = \frac{F_{ext}}{F_{total}} = \frac{1}{2n^2} \quad (11)$$

Because most of organic materials have 1.6~1.8 of refractive indices at 550nm, the out-coupled radiation is only estimated 15~20%. In other words, confined light amount is over 80%, which can be extracted by changing the direction of the light propagation. (in Figure 1.5)²⁵ After this rough estimation from Greenham, out-coupled efficiency influenced by cavity effect was described

Theoretical limit of outcoupling efficiency

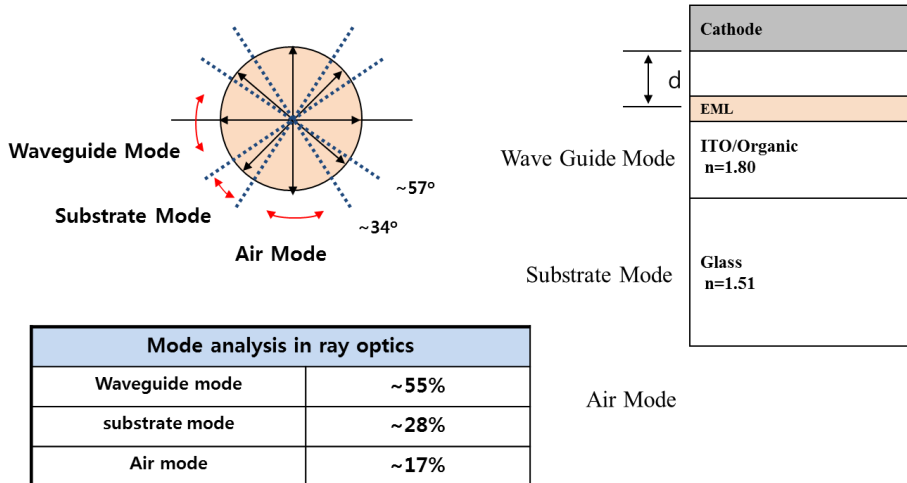


Figure 1.5 Mode analyses in ray optics model.

from Forrest and Sturm group (Combined classical and quantum mechanical microcavity model), giving the out-coupling efficiency is much higher than 20%.^{26,27} However, this model cannot consider the main optical loss of surface plasmonic loss which is near field interaction between dipole emitter and metal electrode. In order to achieve highly efficient OLED with optimization of resonance cavity effect, the dipole emitter in OLEDs is usually located in close to a metal electrode which cannot ignore the energy loss of surface plasmon polaritons (SPPs). The theoretical model using dipole emission interacting with metal or dielectric interfaces in planar structure can represent the most complete description of the microcavity effect and plasmonic effect in near fields.²⁸⁻³³ The classical dipole model is represented by a damped harmonic oscillator with general solutions of dipole moment and reflected electric field, which is described by

$$\frac{d^2}{dt^2} \vec{p} + b_0 \frac{d\vec{p}}{dt} + \omega_0^2 \vec{p} = \frac{e^2}{m} \vec{E}_R(\omega) \quad (12)$$

$$\vec{p} = p_0 e^{-i\omega t} e^{-bt/2} \quad (13)$$

$$\vec{E}_R = E_0 e^{-i\omega t} e^{-bt/2} \quad (14)$$

ω_0 is the oscillator frequency in the undamped case, e is the elementary charge, m is the effective mass of the dipole, $E_R(\omega)$ is the interference-reflected at dipole position, b_0 is the damping constant (inverse lifetime) in the absence of reflecting structure. Through the analysis of the reflection coefficient and damping constant in cavity structure, dissipated power at each optical modes can be calculated, which indicate the energy distribution in and out of the OLEDs. Optical modes can be classified extractable modes and non-extractable modes. Direct out-coupled air mode, substrate mode and

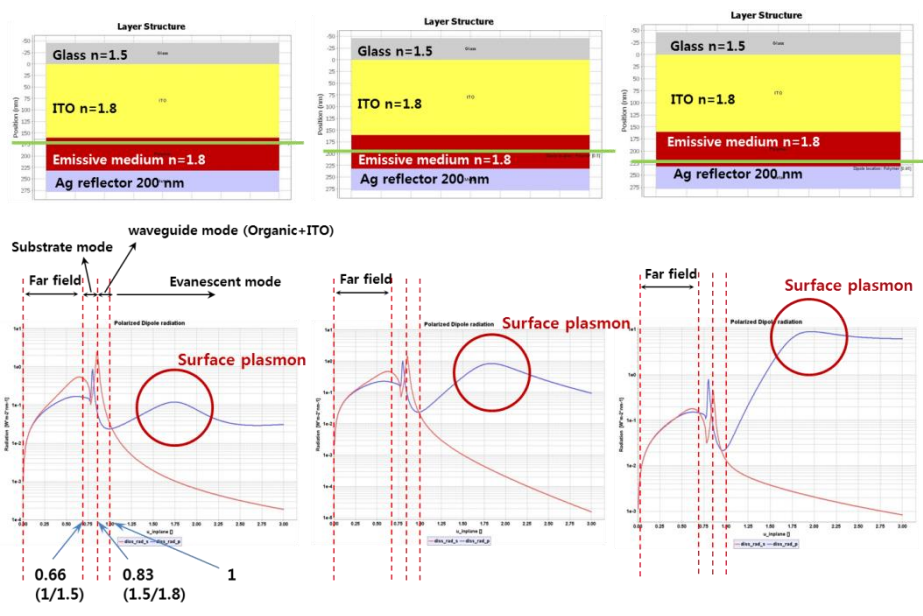


Figure 1.6 Change of dissipated power and surface plasmon polaritons against the location of emitter.

waveguide mode can be extracted if we apply proper light extraction structure at the interfaces. However, surface plasmonic mode and intrinsic absorption mode are crucially limited the possibility to realize high efficient OLEDs. Plasmon defines plasma wave, which means density fluctuation of free electrons. In layered metallic surface, surface plasmon polaritons (SPP) occurs, where plasmons confine to surfaces that can interact with light to form propagating at the metal surface. This longitudinal electromagnetic wave has a dispersion relation as follows

$$k_x = \frac{\omega}{c} \sqrt{\frac{\epsilon_m \epsilon_d}{\epsilon_m + \epsilon_d}} \quad (15)$$

k_x is in-plane wave vector of the complex wave k , c is the speed of light, ϵ_m and ϵ_d are the relative permittivity of metal and adjacent dielectric, respectively. Through the expression of dielectric constant of free-electron plasma from Drude model, the relative permittivity in ideal case for metals can be described by

$$\epsilon_r(\omega) = 1 - \frac{\omega_p^2}{\omega^2} \quad (16)$$

Since the complex dielectric constant is related to the complex refractive index, near field coupling of in-plane wave from SPP generates at the interfaces of metal/organic and metal/air. As OLEDs are usually composed of nano scale multi-layers, p-polarized electromagnetic wave can excite the plasmon, giving one major optical loss of OLED efficiency. Plasmonic loss is generated from the interaction with the surface of conducting materials with free electrons and the distance between dipole emitter and metal surface is one of the important parameters. When the emitter locates far from the metal

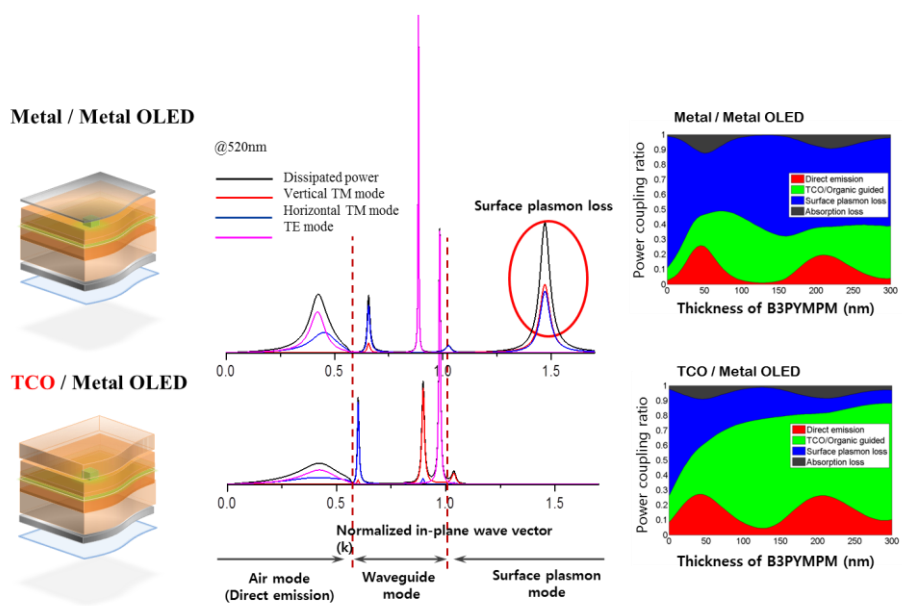


Figure 1.7 Comparison of mode analysis of the thin metal and TCO top electrode based TEOLEDs

surface, the excitation of plasmon can be decreased. Figure 1.6 shows dissipated power against in-plane wave vector and the change of the peak intensity from SPP according to the change of the emitter's location. Especially, top emitting OLEDs which is mainly treated in this thesis have two metal electrodes top and bottom so that plasmonic loss crucially decreases the extractable photon energy and limits the efficient light extraction. Figure 1.7 shows the comparison of plasmonic loss and possible light extraction energy between thin metal top electrode and transparent conducting oxide (TCO) top electrode based TEOLEDs. TCO top electrode based TEOLED has much larger amount of extractable light than thin metal based TEOLEDs. Another important issue is preferred oriented dipole status of emitters. Horizontally oriented emitter generates the collimation of electric field oscillation which can reduce the interaction between propagated light and metal surface. As a result, optical loss from plasmonic coupling can be dramatically changed by the orientation property of the emitter as shown in Figure 1.8. In this thesis, we will focus on the suppression of plasmonic loss and increase extractable light amount, resulting in the realization of highly efficient light extraction in OLEDs.

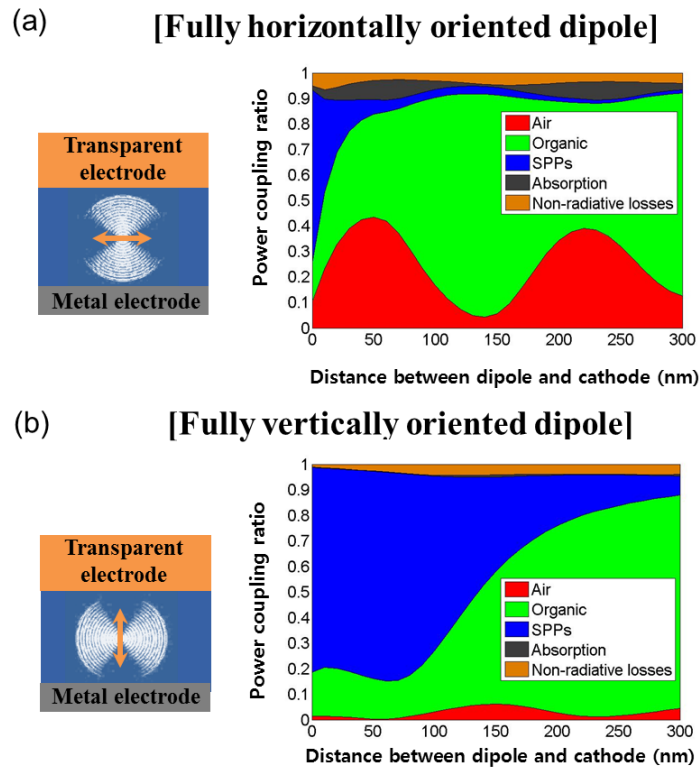


Figure 1.8 Mode analysis of (a) fully horizontally oriented emitter and (b) fully vertically oriented emitter from the transparent top electrode based TEOLEDs

Chapter 2 Optical simulation method of light extraction in top emitting organic light emitting diodes

2.1 Introduction

Efficiency of organic light emitting diodes (OLEDs) has been improved steadily in the past two decades to reach the external quantum efficiency (EQE) of over 30% without extra light extraction structures. Still over 60% of emitted light is confined in OLEDs as waveguide and substrate mode, or lost as surface plasmon polariton (SPP) mode by metal electrodes or absorption.^{16,17} Micro lens arrays (MLAs) have been widely used for light extraction because of their simplicity and high extraction efficiency.³⁴⁻³⁶ Various methods have been reported to simulate the light extraction from OLEDs with MLAs. The first attempt was a ray tracing method where Micro size light extraction structures have been analyzed by ray optics for incoherent light. However, OLEDs have microcavity structures consisting of hundreds nanometer thick stacked layers, whose emission characteristics are greatly influenced by the device structure. These coherent characteristics give difficulties for the optical analysis of light extraction from OLEDs with light extraction structures. Therefore, coherent and incoherent optical characteristics must be considered simultaneously for the simulation of light extraction from OLEDs with light extraction structures. There have been various studies about optical analysis of light extraction from OLEDs with

light extraction patterns. Initial attempts represented by entire ray tracing^{37,38} or assumption of Lambertian angular intensity distributions^{26,39,40} have limitation to express correct dipole status of emitters. Classical dipole model has been used for the optical analysis of OLEDs composed of multiple submicron thick layers,^{26,41-43} giving the analysis for the microcavity effect and surface plasmon polariton but not for the out-coupled light amount of the light extraction structures. The optical modeling based on only geometrical optics does not take into account microcavity effect. FDTD method has been used for the optical analysis of the patterned OLEDs⁴⁴⁻⁴⁸ with dipole emitter but the assumption of computational domains such as the number of dipole emitters, light extraction pattern shape consume very long computational time or generate the difference from the experimental results. Several combined simulation methods have been introduced^{27,49,50} but effective optical analysis method is still needed.

In this chapter, the simulation model for calculation of the light extraction efficiency of indium zinc oxide (IZO) top electrode based top emitting OLEDs (TEOLEDs) with directly formed organic MLAs (refractive index of 4,4-bis[N-(1-naphthyl)-N-phenyl-amino]biphenyl(α -NPD) was used for calculation) on top of the device is represented. The angular intensity distribution of the light emitted by the TEOLEDs into the MLAs is investigated from the classical dipole model in the cases of 30, 50, and 70 nm thick electron injection layers (EILs), giving the most dramatically change of the angle dependent emission properties. These angle dependent emission properties are used as the light sources set in the calculation of light propagation and extraction to the air by Monte Carlo ray tracing. In addition, reflectance of OLED with metal electrode as a function of incident angle was

calculated and set as the parameters of ray tracing simulation. The enhancement ratio of external quantum efficiencies were calculated by this combined simulation method as functions of the refractive indices and fill-factor of the MLAs. This method combines coherent and incoherent light characteristics of OLEDs, resulting in the excellent agreement between theoretically calculated and experimentally measured the enhancement of the external quantum efficiencies.

2.2 Methodology of optical analysis of light extraction

Figure 2.1a shows the schematic diagrams of the structures of the inverted TEOLED with organic MLAs and simulation methods combined with the classical dipole model and ray tracing model. Figure 2.1b represents the design of the light extraction structures for the ray tracing simulation based on the fully packed organic MLAs (α -NPD). In order to calculate the light extraction efficiency of OLEDs, firstly, angle dependent emission characteristics should be considered because the light extraction efficiency is greatly affected by the angle dependent emission property caused by resonance effect. We set the light source for the ray tracing simulation using the angle dependent characteristics from the results of the dipole model simulation. Considering a top emitting OLED with multilayered structure, we first solve the classical dipole model reported by Chance, Prock, and Silbey to provide the most complete classical picture to describe the interference effect.^{41,42} The parameters for numerical calculations include the photoluminescence spectrum of emitting layer and the thickness and complex

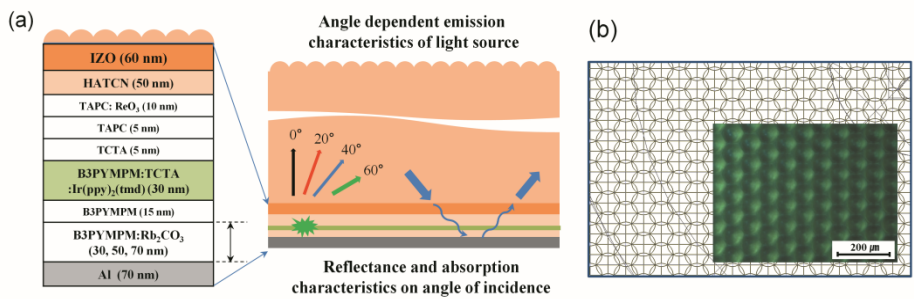


Figure 2.1 (a) Device structure of the inverted TEOLED with light extraction structures and schematic for the optical analysis method combined with the classical dipole model and ray tracing model (b) Design of fully packed organic micro lens arrays of ray tracing simulation from LightTools® and inset image is the microscope image of the structures.

refractive index of each layer. The spontaneous decay time of an exciton is calculated by an oscillating electrical dipole embedded in the OLEDs and the electric and magnetic fields describe the radiation fields for multi-layered structure with full vectorial scheme. The factor influenced by the most significant change of the angular intensity distribution is the distance between the dipole emitters and metal reflector. Three different TEOLEDs were fabricated for the reference devices as functions of the 30, 50, and 70 nm thick EILs. We simulated the angular behavior of emission intensity and spectral property of the light source under the assumption when applying the infinite thickness of α -NPD (refractive index ~ 1.8 @550 nm) on the top of the IZO top electrode based TEOLED. Figure 2.2a shows the result of intensity distribution by viewing angles with air (reference device) and α -NPD (with MLAs) ambient surrounding. The spectral properties as a function of wavelength and viewing angle in the case of α -NPD ambient surrounding are shown in Figure 2.2b, c and d in the case of 30, 50 and 70 nm thick EILs.

We set the result of dipole model calculation to the characteristics of the light source and designed light extraction structures in the Monte Carlo ray tracing simulation by LightTools®. The 3-dimensional geometrical ray tracing simulation was designed and performed. A 2 mm \times 2 mm planar light source located in the middle of the organic layer, where the planar light source consisted of 25,000 rays with the results of angle dependent emission properties calculated by the classical dipole model with upside refractive index infinite surroundings.

Second, we investigate the light extraction efficiency of fully packed α -NPD MLAs as a function of emission angle and reflectance of the reflector as an assumption of the multi layered OLEDs with metal electrode. Constituent

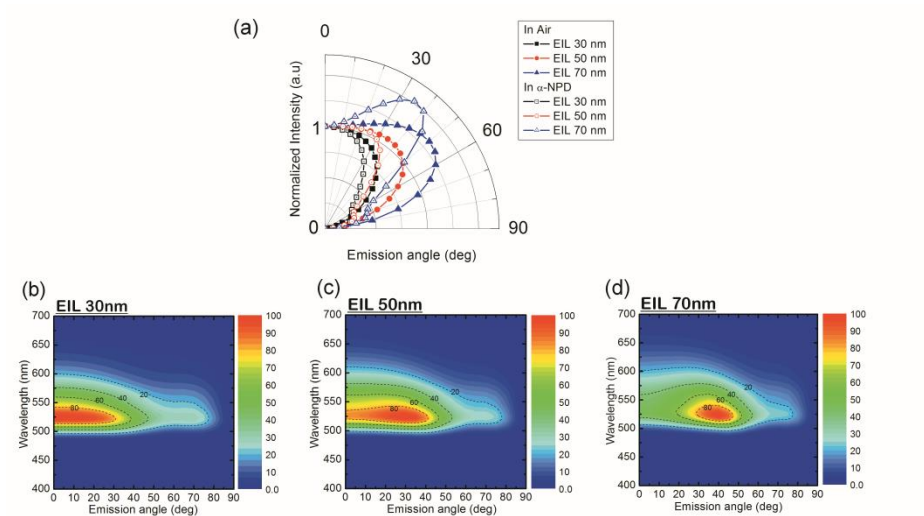


Figure 2.2 Angle dependent emission characteristics of the inverted TEOLEDs. (Parameters for the light source set up the ray tracing simulation) (a) the calculated results of the angle dependent intensity distribution from the devices with the 30, 50, and 70 nm thick EILs, emitting to the ambient surrounding of air and α -NPD. (b) (c) and (d) calculated intensity profiles with α -NPD ambient surrounding as a function of wavelength and emission angle from the devices with the 30, 50, and 70 nm thick EILs, respectively.

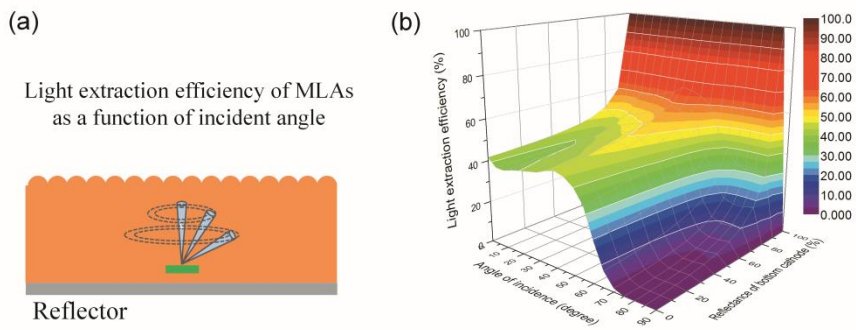


Figure 2.3 Angle dependent light extraction efficiencies of fully packed MLAs. (a) is schematic for the simulation of angle dependent light extraction as functions of azimuthal angle of incident light and reflectance of reflector.

materials were also set in the refractive index of α -NPD. Vertical axis of Figure 2.3 means escape probability of emitted light rays with the same azimuth angle. The result shows the angle dependent reflectance of the OLED stacked can change the light extraction efficiency of fully packed MLAs for a given emission intensity distribution with incident angle. Therefore, angle dependent reflectance should be considered differently for certain device architecture in order to calculate for the light extraction efficiency more precisely.

We thirdly calculated the angle dependent reflectance of multi-layered OLED with metal electrode by using the Fresnel equation with the complex refractive indices of the constituting materials. Ambient surrounding was set in the refractive index of α -NPD. Optical property of the incident light is assumed as photoluminescence characteristics of the emitter. Figure 3 illustrates the results of the reflectance of the multi-layered OLED with metal electrode as a function of wavelength and incident angle. The results are shown in Figure 2.4a, b and c in the case of 30, 50 and 70 nm thick EILs, meaning that the reflectance was influenced by the device architecture, wavelength and incident angle. We also set the results of the reflectance property for each case of the device to the ray tracing simulation. Therefore, the different optical property for the back scattered and recycled light propagation with each incident angle was approximately considered in our simulation method.

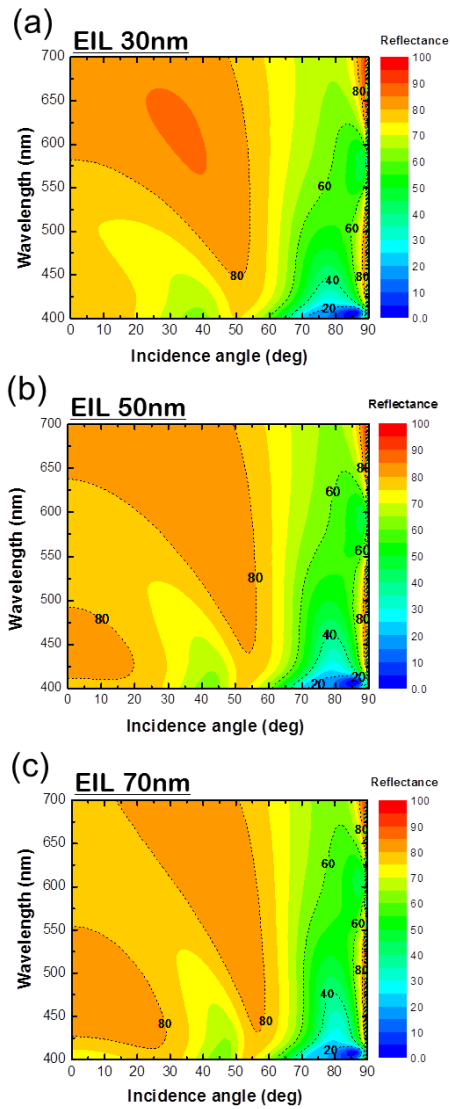


Figure 2.4 Calculated results of angle dependent reflectance of the OLEDs with metal electrode (incident light from α -NPD ambient surroundings) (a) (b) and (c) are reflectance with α -NPD ambient surrounding as a function of wavelength and emission angle from the devices with the 30, 50, and 70 nm thick EILs, respectively.

2.3 Results and Discussion

In order to calculate the light extraction effect of MLAs we parameterized the refractive index and fill-factor of fully packed MLAs. Therefore, we additionally investigated the angle dependent reflectance change as a function of the refractive indices of ambient surrounding (Figure 2.5) and calculate the enhancement ratio of radiant flux as a function of fill-factor of MLAs. Since the size of the MLAs does not influence the result of the enhancement ratio of radiant flux so much (Figure 2.6a), fill-factor of MLAs was controlled by radius of lens size. (Figure 2.6b) Radiant flux corresponding to the external quantum efficiency (EQE) from the light source was integrated using a spherical detector surrounding the source, where the detecting surface and the light source were set to infinite for ray tracing simulation. By using our simulation method combined all these optical parameters, we obtained the results of enhancement ratio of EQE by using the organic MLAs applying to the inverted TEOLEDs. The simulated enhancement ratio of the OLEDs with the 30, 50, and 70 nm thick EILs are displayed in Figure 2.7 as functions of the refractive index and fill-factor of MLAs. The extraction efficiencies increase as the refractive indices of the extraction structures approach the underlying organic materials due to the reduction of the reflection at the interfaces. In addition, when the refractive index of MLAs increase larger than organic materials, enhancement ratio showed a decreasing trend which caused by the reflectance change from the electric and magnetic field distribution on incident angle as a function of a refractive index of MLAs. As a result, when giving the point about 1.8 of refractive index of MLAs matched with the

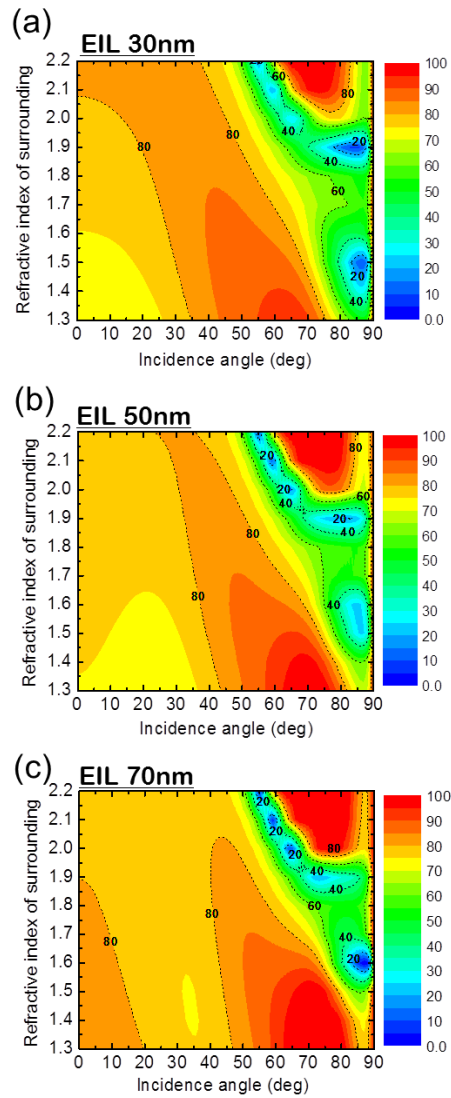


Figure 2.5 Calculated results of angle dependent reflectance of the OLEDs with metal electrode as a function of refractive index of ambient surrounding and incident angle. (a) (b) and (c) are calculated reflectance results from the devices with the 30, 50, and 70 nm thick EILs, respectively.

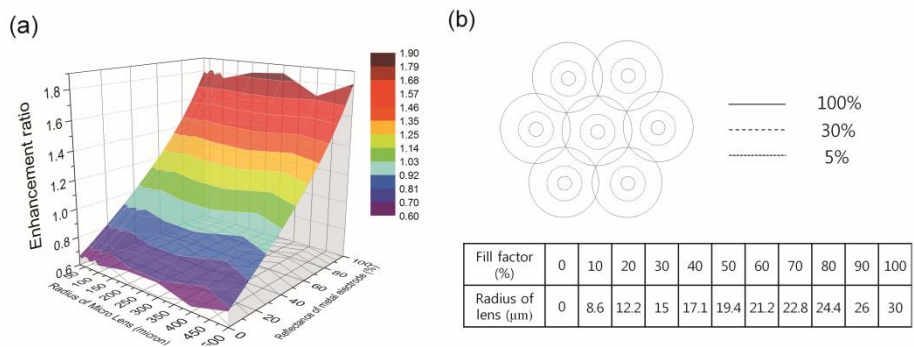


Figure 2.6 (a) Simulation results of enhancement ratio of radiant flux as a function of radius of fully packed MLAs (b) values of radius of micro lens for calculation of fill-factor of MLAs

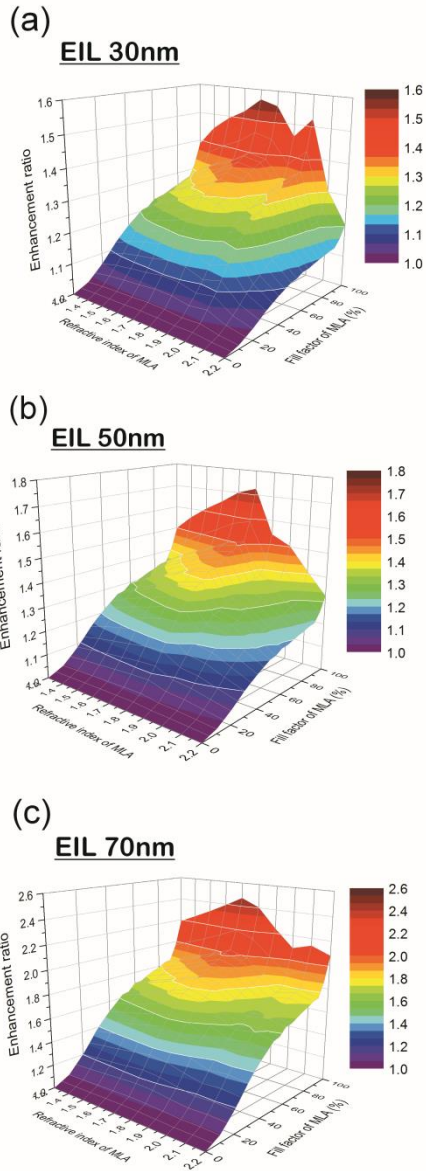


Figure 2.7 Simulation results of outcoupling enhancement ratio by light extraction structures as functions of the refractive index and fill-factor of MLAs. (a) (b) and (c) are the results from the devices with the 30, 50, and 70 nm thick EILs, respectively.

refractive index of α -NPD at 550 nm, we achieved 1.55, 1.74, and 2.43 times of enhancement ratio, corresponding to 42.8, 34.8, and 12.2% of the EQEs for the device with 30, 50 and 70 nm thick EILs.

2.4 Conclusion

In conclusion, an analytic simulation method for light extraction from TEOLEDs with MLAs has been developed. We combined two simulation methods of the classical dipole model and ray tracing model including the angle dependent reflectance property of device with metal electrode. Interference effect between dipole emitter and metal reflector changing the angle dependent spectra and intensity distribution was investigated from the oscillating dipole model considered to the PL spectra and molecular horizontal orientation ratio of the emitter. Based on these results of the emitted angle dependent properties, light extraction enhancement ratios of EQEs were simulated by Monte Carlo ray tracing simulation as functions of refractive indices and fill-factors of MLAs.

Chapter 3 Transparent top electrode based inverted top emitting organic light emitting diodes

3.1 Optical characteristics of transparent top electrode based inverted top emitting OLEDs

3.1.1 Introduction

Organic light emitting diodes (OLEDs) have shown great potential for flat panel displays and solid state lighting applications.⁵¹⁻⁵² Recently OLEDs are moving toward flexible displays on plastics where low temperature processing is preferred.⁵³⁻⁵⁶ Oxide thin film transistors are a choice as the backplane for the purpose because they offer low temperature and easy process compared to low temperature polysilicon. Inverted OLEDs with a bottom cathode are preferred in the case because oxide semiconductors are n-type.⁵⁷⁻⁶¹ In addition, top emitting OLEDs (TEOLEDs) are preferred in small size high resolution active matrix displays to increase the aperture ratio, thereby to reduce the operating luminance and increase lifetime. Strong microcavity structures composed of a thick metal bottom electrode and a semitransparent thin metal top electrode are mostly used.⁶²⁻⁶⁵ The strong microcavity structure results in narrowing of emission spectra, which is beneficial to display applications. One drawback of the strong microcavity structure is the variation of the emission color with viewing angle. The strong viewing angle dependent color

change can be relaxed by increasing the transmittance of the top electrode and various methods have been developed for the purpose including the use of (i) a capping layer on the top electrode⁶⁶⁻⁶⁹ and (ii) a transparent oxide conductor with a buffer layer such as WO₃, ZnO, Pentacene, copper phthalocyanine to protect the underlying organic layers from sputter damage⁷⁰⁻⁷⁴ but with limited success. It is rather difficult to satisfy the requirements of the electrical and optical characteristics of the devices at the same time using the methods. Recently, we demonstrated that 1,4,5,8,9,11-hexaazatriphenylene-hexacarbonitrile (HATCN) is very effective as a buffer layer to protect underlying organic layers and to have excellent hole transporting ability even after the sputter deposition of indium zinc oxide (IZO) for transparent OLEDs.⁷⁵⁻⁷⁸

In this chapter, we report a high efficiency inverted TEOLED with excellent color stability by using indium zinc oxide as the top electrode and HATCN as the buffer layer. An exciplex-forming co-host system doped with the green dopant bis(2-phenylpyridine)iridium(III) acetylacetonate [Ir(ppy)₂acac] was adopted as the emitting layer (EML) in the device.^{8,24,79} The inverted TEOLED showed an external quantum efficiency (EQE) of 23.4% at 1,000 cd/m² corresponding to the current efficiency of 110 cd/A with the variation of $\Delta x=0.02$, $\Delta y=0.02$ in the CIE 1931 coordinates for the viewing angles between 0 and 60°. Moreover, the device showed low efficiency roll-off with the EQE value of 21% and the luminous efficiency of 98 cd/A at 10,000 cd/m².

3.1.2 Experiment

Figure 3.1a and b show the structure of the inverted TEOLEDs and the chemical structure of the materials used for the devices. A 70 nm thick Al metal cathode and organic layers were successively deposited at a base pressure of $< 5 \times 10^{-7}$ Torr by thermal evaporation without breaking the vacuum. 15wt% rubidium carbonate (Rb_2CO_3) doped bis-4,6-(3,5-di-3-pyridylphenyl)-2-methylpyrimidine (B3PYMPM) was used as a n-doped electron injection layer (EIL) and undoped B3PYMPM was used as an electron transport layer (ETL). Co-deposited B3PYMPM and 4,4',4''-tris(N-carbazolyl)-triphenylamine (TCTA) with the 1:1 ratio and doped with 8wt% $\text{Ir}(\text{ppy})_2\text{acac}$ were used as an emission layer (EML) to exploit the exciplex forming character of the materials.^{8,24,79} Undoped 1,1-bis-(4-bis(4-methylphenyl)-amino-phenyl)-cyclohexane (TAPC) and TAPC doped with 8 wt% rhenium oxide (ReO_3) were used as a hole transport layer and a p-doped hole injection layer (HTL, HIL), respectively. A 50 nm thick HATCN layer was deposited to protect the underlying organic layers from the plasma damage and have good hole-injection properties from the sputter deposited IZO top electrode. OLEDs using a thin Ag top electrode were also fabricated to compare with the OLEDs based on the TCO top electrode. The device structures were optimized prior to the fabrication of the inverted TEOLEDs using the classical dipole model to maximize luminous intensity in the normal direction which is proportional to the current efficiency. The current density-voltage-luminance (J-V-L) characteristics of the devices were measured using a Keithley 2400 semiconductor parameter analyzer and a Photo Research PR 650 spectro-photometer. Angular-dependent EL spectra were measured using an optical fiber and an S2000 miniature fiber optic spectrometer (Ocean Optics).

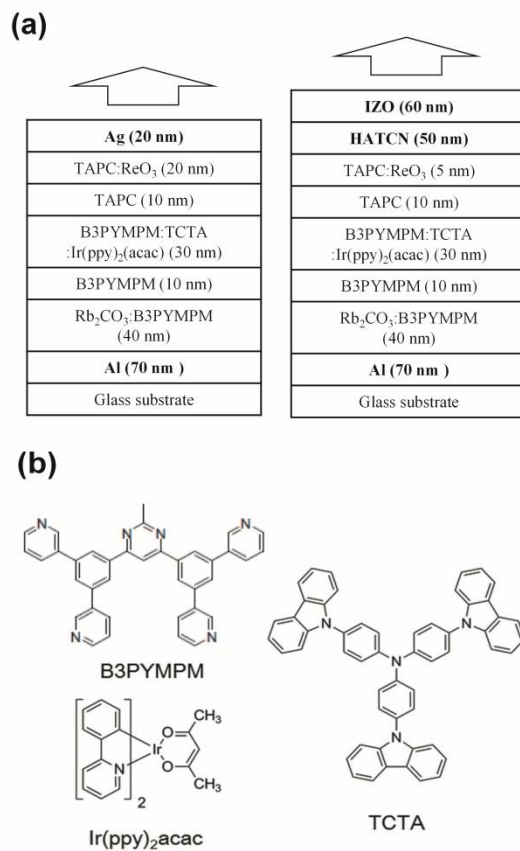


Figure 3.1 (a) Device structures of inverted TEOLEDs with Ag (left) and IZO (right) top anodes, respectively. (b) Molecular structures of organic materials in the emitting layer.

3.1.3 Results and Discussion

The performances of the devices were firstly simulated using the classical dipole model.^{41,42} Figure 3.2 shows the simulated relative EQEs (a, c) and the relative current efficiency (b, d) of the devices with the Ag (a, b) and the IZO (c, d) top electrodes as contour plots as functions of the thickness of the

EIL and HIL, while the thickness of intrinsic ETL and HTL fixed 10nm. The inset figures display the simulated spectral changes with viewing angle for the OLEDs with the maximum efficiencies. One can note that the maximum EQE is obtained at the different thicknesses of the EIL and HIL from the thicknesses giving the maximum current efficiency in the device with the Ag top electrode (Figure 3.2a and b). The color variation with viewing angle is more significant for the device with the highest EQE than the device giving the highest current efficiency. These results indicate that it is difficult to maximize the EQE with little variation of color with viewing angle if a thin metal is used as the top electrode. Based on the simulation results, we fabricated the device with the structure corresponding to the maximum current efficiency where the thicknesses of the EIL and HIL are 40 nm and 20 nm, respectively. On the other hand, the maximum EQE and the maximum current efficiency in the transparent top electrode based OLEDs were obtained from the similar device structure with the thicknesses of the EIL and HIL of 40 nm and 5 nm, respectively and the color variation is much less than the devices with the Ag top electrode as shown in Figure 3.2c and d.

Figure 3.3a shows the J-V-L characteristics of the optimized OLEDs with the IZO and the Ag top electrodes. Both OLEDs showed similar turn on voltages of 2.4 V and 2.5 V, respectively. The IZO-based inverted TEOLED exhibits

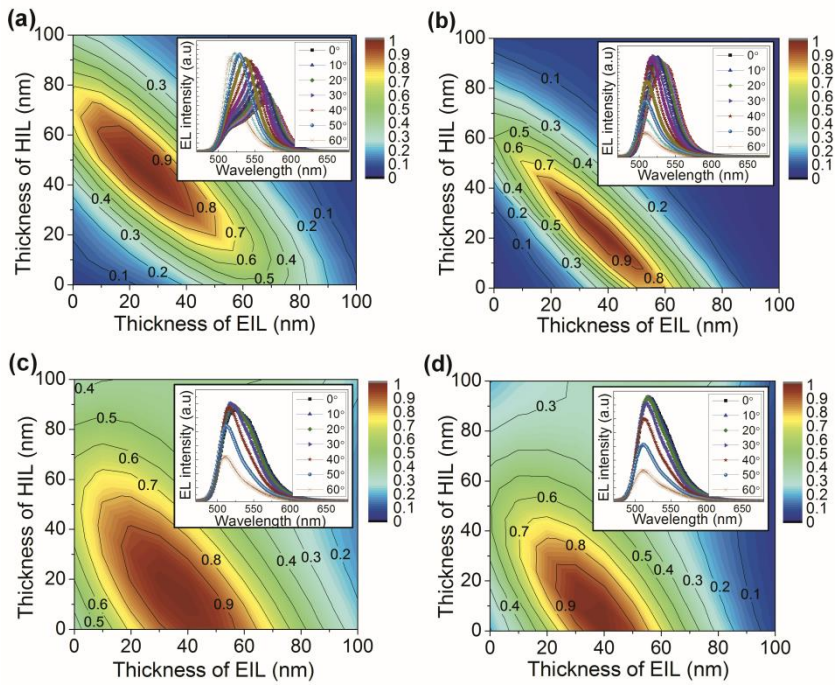


Figure 3.2 Contour plots of efficiency of the inverted TEOLEDs as functions of the thicknesses of n-doped electron injection layer (EIL) and p-doped hole injection layer (HIL); relative external quantum efficiencies (a,c) and relative current efficiencies (b, d) for the device with Ag (a,b) and IZO (c, d) top anodes, respectively.

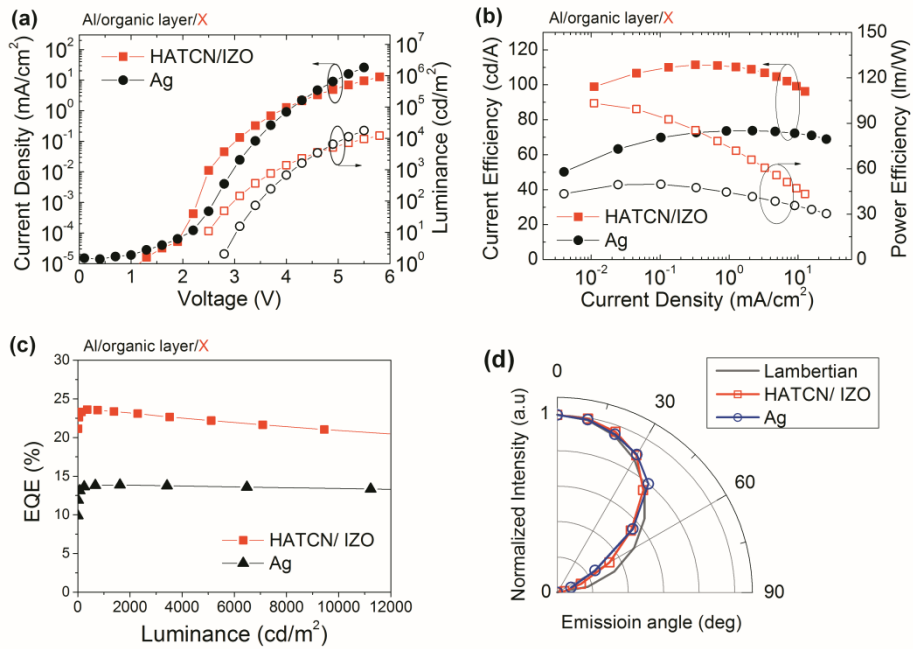


Figure 3.3 Electrical and optical characteristics of inverted TEOLEDs; (a) current density–voltage–luminance (J–V–L) characteristics, (b) current and power efficiencies against current density, (c) external quantum efficiencies and (d) normalized electroluminescent intensities at different viewing angles which are compared with a Lambertian emitter.

higher current density and luminance from 1 to 1000 cd/m² and lower turn-on voltage than the Ag-based device, demonstrating the good hole injection property of HATCN for the inverted OLED even after the sputtering process of IZO. Figure 3.3b represents the current and power efficiency of the devices with the IZO and Ag top electrodes. The IZO-based device exhibited the current efficiency of 110 cd/A, 75 lm/W at 1000 cd/m² and 98 cd/A, 46 lm/W at 10,000 cd/m². At the same time, high EQE of 23.4% was obtained from the IZO-based device (Fig. 3.3c). On the other hand, the Ag-electrode based device showed lower efficiencies of 73 cd/A, 43 lm/W at 1000 cd/m², and 71 cd/A, 34 lm/W at 10,000 cd/m² with the optimized thicknesses of EIL and HIL. The maximum EQE was only 13.8%. The low EQE might come from the device structure which was optimized for the current efficiency along with the poor electrical balance. Both devices showed narrower angular distributions of intensity with viewing angle than the Lambertian pattern with the Lambertian correction factor of 0.83 and 0.77 for the IZO and Ag-based devices, respectively (Fig. 3.3d). The power efficiency and external quantum efficiency of the devices were calibrated using the viewing angle-dependent electroluminescent (EL) intensity and spectra. Performances of the devices are summarized in Table 3.1.

Figure 3.4a and b show the spectral changes with viewing angle of the IZO and Ag-based inverted TEOLEDs. The IZO-based TEOLED exhibited almost the same emission spectra independent of viewing angle. On the other hand, the device with the Ag top anode showed large spectral variation with viewing angle. The changes of the CIE 1931 coordinates of the devices as the viewing angle varies from 0 to 60° are displayed in Figure 3.4c. The device with the Ag top anode showed $\Delta x=0.08$ and $\Delta y=0.03$. On the other hand, the device

Table 3.1 Performances of inverted TEOLEDs with Ag and IZO top electrodes

Top Electrode	Turn-on voltage (V)	@ 1000 cd/m ²				
		Driving voltage (V)	EQE (%)	Current Efficiency (cd/A)	Power Efficiency (lm/W)	Lambertian factor
IZO	2.4	3.8	23.4	110	75	0.83
Ag	2.5	4.2	13.8	73	43	0.77

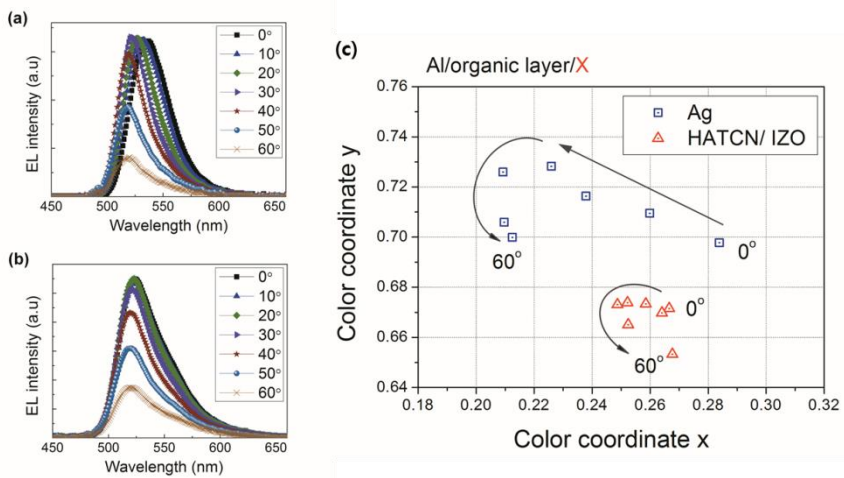


Figure 3.4 Angle dependent EL spectra of TEOLEDs with Ag (a) and IZO (b) top anodes. (c) Variation of CIE 1931 coordinates (x,y) with viewing angle for inverted TEOLEDs with Ag (rectangle) and IZO (triangle) top electrodes, respectively.

with the IZO top electrode exhibited small change with $\Delta x=0.02$ and $\Delta y=0.02$. These results assure that the inverted TEOLEDs using the IZO top electrode significantly improve the efficiency and the color stability with viewing angle simultaneously.

3.1.4 Conclusion

In conclusion, we demonstrated a highly efficient inverted phosphorescent green TEOLED with the EQE of 23.4% and the current efficiency of 110 cd/A at 1,000 cd/m² and low efficiency roll-off up to 10,000 cd/m² by using an IZO top electrode. In addition, the OLED with the IZO top electrode showed much better color stability with viewing angle than the OLED with the Ag top electrode. The results clearly indicate that a transparent top electrode performs much better than the thin metal top electrode for top emission OLEDs in terms of efficiency and color stability. In addition we demonstrated that the HATCN/sputtered IZO electrode is adequate as the transparent top electrode for efficient inverted top emission OLEDs.

3.2 Transparent top electrode based inverted top emitting OLEDs using a horizontally oriented emitter

3.2.1 Introduction

Top emitting organic light emitting diodes (TEOLEDs) have shown interests in solid state lighting and display. Especially, the research of inverted TEOLEDs with a bottom cathode is important for the future applications adopting metal foil substrate for roll to roll process or the display backplane using n-type oxide thin film transistors.^{67,71,80-82} In recent years, orientation of the transition dipole moments of an emitter is considered as an important factor influencing the quantum efficiency and the out-coupling efficiency in OLEDs. Numerous papers have demonstrated that horizontally oriented emitting dipoles result in higher outcoupling efficiency than vertically oriented dipoles due to the change of the electromagnetic field distribution of the dipole oscillations.⁸³⁻⁸⁸ Not only spin coated polymers but also vacuum evaporated fluorescent and phosphorescent emitters were reported to have preferred horizontal orientation, which enhances the outcoupling efficiency of OLEDs.^{8,24,79,89-91} Recently our group reported high efficiency bottom emission OLEDs with external quantum efficiencies (EQEs) over 30% by doping heteroleptic iridium complexes having high quantum yield and horizontal orientation of transition dipole moments in exciplex co-host systems.⁷⁵⁻⁷⁸

In this chapter, we report a highly efficient inverted TEOLED using an exciplex-forming co-host system doped with the horizontally oriented

phosphorescent green dopant bis(2-phenylpyridine)iridium(III)(2,2,6,6-tetramethylheptane-3,5-diketonate) [Ir(ppy)₂tmd]. The emitter has a preferred orientation of the transition dipole moment in the emitting layer (EML) with the horizontal to vertical transition dipole ratio of 0.78:0.22 and the photoluminescence quantum yield (PLQY) of 96%⁹². The device showed an external quantum efficiency (EQE) of 27.6% at 1,000 cd/m² and the current efficiency of 120.7 cd/A. Moreover, the device showed low efficiency roll-off with the EQE value of 24.5% and the luminous efficiency of 107.6 cd/A at 20,000 cd/m².

3.2.2 Experiment

Figure 3.5a and b show the device architecture of the inverted TEOLEDs and the chemical structure of the materials used for the devices. A 70 nm thick Al metal cathode and organic layers were successively deposited at a base pressure of $< 5 \times 10^{-7}$ Torr by thermal evaporation without breaking the vacuum. 15 wt% rubidium carbonate (Rb₂CO₃) doped bis-4,6-(3,5-di-3-pyridylphenyl)-2-methylpyrimidine (B3PYMPM) was used as a n-doped electron injection layer (EIL) and undoped B3PYMPM was used as an electron transport layer (ETL). Co-deposited B3PYMPM and 4,4',4''-tris(N-carbazolyl)-triphenylamine (TCTA) with the 1:1 ratio and doped with 8wt% Ir(ppy)₂tmd (0.46:0.46:0.08 molar ratio) were used as an EML to take advantage of the exciplex forming character of the materials.^{8,24,79,89-91} Undoped 1,1-bis-(4-bis(4-methyl-phenyl)-amino-phenyl)-cyclohexane (TAPC) and TAPC doped with 8 wt% rhenium oxide (ReO₃) were used as a hole transport layer and a p-doped hole injection layer (HTL, HIL), respectively. A

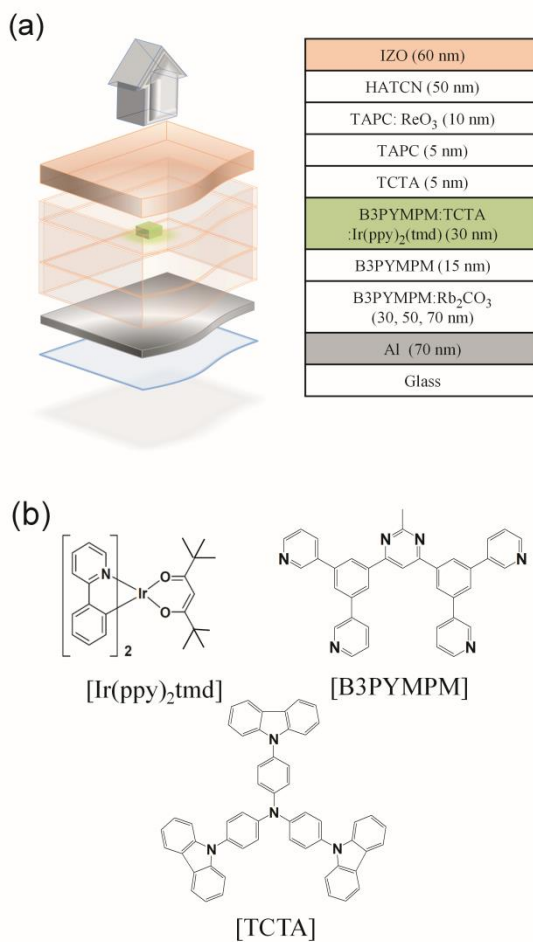


Figure 3.5 Schematic diagram of the inverted TEOLEDs (a) device structures of inverted TEOLEDs (b) Molecular structures of organic materials in the emitting layer.

50 nm thick HATCN layer was deposited to protect the underlying organic layers from the plasma damage and have good hole-injection properties from the sputter deposited IZO top electrode.⁷⁵⁻⁷⁸ The device structure was optimized prior to the fabrication of the inverted TEOLEDs using the classical dipole model.^{41,42} The current density-voltage-luminance (J-V-L) characteristics of the devices were measured using a Keithley 2400 semiconductor parameter analyzer and a Photo Research PR 650 spectrophotometer. Angular-dependent EL spectra were measured using an optical fiber and an S2000 miniature fiber optic spectrometer (Ocean Optics).

3.2.3 Results and Discussion

Figure 3.6a exhibits a simulated contour plot of the relative maximum achievable luminous intensity in the normal direction as functions of the thickness of EIL and HIL. The simulation results indicate that the highest current efficiency can be obtained with the EIL and HIL thicknesses of 30 nm and 10 nm, respectively with the fixed thicknesses of B3PYMPM (15 nm), TCTA (5 nm), and TAPC (5 nm), respectively. Figure 3.6b shows the current density-voltage-luminance (*J-V-L*) characteristics of the inverted TEOLEDs with the 30 nm, 50 nm, and 70 nm thick EILs, respectively. The device with the 30 nm thick EIL showed the highest luminance, which is consistent with the simulation result. The turn-on voltage of the optimized device was 2.8 V at 22 cd/m² and the driving voltages were 4.0 V and 5.8 V at 1,000 cd/m² and 10,000 cd/m², respectively. The electroluminescence spectra in the normal direction and angle dependent intensity distribution of the devices matched

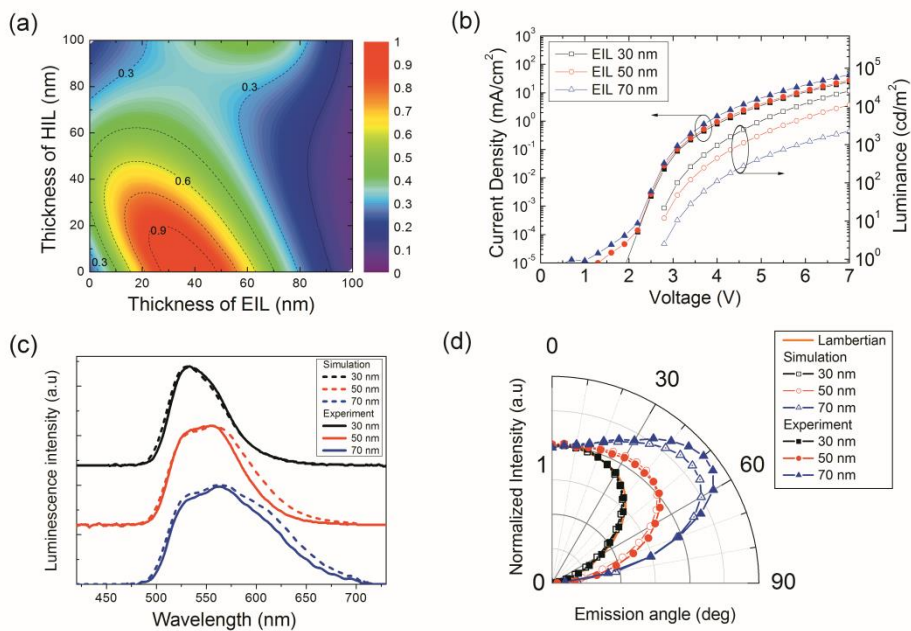


Figure 3.6 Electrical and optical characteristics of inverted TEOLEDs; (a) contour plots of relative current efficiencies of the inverted TEOLEDs as functions of the thicknesses of EIL and HIL (b) current density–voltage–luminance (J–V–L) characteristics, (c) normalized luminescent spectra of the devices with 30, 50, and 70 nm thick EILs: simulated (dashed lines) and measured (solid lines) values (d) normalized angle dependent intensity distributions of the devices: simulated (filled symbols) and measured (open symbols) values

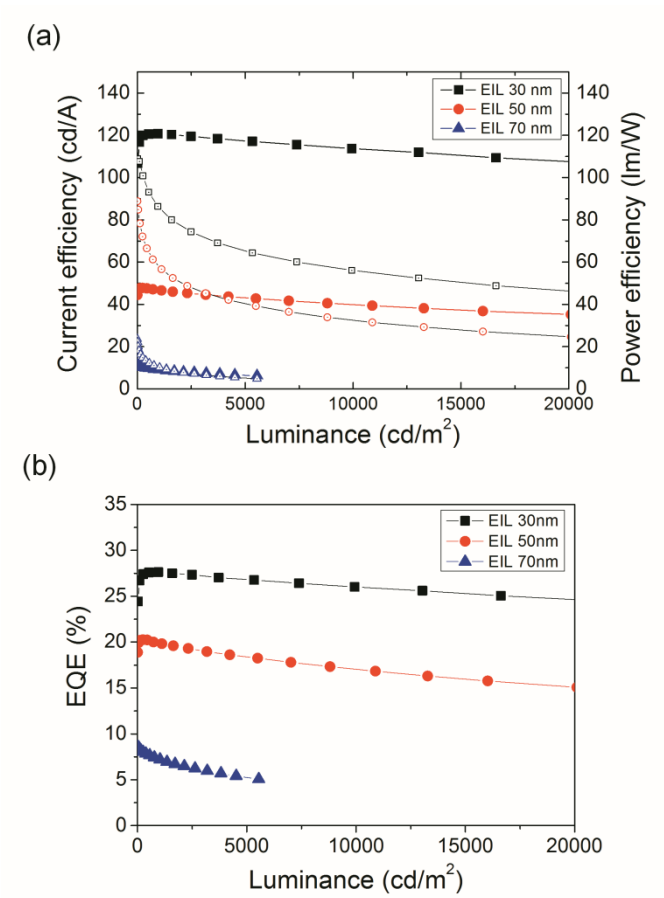


Figure 3.7 Performances of inverted TEOLEDs (a) current efficiencies against current density (b) power efficiencies and external quantum efficiencies against luminance

Table 3.2 Performances of inverted TEOLEDs

	EIL 30 nm		EIL 50 nm		EIL 70 nm	
	1,000 cd/m ²	10,000 cd/m ²	1,000 cd/m ²	10,000 cd/m ²	1,000 cd/m ²	10,000 cd/m ²
EQE (%)	27.6	26.0	20.0	17.0	7.2	-
P.E (lm/W)	85.9	56.0	48.6	32.5	10.2	-
C.E (cd/A)	120.7	113.7	46.8	39.9	9.1	-
Lambertian factor	0.91		1.49		1.97	

very well with the simulation results as shown in Figure 3.6c and d, respectively. Some discrepancy between them might come from the shift of emission zone in the devices depending on the thickness of the ETL and/or optical birefringence of organic materials which has not been considered in our optical modeling. Figure 3a represents the current and power efficiency of the inverted TEOLEDs. The optimized device with 30 nm thick EIL exhibited the current and power efficiencies of 120.7 cd/A and 85.9 lm/W at 1,000 cd/m² and 113.7 cd/A, 56 lm/W at 10,000 cd/m². The device also showed high EQEs of 27.6% at 1,000 cd/m² and 26.0% at 10,000 cd/m² (Figure 3.7b). Moreover, the efficiency roll off is small with the current efficiency of 107.6 cd/A, the power efficiency of 46.4 lm/W, and the EQE of 24.6% at 20,000 cd/m². The power efficiency and external quantum efficiency of the devices were calibrated using the viewing angle-dependent electroluminescent (EL) intensity and spectra. Log scale plots of the efficiencies can be found in Supplementary Information (Figure S1) to get more information on the region of low luminance. Performances of the devices are summarized in Table 3.2.

Optical simulation of the EQE of the devices was performed using the experimentally obtained values of PLQY=0.96 and Θ =0.78. The PL quantum yield was measured using an integrating sphere^{93,94} and the sample consisted of a 50 nm thick emitting layer (TCTA:B3PYMPM:Ir(ppy)₂(tmd), 1:1 molar ratio and 8 wt%) on a quartz substrate. Figure 3.8 represents the maximum achievable EQEs from the optically optimized device structure as a function of PLQY and Θ of the emitter under the assumption of negligible electrical loss (Γ). The simulation predicted that EQE of 31.9% is achievable if there is no electrical loss in the device. Our experimental result of 27.6% EQE indicates that the device has electrical loss of 13.5%, which can be further

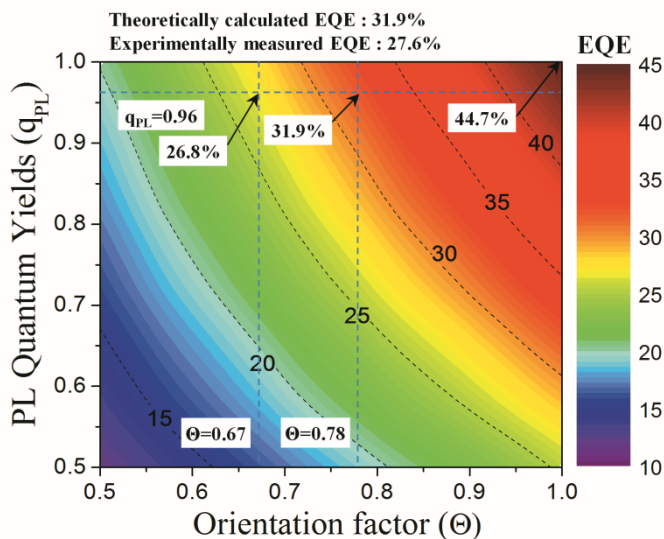


Figure 3.8 Contour plots of the simulation results of EQE of the inverted TEOLED as a function of q_{PL} and Θ with the theoretical maximum value. The dashed lines indicate the EQEs with $q_{PL} = 0.96$ and $\Theta = 0.67$ (isotropic), 0.78 (Ir(ppy)₂tmd), respectively.

improved with optimization. One can note that a maximum EQE of 44.7% can be obtained in inverted TEOLEDs even with a dye of PLQY=1 and $\Theta=1$.

3.2.4 Conclusion

In conclusion, we demonstrated a highly efficient inverted phosphorescent green TEOLED with the EQE of 27.6%, the current efficiency of 120.7 cd/A, and the power efficiency of 85.9 lm/W at 1,000 cd/m² and low efficiency roll-off up to 20,000 cd/m² by using an horizontally oriented emitter in an exciplex forming co-host system. The efficiencies are the highest ones reported up to now to our best knowledge. Optical simulation showed that there is still a margin to improve reaching up to EQE of 32% through further optimization of the structure of TEOLEDs.

Chapter 4 Inverted top emitting white organic light emitting diodes with high color quality by using broadband anti-reflection top electrode

4.1 Introduction

White organic light emitting diodes (WOLEDs) have great interests as the promising application for the flat panel display and solid state lighting. In particular, inverted top-emitting WOLEDs have an importance to realize a highly efficient device with a higher aperture ratio and compatibility with n-type oxide thin film transistors (TFTs).⁵⁷⁻⁶¹ In WOLEDs, quality of the color has also been an important issue as well as the light emission efficiency. Especially, top emitting OLEDs (TEOLEDs) are crucially influenced by the upper electrode where the emitted light passes through. Semitransparent thin metal top electrode based TEOLEDs have been intensively researched.⁶²⁻⁶⁵ However, these methods generally have narrow bandwidth with strong angle dependence, resulting unacceptable color shift due to a strongly resonant microcavity effect. Applying metal oxide or organic capping layer on the thin metal electrode or using dielectric/ metal/ dielectric (DMD) system rather relax the resonant cavity effect and increase the transparency of top electrode but with limited success.⁶⁶⁻⁷⁴ By using the stacked tandem structures, the difference of wavelength dependent optical property can be slightly reduced by controlling the optical path length from optimization of the device

architecture. However, the device must have a lot of layers, including the complicated optimization process into much more expensive than a single junction white device. In the device structure of a single junction white TEOLEDs, in order to obtain a high efficiency and high color quality at the same time, spectral distortion influenced by device geometry must be minimized for all visible wavelength range. Promising way to realize the highly efficient TEOLEDs with the high color quality is to maximize the transmission of the top electrode, minimizing the reflection and absorption without wavelength dependency.

First, we studied the effect of applying dielectric capping layer for TCO top electrode based TEOLEDs. External quantum efficiency (EQE) and spectral property were investigated as functions of refractive index and thickness of capping layer through the experiment and simulation. Especially, single layer anti-reflection condition from a low index capping layer (experimental results from LiF 100 nm capping layer) shows extreme relaxation of spectral change from resonance effect through all visible wavelength range maintaining high EQE. We experimentally fabricated the phosphorescent green TEOLEDs with 100 nm thick LiF capping layer having the EQE of 27% at 1,000 cd/m² and deviation of color coordinate is $\Delta x = 0.01$, $\Delta y = 0.01$ as the viewing angle changes from 0° to 60°. The results of angle dependent intensity distribution and spectral change on viewing angle showed very great agreement with the results of the theoretical calculation. As the same processing, we additionally investigated the devices applying LiF 100 nm single anti reflection layer on top of the phosphorescent red and blue devices, resulting in the deviation of color coordinate with $\Delta x = 0.01$, $\Delta y = 0.01$ from red device, $\Delta x = 0.01$, $\Delta y = 0.02$ from blue device maintaining high EQEs. The results represent that

applying single layer anti-reflection coating on IZO top electrode based TEOLEDs is an effective method for achieving high efficiency and good angle dependent color property simultaneously through all visible wavelength range.

Second, we fabricated highly efficient and high color quality white TEOLEDs by using very low reflectance of top side electrode in all visible wavelength range, where the single layer broadband AR coating on the top of the TEOLEDs. The broadband AR layer reduced the reflectance of the top electrode for all visible wavelength range under 4%. Therefore, angle dependent spectral change of white emission was relaxed. We fabricated two types of the white TEOLEDs according to the distribution of charge carriers between orange and blue emitters by controlling the configuration of electron transport materials (ETM) in exciplex co-host system. Interestingly, the single junction white TEOLEDs with the broadband AR layer showed small variation of spectral change on viewing angles of $dx=0.02$, $dy=0.01$ at $0 \sim 60^\circ$ compared to the reference device of $dx =0.15$, $dy=0.05$ for W1 (17wt% of B3PYMPM in buffer layer) and $dx=0.14$, $dy=0.03$ for W2 (15wt% of B3PYMPM in buffer layer). Furthermore, the single junction white TEOLEDs with the broadband AR layer showed the external quantum efficiencies increase due to the relaxation of the resonance effect of the device structure. As results, the EQEs of 18.8% and 16.9% for W1 and W2 of the single junction white TEOLEDs were realized with the small color variation on viewing angles, resulting in the duv values of $-0.0014\sim 0.0009$ and $0.0041\sim 0.0058$ at $0\sim 60$ degrees. Correlated color temperatures of W1 and W2 were $\sim 2200\text{K}$ and $\sim 3000\text{K}$ satisfied with the blackbody radiation white within 5 steps of MacAdam ellipse for the requirement of the solid state lighting

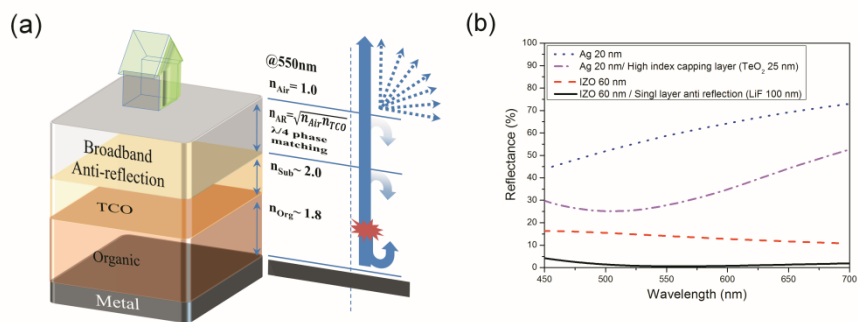


Figure 4.1 (a) Schematic diagram of transparent conducting oxide top electrode based inverted TEOLED with broadband anti-reflection coating (b) reflectance data of Ag 20 nm, Ag 20 nm with TeO₂ 25 nm capping layer, IZO 60 nm, IZO 60 nm with LiF 100 nm capping layer.

application.

4.2 Optical simulation analysis

Figure 4.1a shows the schematic diagrams of the structure of the TEOLED with a broadband anti-reflection layer on the top of the TCO top electrode. Reflectance of four types of top electrode was calculated: Ag 20 nm, Ag 20 nm with high index capping layer (TeO_2 25 nm, $n \sim 2.3$ @ 550 nm), IZO 60 nm, IZO 60 nm with the single layer AR layer (LiF 100 nm, $n \sim 1.4$ @ 550 nm). TeO_2 was representatively chosen for the high refractive capping layer based on the results of the previous researches from other groups. LiF was chosen for square root configuration of broadband single layer anti-reflection condition between IZO and air. LiF 100 nm thick was chosen for $\lambda/4$ phase matching condition in the middle of the wavelength range in visible light. [ref] Incident light was set in the refractive index of $n \sim 1.8$ as an approximation of the refractive index of organic materials propagating through the top electrode to the air. The device with IZO 60 nm with the single layer AR coating shows extremely low reflectance under 1~4% over the entire wavelength range in visible light as shown in Figure 1b.

Figure 4.2 shows the wavelength dependency of spectral characteristics of the devices with four types of top electrode. The structures of all devices were designed from the classical dipole model simulation for the optimized maximum efficiency, basically the same device architectures in chapter 3.2. The emission zone was assumed to be located at the center of the emitting layer and the emission intensity was considered as a constant value between

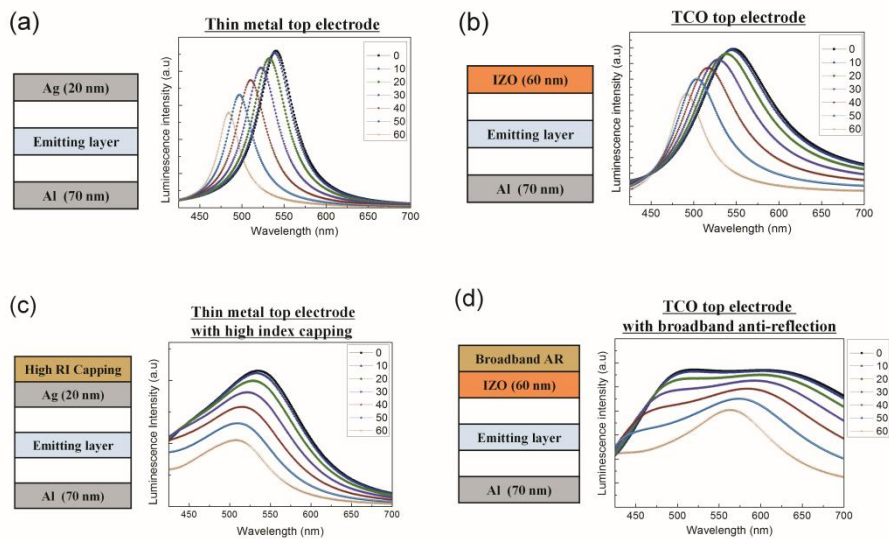


Figure 4.2 The comparison of the angle dependent spectral change influenced by the top electrode system and device structure. (under the assumption of constant quantum yield in all visible wavelength regions) The calculated results of the device with (a) Ag 20 nm, (b) IZO 60 nm, Ag 20 nm with the high refractive index capping layer, and (d) IZO 60 nm with the low refractive index capping layer of single layer anti-reflection condition of top electrode system based TEOLEDs.

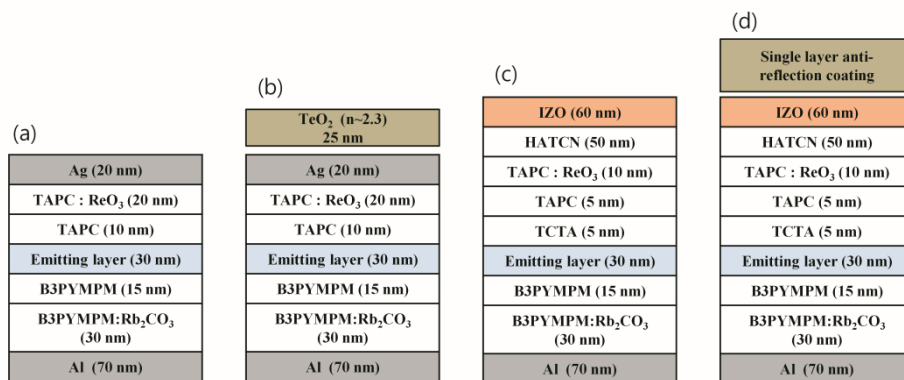


Figure 4.3 The device structures of four types of TEOLEDs used for the optical analysis of the wavelength-dependent intensity characteristics. (a) Ag 20 nm, (b) Ag 20 nm with TeO₂ 25 nm, (c) IZO 60 nm, (d) IZO 60 nm with single layer anti-reflection coating top electrodes based inverted TEOLEDs.

400 nm and 700 nm. The complex refractive indices of all organic materials were measured by the spectroscopic ellipsometer. Specific device structures are informed in figure 4.3. The change of the out coupled luminescence intensity influenced by the device geometry were calculated and represented in Figure 4.2a-d as function of wavelength in visible range with the multiple viewing angles. Interestingly, the device with the broadband single layer AR coating (LiF 100 nm) on top of the IZO electrode showed small changes of the luminescence intensity against wavelength and viewing angle. The results illustrate that the spectral change influenced by the different optical path length from the device structures is minimized by using common single layer on top of the IZO top electrode based TEOLEDs.

We carried out the optical simulation for angle dependent spectral property of phosphorescent blue, green, red top emitting OLEDs. The external quantum efficiency of the top emitting OLEDs was calculated as functions of the thickness and refractive index of capping layer in the case of blue, green, red devices. As shown in Figure 4.4, the devices with the ideal refractive index for anti-reflection of ~ 1.4 and ~ 100 nm thick capping layer show maintaining the highest optimized EQE values. As results, the device shows extremely small color change with the variation of $\Delta x=0.01$, $\Delta y=0.02$ for blue, $\Delta x=0.01$, $\Delta y=0.01$ for green, $\Delta x=0.01$, $\Delta y=0.01$ for red and in the CIE 1931 coordinates as the viewing angle changes from 0 to 60° (Figure 4.5) In addition, this optical property of single layer anti-reflection gives electroluminescence (EL) spectra closer to the intrinsic photoluminescence (PL) spectra of emitter materials. Figure 4.6 represents the comparison PL spectra of RGB emitters and EL spectra from the device with LiF 100 nm capping layer, which are matched with each other through all visible wavelength range.

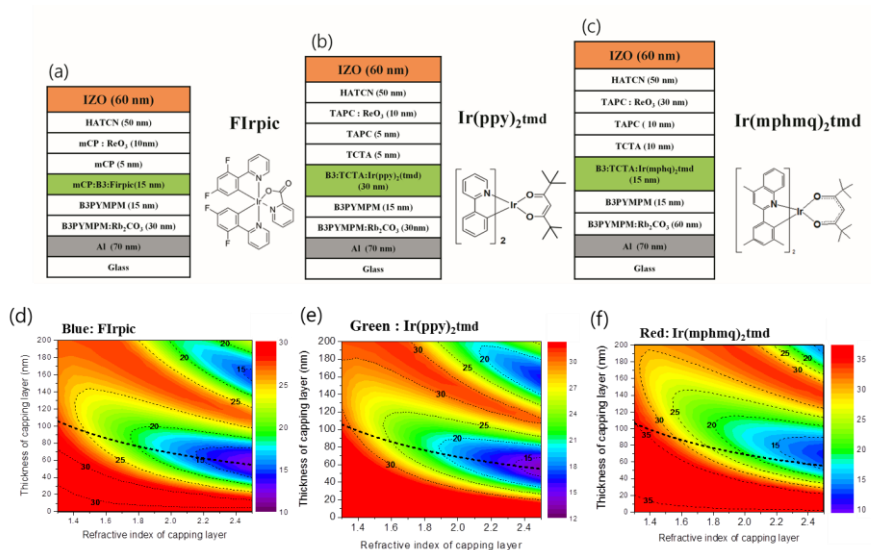


Figure 4.4 Device structures of phosphorescent blue, green, and red inverted TEOLEDs and molecular structures of the emitters represent (a), (b), and (c), respectively. External quantum efficiency influenced by capping layer in transparent conducting oxide top electrode based TEOLEDs. Simulation results of (a) the phosphorescent blue emitter of FIrpic. Quantum yield ($q_{PL} = 1$), the horizontal orientation factor ($\Theta = 0.76$). (b) the phosphorescent green emitter of Ir(ppy)₂tmd. Quantum yield ($q_{PL} = 0.96$), the horizontal orientation factor ($\Theta = 0.78$). (c) the phosphorescent red emitter of Ir(mphmq)₂tmd. Quantum yield ($q_{PL} = 0.96$), the horizontal orientation factor ($\Theta = 0.82$). Black dotted line through the contour plot is calculated thicknesses of $\lambda/4$ phase matching @ 550 nm according to the refractive index.

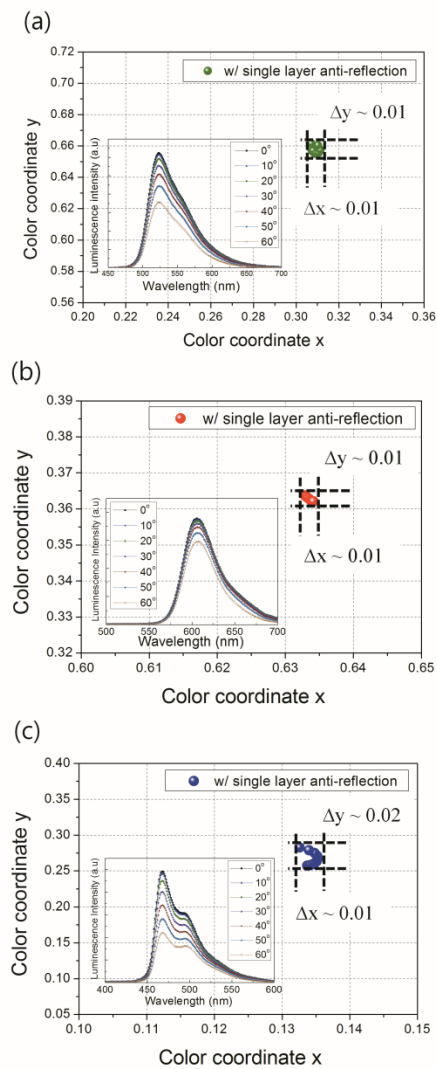


Figure 4.5 Angle dependent spectral and color coordinate characteristics of RGB inverted TEOLEDs. (a) Phosphorescent green emitter of Ir(ppy)₂tmd, (b) phosphorescent red emitter of Ir(mphmq)₂tmd, (c) phosphorescent blue emitter of FIrpic.

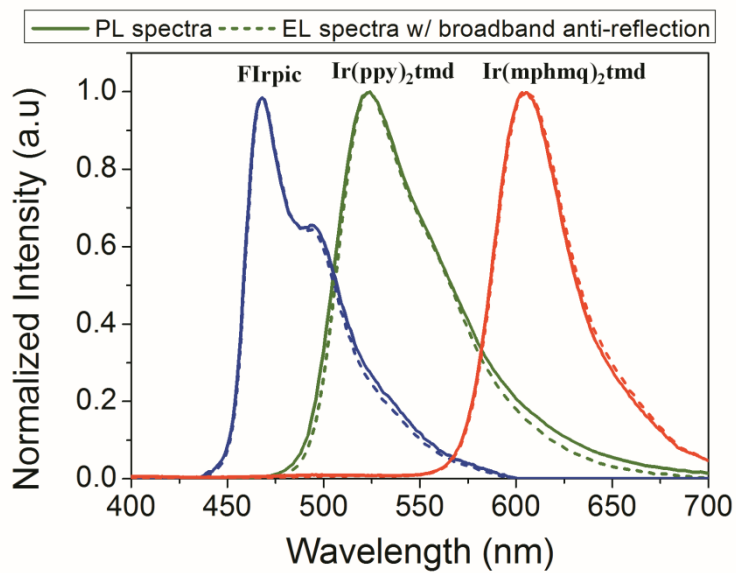


Figure 4.6 The comparison between photoluminescent and electroluminescent spectral characteristics of the TCO top electrode based TEOLEDs with broadband anti-reflection.

4.3 Experiment

Figure 4.7a and b show the device architecture of the inverted white TEOLEDs and the schematic of the blackbody radiation white color design with the chemical structure of the materials used for the devices. Color coordinates were calculated from the photoluminescence spectral characteristics of phosphorescent red, green, blue emitters. A 70 nm thick Al metal cathode and organic layers were successively deposited at a base pressure of $< 5 \times 10^{-7}$ Torr by thermal evaporation without breaking the vacuum. 15 wt% rubidium carbonate (Rb_2CO_3) doped bis-4,6-(3,5-di-3-pyridylphenyl)-2-methylpyrimidine (B3PYMPM) was used as a n-doped electron injection layer (EIL) and undoped B3PYMPM was used as an electron transport layer (ETL). EML (emitting layer) was consists of three layers: orange emitter, buffer layer, and blue emitter to take advantage of the exciplex forming character of the materials.⁸⁶⁻⁹¹ Ir(mphmq)₂(tmd) [Iridium(III) bis(4-methyl-2-(3,5-dimethylphenyl)quinolinato-N,C2') tetramethylheptadionate], Ir(ppy)₂(tmd) [iridium(III) bis(2-phenylquinoline) tetramethylheptadionate], and FIrpic [Iridium(III) bis((4,6-di-fluorophenyl)-pyridinato-N,C') picolinate] were used as the blue, green and red phosphorescence dyes, respectively. TCTA (4,4',4''-tris(N-carbazolyl)-triphenylamine), mCP (N,N'-dicarbazolyl-3,5-benzene), and B3PYMPM were used for HTM (hole transporting materials) for orange, HTM for blue, ETL(electron transporting materials) for orange and blue, respectively. The orange and blue EMLs are spatially separated by a buffer layer consisting B3PYMPM doped TCTA layer. Undoped TCTA, 1,1-bis-(4-bis(4-methyl-

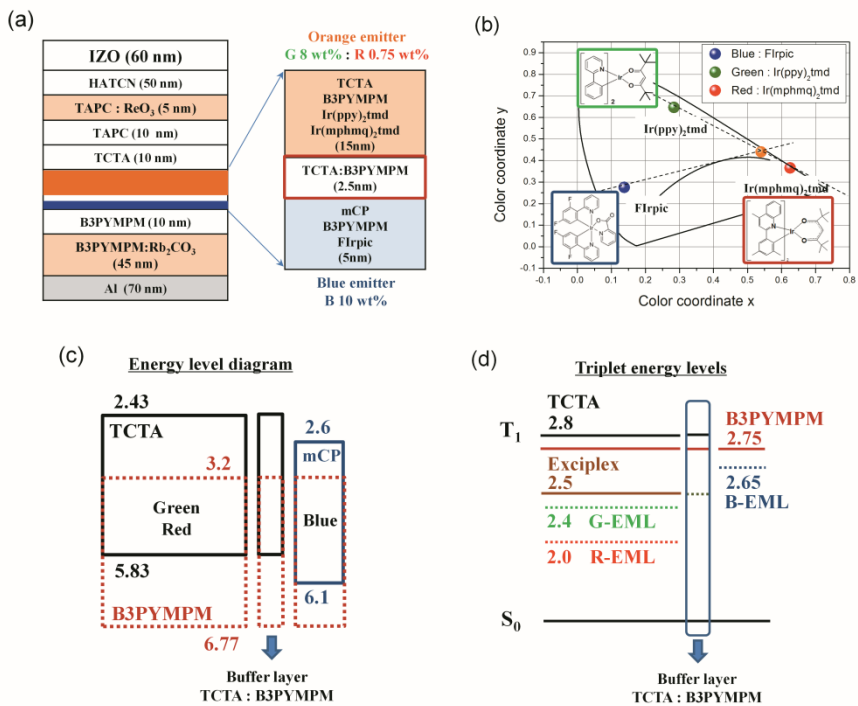


Figure 4.7 (a) Device structure and materials of white inverted top emitting OLEDs (b) TEOLEDs and the schematic of the blackbody radiation white color design. (c) is energy diagram of consisting materials of white emitter. (d) is triplet energy levels of consisting materials of white emitter.

phenyl)-amino-phenyl)-cyclohexane (TAPC) and TAPC doped with 8 wt% rhenium oxide (ReO_3) were used as a hole transport layers and a p-doped hole injection layer (HTLs, HIL), respectively. A 50 nm thick HATCN layer was deposited to protect the underlying organic layers from the plasma damage and have good hole-injection properties from the sputter deposited IZO top electrode.^{8,24,79,89-91} The device structure was optimized prior to the fabrication of the inverted TEOLEDs using the classical dipole model.⁴¹⁻⁴²

Orange and blue emitters are designed as the exciplex forming co-host system having a good electron-hole balance, low driving voltage, and low efficiency roll-off. Figure 4.7 c and d shows the energy level diagram and triplet energy level of the white emitter. Because the triplet energy levels of the exciplex and host materials were higher than dopants in EML, the energy transfer process from the exciplex to the dopants is more dominant than the direct charge trapping. The TCTA and B3PYMPM were used as the co-host of the orange EML in a molar ratio of 1:1. Firstly, the orange device was designed and fabricated. CIE color coordinate (x, y) of orange emitter for black body radiation white should be set in (0.54, 0.44). Doping concentration of red and green dye to 0.75 and 8 wt% were found from the photoluminescent (PL) spectra measured by 325 nm He-Cd laser. The mCP and B3PYMPM were used as the exciplex forming co-host for the blue EML in a molar ratio of 1:1. The doping concentration of the blue dye was 10 wt%. Buffer layer was set in the middle of orange and blue emitters consisting of TCTA doped with B3PYMPM. The buffer layer acts controlling the color balance from the separation of the charge carrier and avoiding energy transfer from the blue to the orange.

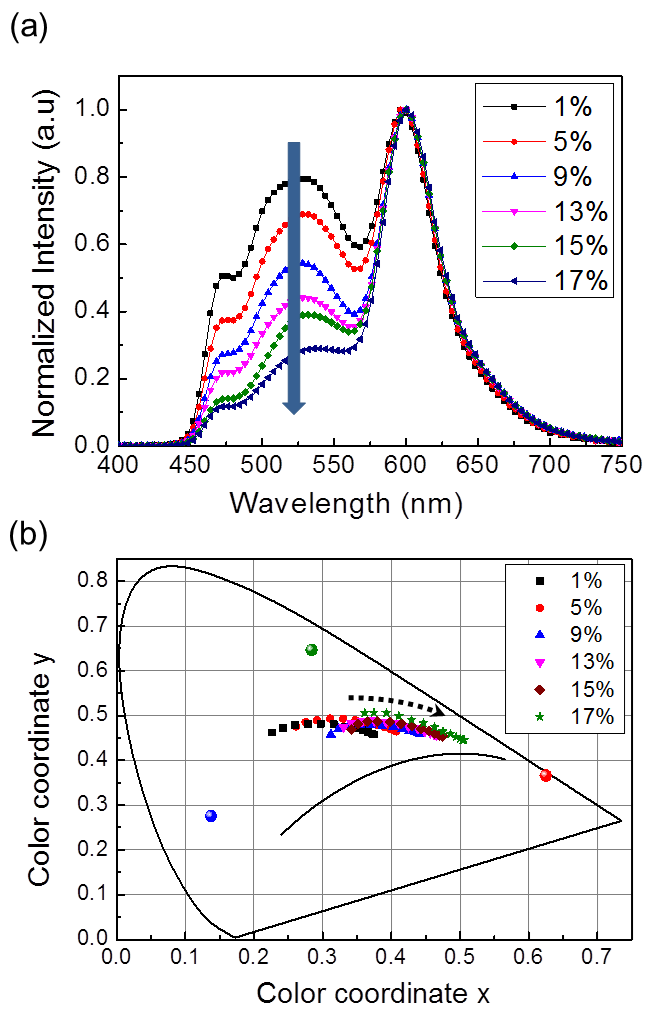


Figure 4.8 (a) Emission spectra in normal direction of white inverted TEOLEDs and (b) Angle dependency of the color coordinate in white inverted TEOLEDs, while doping concentration of B3PYMPM in buffer layer was controlled from 1~17wt%.

In order to design black body radiation white, doping concentration of B3PYMPM in buffer layer was controlled from 1~17wt%. (Figure 4.8) When increasing the doping concentration of B3PYMPM, blue emission was decreased as following increasing the orange emission so that the white color was approaching to the Planckian locus. TCTA doped with 17 for White 1 (W1) and 15wt% for White 2 (W2) of B3PYMPM as the buffer layers were chosen for design of the black body radiation white color device.

4.4 Results and Discussion

Two types of the IZO top electrode based inverted white TEOLEDs (W1 and W2) with the broadband AR layer were fabricated. LiF was chosen as the low index capping material whose refractive index is 1.39 at 550 nm which is close to the ideal case for the single layer anti-reflection at the interface between IZO and air. When the AR layer is designed for a wavelength in the middle of the visible band with the phase matching condition, reasonably good anti-reflection property over the entire band can be expected. The LiF layer was deposited 100 nm thick of $\lambda/4$ phase matching condition for visible band. As shown in Figure 4.9a and b, because the single junction white OLEDs have only one cavity length for RGB emitters, in case of the optimized device structure for maximum EQEs, the angle dependent spectral change occurs. However, the devices with the broadband AR layer on the TCO top electrode shows extremely small spectral change with the variation of $\Delta x=0.02$, $\Delta y=0.01$ in the CIE 1931 coordinates as the viewing angle changes from 0 to 60°. (Figure 4.9c and d) Figure 4.9e illustrates the SIE 1931

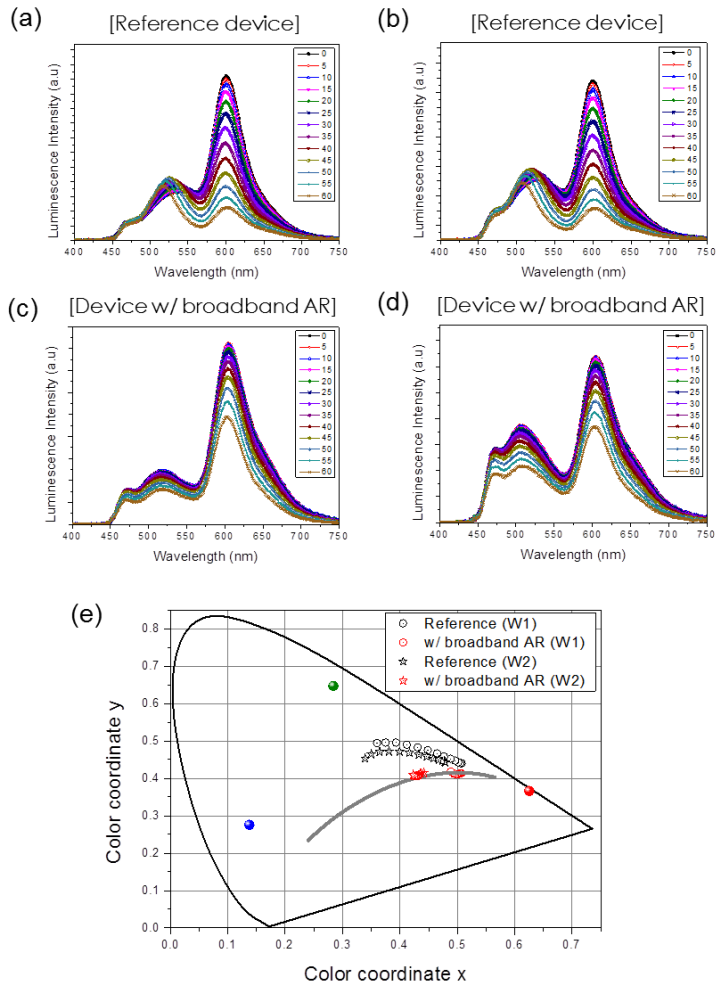


Figure 4.9 Angle dependent emission spectra of white inverted TEOLEDs (a) and (b) are reference devices of W1 and W2. (c) and (d) are devices with broadband AR layer of W1 and W2, respectively. (e) Angle dependent color coordinate of the devices from 0 to 60 degrees.

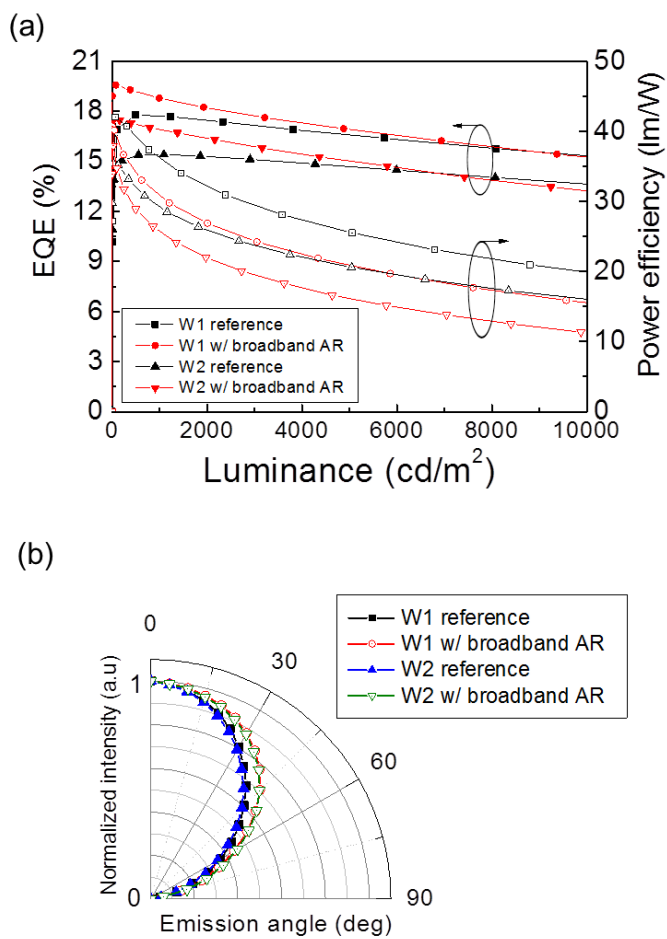


Figure 4.10 (a) external quantum efficiencies and power efficiencies of the white inverted TEOLEDs (b) normalized electroluminescent intensities at different viewing angles of reference devices and devices with broadband AR layer.

color coordinates calculated from the spectral properties of W1 and W2 with and without the broadband AR layer. As results, W1 and W2 shows ~2200K and ~3000K of correlated color temperature in 5 steps of MacAdam ellipse with the color stability on viewing angles.

Moreover, the devices with broadband AR show higher EQEs and wider angle dependent intensity distribution than reference devices. As shown in Figure 4.10a, W1 and W2 with the broadband AR shows the EQEs of 18.8% and 16.9% increase from the EQEs of 17.7% and 15.4% for the reference devices, respectively. These values are the highest values of EQEs ever achieved for the single junction TEOLEDs. Angle dependent intensity distributions were widening due to the relaxation of cavity effect from the broadband AR, which is also good property for the applications in OLEDs. (Figure 4.10b)

The electroluminescence spectra in the normal direction of the W1 and W2 devices applied with the broadband AR layers are well matched with the simulation results as shown in Figure 4.11, respectively. We carried out the optical simulation for the analysis of the spectral characteristics and generated photon ratio of each color of the devices. Because the variation of spectral property on viewing angles is very small, we could calculate the ratio of generated photon numbers of blue, green, red from the electroluminescence spectra. Experimentally measured values of PLQYs (q_{PL}) and horizontal dipole orientation ratio (Θ) of the emitters were considered for the calculation. Ir(mphmq)₂tmd, Ir(ppy)₂tmd, and FIrpic were used for red, green and blue emitters whose PL QYs and horizontal orientation ratio are $q_{PL} = 0.96$, $\Theta = 0.96$ for red and $q_{PL} = 0.96$, $\Theta = 0.78$ for green and $q_{PL} = 1$, $\Theta = 0.76$ for blue.⁹² As results, we obtained the ratio of distributed photon number of (B)15 : (G)14 : (R)71 for W1 and (B)25 : (G)16 : (R)59 for W2. Performances

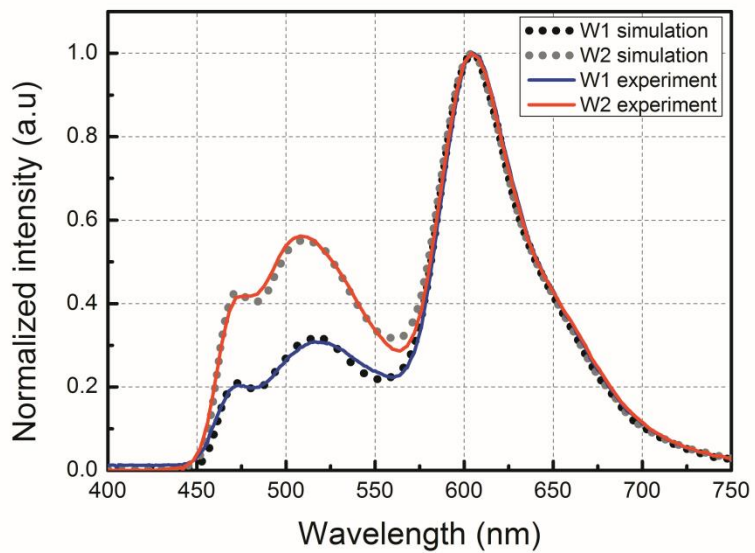


Figure 4.11 (a) external quantum efficiencies and power efficiencies of the white inverted TEOLEDs (b) normalized electroluminescent intensities at different viewing angles of reference devices and devices with broadband AR layer.

of the devices are summarized in Table 4.1.

4.5 Conclusion

In conclusion, we demonstrated a highly efficient the single junction white TEOLEDs with the high color quality by using the broadband AR layer on the top of the devices. Applying 100 nm thick LiF on the top of the OLEDs was satisfied with the ideal values of refractive index ($n \sim 1.4$) and the thickness of the $\lambda/4$ phase matching for single layer broadband anti-reflection at the interface between IZO electrode and air. We have experimentally realized the single junction white TEOLEDs with the EQEs of 18.8% and 16.9% satisfied with the blackbody radiation white of 2200K and 3000K, respectively. Moreover, both of white TEOLEDs have small angle dependent spectral change about the requirement of 5 steps of MacAdam ellipse (duv values of -0.0014~0.0009 and 0.0041~0.0058 at 0~60 degrees). A simple process which combined the high efficiency and no color shift suggests the great potential of our device for application in OLEDs.

Table 4.1 Performances of white inverted TEOLEDs

Doping ratio of B3PYMPM in Buffer layer	Color Coordinate		Delta uv		Correlated Color Temperature		Color Rendering Index		EQE (%)	
	Normal direction	Deviation 0~60°	Normal direction	Deviation 0~60°	Normal direction	Deviation 0~60°	Normal direction	Deviation 0~60°	1,000 cd/m ²	3,000 cd/m ²
W1 17 wt%	Reference	Δx 0.15 (0.36~0.51), Δy 0.05 (0.44~0.49)	0.0073	0.0073~ 0.052	2.342 K	2,633 K (2,342~ 4,975 K)	71.6	7.0 67.7~74.7	17.7	17.2
	w/ Broadband AR	Δx 0.02 (0.49~0.51), Δy 0.01 (0.41~0.42)	-0.0007	-0.0014~ 0.0009	2.185 K	216 K (2,178~ 2,394 K)	76.8	1.3 75.7~77.0	18.8	17.7
W2 15 wt%	Reference	Δx 0.14 (0.34~0.48), Δy 0.03 (0.44~0.47)	0.0098	0.0098~ 0.042	2.699 K	2,652 K (2,699~ 5,351 K)	76.2	2.5 68.1~77.5	15.4	15.1
	w/ Broadband AR	Δx 0.02 (0.42~0.44), Δy 0.01 (0.41~0.42)	0.0042	0.0041~ 0.0058	3.031 K	241 K (3,031~ 3,272 K)	75.8	1.9 73.9~75.8	16.9	15.9

Chapter 5 Highly enhanced light extraction from inverted top emitting OLEDs with little image blurring and good color stability

5.1 Introduction

Top emission organic light emitting diodes (TEOLEDs) using a reflective metal bottom electrode are in use for small size displays to increase the aperture ratio of emitting area. Semitransparent thin metal is generally used as the top electrode in TEOLEDs, resulting in narrow emission spectrum and large variation of emission color with viewing angle due to the strong microcavity effect. Two metal electrodes also induce large optical loss from surface plasmon polaritons (SPPs).^{16,28} Light extraction layers are not currently being used in the devices because of the pixel blurring. Therefore it is rather critical to search for a method to enhance the light extraction efficiency with less pixel blurring and color variation on viewing angle and with low SPP loss. Light extraction methods reported up to now in TEOLEDs are using a capping layer^{29,66}, micro lens arrays (MLAs)^{35,36} and a diffuser¹⁰⁵ on the top metal electrode and corrugated structures.^{106,107} The methods showed improved efficiencies and color stabilities on viewing angles. With the two metal electrodes, the light extraction efficiency is limited to under 1.3 times in the TEOLEDs due to the large SPP loss reaching almost 30~40% of the total emitted light. Integration of a micro lens array (MLA) on transparent top electrodes [MoO₃/Au/MoO₃ (40 nm/10 nm/5 nm)] enhanced both external quantum efficiency and color stability at the same time by using

large-area device.¹⁰⁸ However, better transparency and refractive index matching between the transparent electrode and the MLA will further boost the performance of the TEOLEDs. Recent report on the integration of a capping layer on a thin wetting layer [MoO₃/Au/Ag (1 nm/2 nm/7 nm)] significantly improved the color stability but with limited enhancement (1.2 times) of light extraction.⁸² Few researches reported a large enhancement of light extraction from TEOLEDs with little pixel blurring and color variation on viewing angles with low SPP loss.

In this paper we report a 1.8 times enhancement of light extraction from a high efficiency TEOLEDs with external quantum efficiency (EQE) of 44.7%, little image blurring and little spectral change on viewing angles by using a transparent indium zinc oxide top electrode and in-situ fabricated MLAs with a high refractive index material comparable with a top electrode.

5.2 Experiment

Figure 5.1a shows the device structure of TEOLEDs and the chemical structure of the materials used for the devices. Basic ideas of the structure are as follows. Firstly, we adopted a top emission OLED integrated with MLA to reduce the image blurring because of the short distance from the emission zone to air (~ a few hundred nanometers) as explained in Figure 5.1b. Secondly, we used a transparent conducting oxide (TCO) as the top electrode instead of thin metals or other dielectric/metal/dielectric electrodes.^{61,109} TCO top electrodes allow us not only to reduce the SPP and absorption losses, but also maximize the light extraction of emitted light by integrating high refractive index MLA on the TCO electrode because organic layers and TCOs

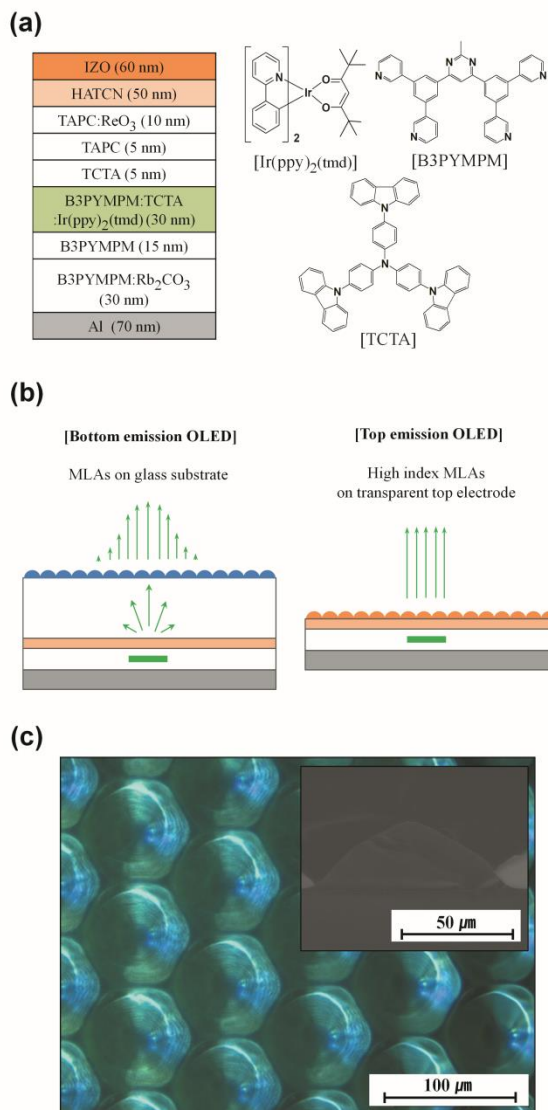


Figure 5.1 Inverted TEOLED & Microstructures. (a) Device structure of the inverted TEOLED and molecular structures of organic materials in the emitting layer. (b) Schematic diagrams of the bottom and top emission OLED with MLAs. (c) Optical microscope image and SEM cross section of the organic MLAs.

have similar refractive indices.⁷⁸ The similar refractive indices between top electrode and organic MLAs relaxed the spectral change influenced by the reflectance of the interface of them, resulting the emission spectra on viewing angles turned to the intrinsic photoluminescence (PL) spectrum of the emitter: Ir(ppy)₂tmd [bis(2-phenylpyridine)iridium(III)(2,2,6,6-tetramethylheptane-3,5-diketonate)]. Thirdly we selected an inverted OLED structure because TCO electrode can be easily fabricated using the structure without sputter damage.^{75,76,111}

The device structure and its fabrication procedure are basically the same as the chapter 3.2 except the light extraction pattern directly integrated on the top of the inverted TEOLED whose image is shown in Figure 5.1c. The micro lens structures were fabricated using thermal evaporation of 4,4-bis[N-(1-naphthyl)-N-phenyl-amino]biphenyl (α -NPD) on the IZO top electrode by gradually lowering the deposition rates through a shadow mask and had an almost 100% fill factor. The radius of the micro lens was 30 μm . α -NPD has a high refractive index of ~ 1.8 close to IZO (~ 2.0). The fabrication procedure of the MLA was described in our previous report.³⁴

5.3 Results and Discussion

Figure 5.2a and b show the current density-voltage-luminance (J-V-L) characteristics and emission spectra in the normal direction of the inverted TEOLEDs with and without the light extraction layer including the PL spectrum of Ir(ppy)₂tmd. Optical simulation for the angle dependent electroluminescence spectra of the devices was carried out using the classical dipole model. Simulated results are well matched with the experimental

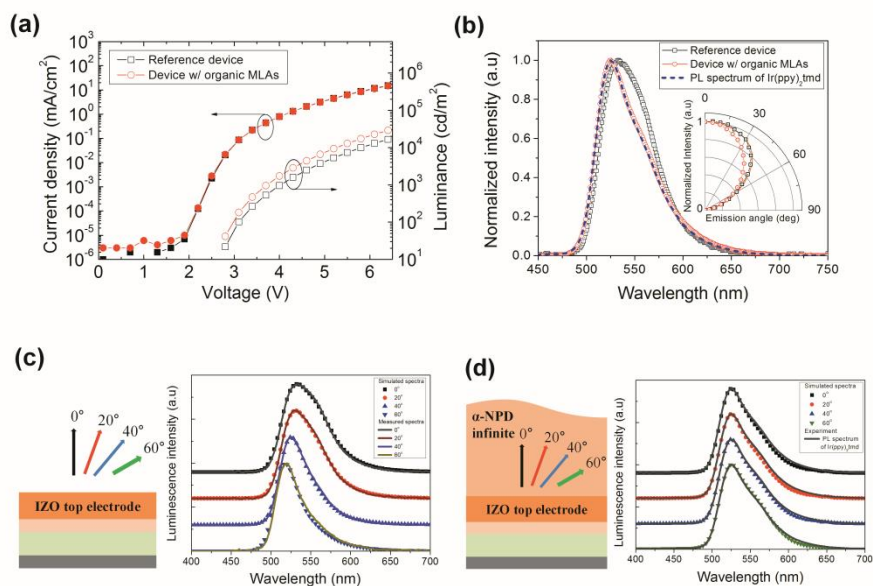


Figure 5.2 Characteristics of the inverted TEOLEDs with and without organic MLAs. (a) Voltage dependent current density and corresponding luminance. (b) Normalized intensity spectra in normal direction with and without organic MLAs and the intrinsic PL spectrum of the Ir(ppy)₂tmd including the angle dependent intensity distribution of the devices in inset. (c) Calculated and measured spectra of the reference devices. (d) Calculated spectra from the TEOLED with α -NPD semi-infinite surroundings on the top of the device compared to the PL spectrum of the Ir(ppy)₂tmd.

results as shown in Figure 5.2c. As an additional analysis of the spectral characteristics of the devices, the refractive index of an α -NPD semi-infinite surroundings on the top of the IZO based TEOLEDs was set as an assumption, where the propagation of the light into the directly attached α -NPD micro structures. As results, all the directions of the emitted light showed almost same spectral shapes and turned to the intrinsic PL spectrum of the emitting materials (In Figure 5.2d). The devices showed the turn-on voltage of 2.8 V at 22 cd/m². The efficiencies of the devices are shown in Figure 5.3. The reference device without the micro lens array showed a maximum current efficiency of 120.7 cd/A (Figure 5.3a), a maximum external quantum efficiency (EQE) of 27.6% and the power efficiency of 85.9 lm/W (Figure 5.3b) at 1,000 cd/m², respectively, where the EQE and power efficiencies were calibrated by considering the spectrum and intensity variations with the viewing angle. Moreover the efficiency roll-off was small up to 20,000 cd/m² with EQE's and current efficiencies of 26.0% and 113.7 cd/A at 10,000 cd/m² and 24.5% and 107.6 cd/A at 20,000 cd/m², respectively. Integration of the organic microstructures on the top electrode increased the current efficiency by 1.8 times reaching the maximum value of 217.2 cd/A. Similarly, EQE and power efficiencies were improved to 44.7% and 134.7 lm/W at 1,000 cd/m² by using the light extraction layer corresponding to 1.62 and 1.59 times enhancement, respectively. The performances of the devices are summarized in Table 5.1. The efficiencies with the light extraction layer are the highest values among phosphorescent green top emission OLEDs reported up to now.

The device with the light extraction pattern on the TEOLED showed little change in spectrum with viewing angle because electroluminescence (EL) spectra in all directions turned to the intrinsic PL spectrum of the emitting

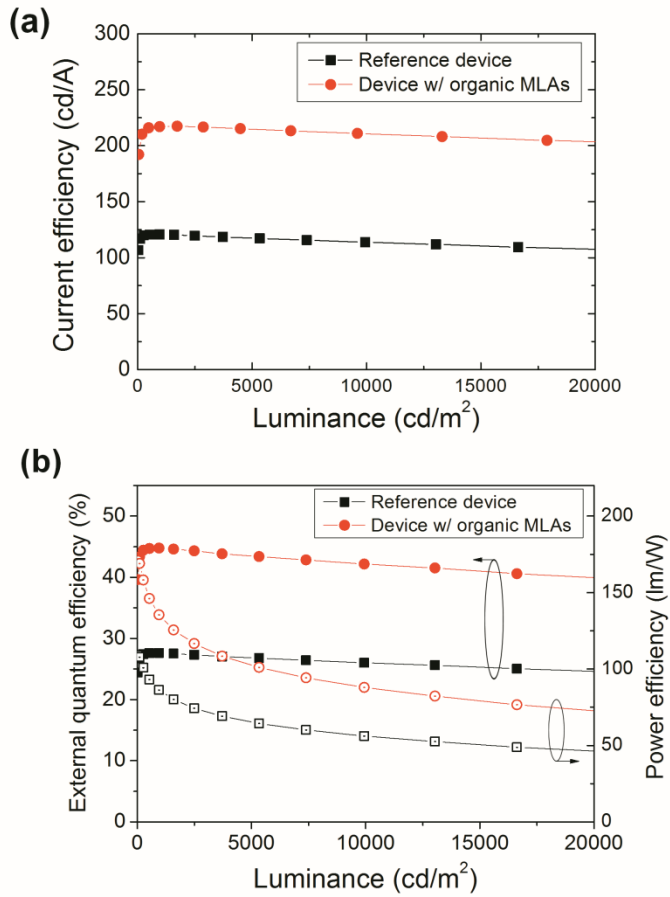


Figure 5.3 Device performance of the inverted TEOLEDs with and without organic MLAs. (a) Current efficiencies, and (b) external quantum efficiency and power efficiency of the devices with (red circle) and without (black rectangle) organic MLAs.

Table 5.1 Performances of inverted TEOLEDs

	C.E (cd/A)	EQE (%)	P.E (lm/W)
	1,000 cd/m ²	1,000 cd/m ²	1,000 cd/m ²
	10,000 cd/m ²	10,000 cd/m ²	10,000 cd/m ²
Reference device	120.7	27.6	85.9
Device w/MLAs	217.2	44.7	134.7
Enhancement ratio	1.80	1.62	1.57

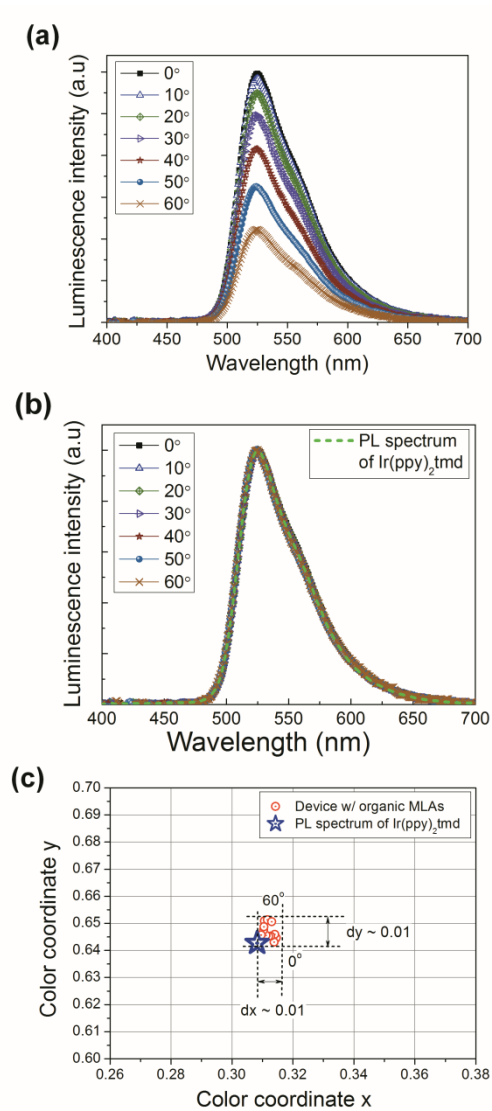


Figure 5.4 Angular emission property of the inverted TEOLEDs with organic MLAs compared to the intrinsic PL spectrum of Ir(ppy)₂tmd. (a) Angle dependent emission spectra and (b) normalized spectra of the device with organic MLAs and PL spectrum of the Ir(ppy)₂tmd. (c) CIE 1931 color coordinates of the devices with organic MLAs and PL spectrum of the Ir(ppy)₂tmd.

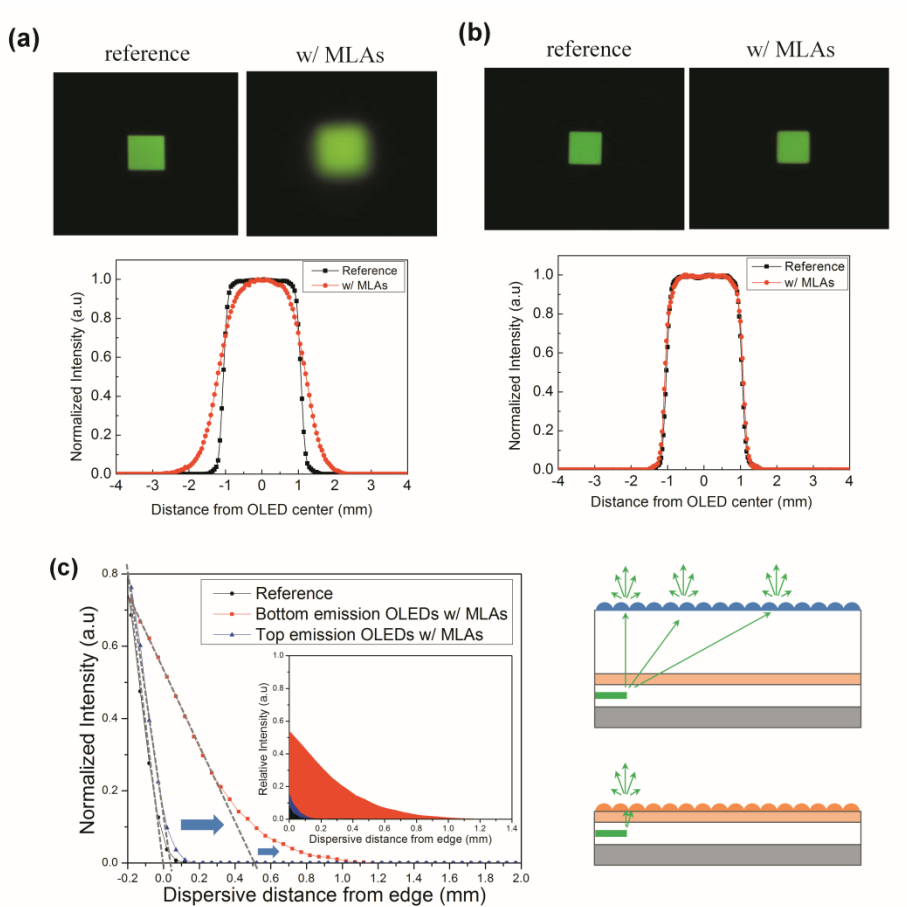


Figure 5.5 Comparison for the image blur of the bottom and top emission OLEDs. Photo images and intensity profile against the distance from OLED center of (a) the bottom emission OLED with and without MLAs on the glass substrate and (b) the top emission OLED with and without organic MLAs on top of the TCO electrode at same luminance of 500 cd/m^2 . The cell size of the images was $2 \text{ mm} \times 2 \text{ mm}$.

material of Ir(ppy)₂tmd (Figure 5.4a and b). The stability of the emission color on viewing angles is apparent in Figure 5.4c, where changes in emission spectrum on viewing angles are displayed in the CIE coordinate. The device with the micro lens arrays showed $\Delta x = 0.01$ and $\Delta y = 0.01$ as the viewing angle varies from 0 and 60°.

It is known that integration of micro lens array on a bottom emission OLED gives image blurring, which is the reason that the micro lens array has not been adopted in displays. It is not the case for our top emission OLEDs as manifested in Figure 5.5a and b. Figure 5.5 c shows the tails of the dispersive intensity profile at the edge of the devices. Bottom emission OLEDs shows over 1 mm of dispersive emission tails at the edge of the device mainly caused by the thickness of the glass substrate (0.7 mm). The planar device has 0.5 mm dispersed tails which might come from the diffracted light at the edge influenced by the exposure time or the sensitivity of ISO. The difference of the distance between the planar device and the TEOLEDs with organic MLAs was ~50 μm attributed by the size of micro lens arrays. It is expected because the micro lens array is directly integrated on the top electrode without space. The distance between the emission zone and the lens array³⁴ is less than 200 nm and pixel size in high resolution displays is about 20 μm for 400 ppi (pixel per inch) device. Because of the high aspect ratio, the image blurring can be minimized in top emission OLEDs.

5.4 Optical simulation for light extraction

In chapter 2, we carried out the optical simulation for light extraction in

Table 5.2 Comparison of the measured and simulated enhancement ratio and external quantum efficiencies for the inverted TEOLEDs.

EQE (%) @ 1,000 nit	EIL 30 nm		EIL 50 nm		EIL 70 nm				
	bare	w/ MLAs Enhanceme nt ratio	bare	w/ MLAs Enhanceme nt ratio	bare	w/ MLAs Enhanceme nt ratio			
Experimental value	27.6	44.7	1.62	20.0	36.1	1.80	5.0	13.7	2.76
Calculated value		42.8	1.55		34.8	1.74		12.2	2.43

Table 5.2 Comparison of the measured and simulated enhancement ratio and external quantum efficiencies for the inverted TEOLEDs.

TEOLEDs applied with MLAs. As a simulation result, when giving the point about 1.8 of refractive index of MLAs matched with the refractive index of α -NPD at 550 nm, we achieved 1.55, 1.74, and 2.43 times of enhancement ratio, corresponding to 42.8, 34.8, and 12.2% of the EQEs for the device with 30, 50 and 70 nm thick EILs, respectively. For comparison, experimental results of EQEs were 44.7, 36.1, and 13.7% of EQE at 1,000 cd/m² for the device with 30, 50 and 70 nm thick EILs, respectively, which are shown in good agreement with simulated and experimental results. All the results are summarized in Table 5.2.

5.5 Conclusion

In conclusion, we successfully fabricated a highly efficient phosphorescent green inverted TEOLED by using the directly fabricated organic microstructures. The high refractive index light extraction structure on the top of the TCO electrode of the inverted TEOLED, gave a very high current efficiency of 217.2 cd/A in the normal direction enhanced from 120.7 cd/A, the EQE of 44.7% enhanced from 27.6%, the power efficiency of 134.7 lm/W enhanced from 85.9 lm/W, respectively. In addition, the OLED with the high refractive index light extraction layer showed great color stability with the color variation of $\Delta x = 0.01$ and $\Delta y = 0.01$ in CIE color coordinate as the viewing angle varies between 0° and 60°. The results demonstrate that our light extraction method has a large potential for high efficiency top emitting

OLEDs to become future display and lighting application.

Chapter 6 Highly enhanced light extraction from surface plasmonic loss minimized OLEDs

6.1 Introduction

Light extraction of organic light emitting diodes (OLEDs) has been an important issue in order to increase the external quantum efficiency (EQE) of the devices for displays and solid-state lighting, because 70%~80% of the emitted light is confined in the substrate (substrate mode), in the organic layer and in the transparent electrode (waveguide mode), or lost by absorption and surface plasmon polaritons of the metal electrode (absorption and SP mode).^{16,17,95} Various methods have been proposed to extract the substrate mode and/or the waveguide modes, which include the use of a micro lens array (MLA) on the glass substrate,^{34,96,97} the insertion of a photonic crystal structure, diffusive particles, silica aero gel, and the use of a low refractive index grid between the transparent conducting electrode and the glass substrate.⁹⁸⁻¹⁰⁴ The use of a patterned high refractive index substrate¹⁰⁹, a fully buckled device system¹¹³⁻¹¹⁵ or using a plastic substrate with a multifunctional anode stacks¹¹⁶ has also been suggested for effective light extraction methods. However, the absorption and SP losses by the metal electrode(s) in bottom

and top emission OLEDs cannot be avoided, therefore we need to minimize them in OLEDs to increase the EQE.

Several approaches have been suggested to reduce the surface plasmon loss, such as by controlling the molecular orientation of the emitter, increasing the distance between the emitting layer and the metal electrode to reduce the interaction between the metal surface and the emitting dipoles, or fabricating a metal electrode free OLED; these methods have met with limited success.^{73,89,117} A metal free OLED with good transparency combined with a method to extract the light efficiently from the device could be a solution for the purpose of reducing the surface plasmon loss.

Here we report a metal-free OLED with an extremely high EQE, achieved by reducing the SP and intrinsic absorption loss, where the transparent indium zinc oxide (IZO) and indium tin oxide (ITO) layers were used as the top and bottom electrodes, respectively. To extract the confined light inside the device, a high refractive index light extraction pattern was additionally fabricated on the transparent top electrode using a simple evaporation method and a MLA sheet was attached on the bottom side of the glass substrate, as shown in Fig. 1a. As a result, the EQE of the device increased from 18.2% to 47.3% by using both microstructures, and this was additionally enhanced to 62.9% by attaching an index-matched hemisphere lens instead of the MLA on the glass substrate to extract the remaining light guiding losses inside of the device.

6.2 Experiments

Figure 6.1a shows the schematic diagrams of the structure of the transparent OLED and the top and bottom microstructures used for the light extraction. The transparent OLED has an inverted structure. 8 wt% Ir(ppy)₃ [fac-tris(2-phenylpyridine) iridium] doped CBP [4,4'-N,N'-dicarbazole-biphenyl] was used as the emitting layer (EML), with ITO as the bottom electrode and IZO as the top electrode. The HATCN (1,4,5,8,9,11-hexaazatriphenylenehexacarbonitrile) was used as the hole injection layer as well as the protective layer for the sputter deposited IZO. The electron microscope images of the micro-cone array (MCA) and the MLA used as the bottom and top extraction layers are shown in Fig. 6.1b and c, respectively. The MCA was fabricated using the thermal evaporation of 4,4-bis[N-(1-naphthyl)-N-phenyl-amino]biphenyl(α -NPD) on IZO and has an almost 100% fill factor (Fig. 6.1d) using a shadow mask after fabrication of the top IZO electrode. Various structures can be fabricated by controlling the deposition rate (Fig. 6.2). We selected the MCA for this work among various structures because of the simplicity of the in-situ fabrication of the structure by thermal evaporation. α -NPD has a high refractive index of ~ 1.8 close to IZO whose refractive index is about ~ 2.0 . The diameter and the height of the micro-cones are 60 μm and 80 μm , respectively. The MLA sheet used for the bottom extraction layer is composed of the half sphere micro-lenses with a diameter

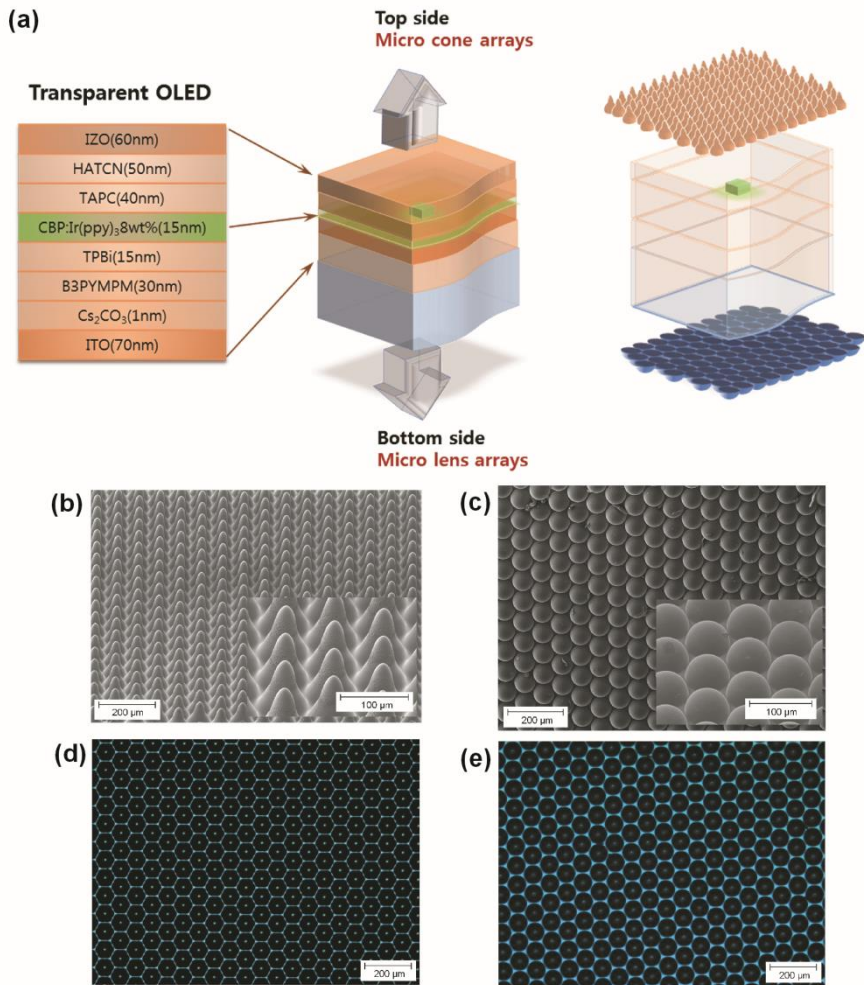


Figure 6.1. Transparent OLED & Microstructures. (a) Schematic diagrams of the structure of the transparent OLED and the microstructures for light extraction. (b) SEM images of the top side micro cone array. (c) SEM images of the bottom side micro lens array. (d) Optical microscope image of the top side micro cone array. (e) Optical microscope image of the bottom side micro lens array. of 70 μm and a fill factor of 90% (Fig. 6.1e). The refractive index of the MLA sheet is the same as that of the glass substrate.

6.2.1 Transparent device fabrication and measurement

The transparent OLEDs have the structure of ITO (70 nm)/cesium carbonate (Cs_2CO_3) (1nm)/ bis-4,6-(3,5-di-3-pyridylphenyl)-2-methylpyrimidine (B3PYMPM) (30 nm)/ 2,2',2''-(1,3,5-benzenetriyl)tris-[1-phenyl-1H-benzimidazole] (TPBi) (15 nm)/8 wt% fac-tris(2-phenylpyridine) iridium [Ir(ppy)₃] doped 4,4'-N,N'-dicarbazole-biphenyl (CBP) (15 nm)/1,1'-bis-(4-bis(4-methyl-phenyl)-amino-phenyl)-cyclohexane (TAPC) (40 nm)/1,4,5,8,9,11-hexaazatriphenylenehexacarbonitrile (HATCN) (50 nm)/IZO (60 nm). The organic layers were successively deposited at a base pressure of $< 5 \times 10^{-7}$ Torr on pre-cleaned 70 nm thick indium tin oxide (ITO) patterned glass substrates, and then the substrates were transferred to another chamber through a load-lock chamber to form the IZO anode on top of the HAT-CN layer. The IZO top electrode was fabricated by a sputtering process under a gas flow rate of 30 sccm for Ar and 0.6 sccm for O₂ and a working pressure of 1 mTorr.

We measured the voltage dependent current density and the corresponding luminance, and EL spectra of the reference transparent device using a Keithley 2400 programmable source meter and a Spectra Scan PR650 (Photo Research). The angle dependent emission intensity was measured using an area independent silicon photo diode (Ocean Optics) and the EQE data of the reference transparent device was calibrated using the angle dependent

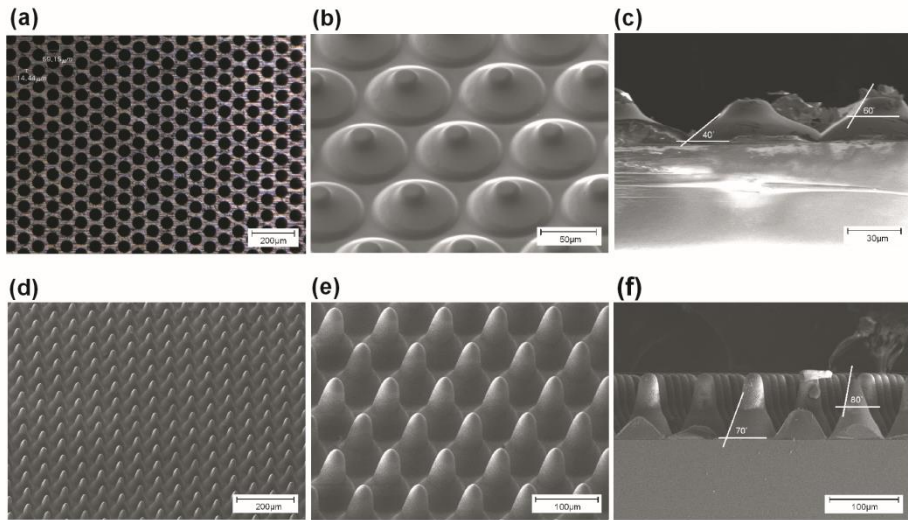


Figure 6.2 Fabrication of high refractive index microstructures. (a) Optical microscope image of shadow mask used for the fabrication of micro cone structures. (b) SEM image of the structure fabricated using two step deposition rate of ~ 5 nm/s for ~ 30 min followed by ~ 15 nm/s for ~ 10 min. (c) Cross section image of the structure grown by two step deposition rate with the taper angle of $\sim 40^\circ$ at the deposition rate of ~ 5 nm/s and the taper angle of $\sim 60^\circ$ at the deposition rate of ~ 15 nm/s. (d), (e). SEM images of the structure fabricated using two step deposition rate of ~ 20 nm/s for ~ 30 min followed by ~ 25 nm/s for ~ 30 min. (f), Cross section image of the structure grown by two step deposition rate with the taper angle of $\sim 70^\circ$ at the deposition rate of ~ 20 nm/s and the taper angle of $\sim 80^\circ$ at the deposition rate of ~ 25 nm/s.

emission intensity^{118,119}. After fabricating the microstructures and/or hemisphere lens, we measured the radiant flux of each sample by using a six-inch integrating sphere made by Labsphere.

6.2.2 Microstructure fabrication

The microstructures on the top IZO electrode were fabricated by evaporating 4,4-bis[N-(1-naphthyl)-N-phenyl-amino]biphenyl(α -NPD) using a simple vacuum evaporating system through a 30 μm thick metal shadow mask where the circular hole arrays, with 60 μm diameters, were hexagonally arranged. Densely packed micro-cone arrays with an almost 100% fill factor were obtained with a height of ~ 80 μm and taper angles of $60\sim 70^\circ$ when α -NPD was deposited at the deposition rate of 15~20 nm/s. α -NPD was selected for the refractive index matching with the IZO top electrode. The refractive index of α -NPD is ~ 1.80 at 550 nm, which is close to that of IZO (~ 2.0). In the case of the bottom side, a film type micro lens array made of index matching optical adhesive NOA65 (Norland optical adhesive, $n=1.52$) was used to achieve the index matching condition. The micro lenses in the film have the shape of half spheres, each with a radius of 35 μm , and 90% fill factor hexagonal arrays. Additionally, we used a BK7 half-sphere lens with a 10 mm diameter (Edmond optics) and used the refractive index matching adhesive when attaching microstructures on the glass substrate.

6.3 Results and Discussion

The EQE of the device without the microstructures is shown in Fig. 6.3a. The efficiency data were obtained from the current density–voltage–luminance characteristics of the device shown in Fig. 6.4. The device shows a maximum EQE of 18.2% (13.0% from the bottom side and 5.2% from the top side). Integration of the microstructures on the transparent OLEDs increased the total EQE enormously, as shown in Fig 6.3b. A maximum EQE value of 47.3% (bottom 31.8% and top 15.5%) was obtained, which is 2.6 times higher than the device without the microstructures. When we replace the MLA on the glass substrate by an index matched hemispherical lens, the EQE value increased to an even much higher value of 62.9% (Fig. 6.3c), which is 3.46 times the increment ratio. The enhancement ratios of the EQE values are almost the same even at high luminance, increasing from 15.1% and 11.7 % at 1 and 10 mA/cm² in the reference device to 39.2% and 30.5% in the device with the microstructures and 52.3% and 39.7% in the device with the hemispherical lens on the glass side, respectively.

The angular dependences of the light intensity are shown in Fig. 6.3d and e for the bottom and top emissions, respectively. The reference transparent device shows emission patterns close to the Lambertian for the bottom and top emission. Interestingly, the device with the microstructures displays a stronger side emission than the device without the microstructures. As a result, the bottom and top emissions give 1.33 and 1.14 times a larger total emission than the Lambertian emission when normalized to the vertical emission. Moreover,

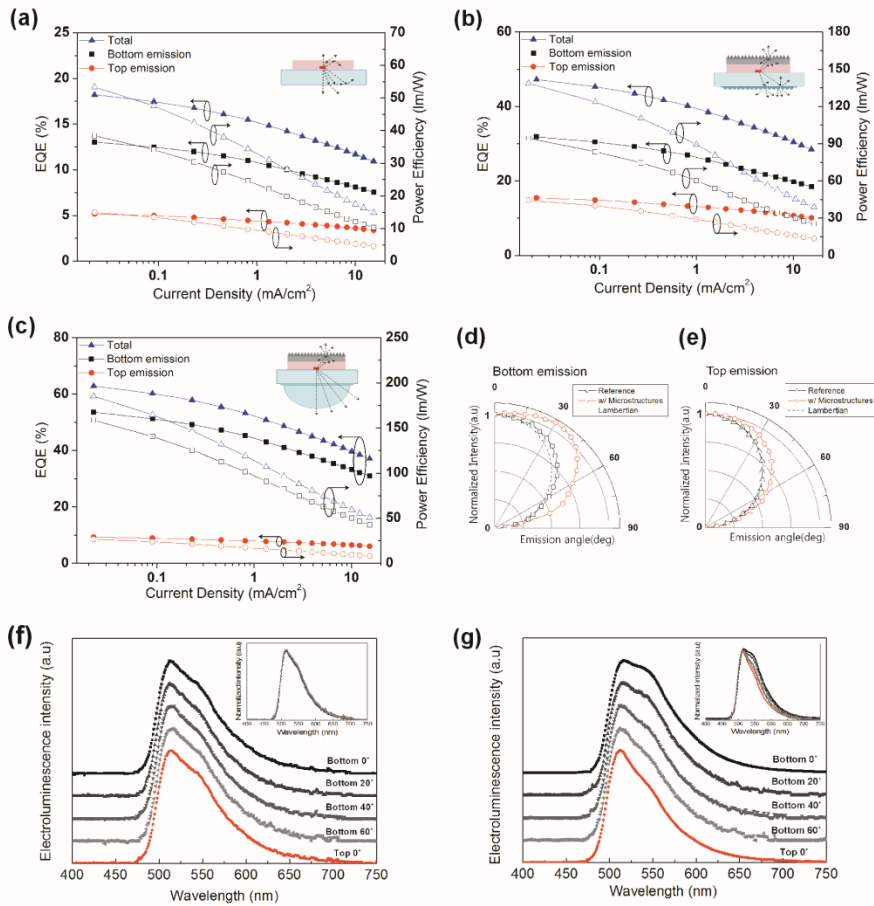


Figure 6.3 External quantum efficiencies and power efficiencies, angle dependent emission intensities and spectra of the OLEDs. (a)-(c) External quantum efficiencies (filled symbols) and power efficiencies (open symbols) as a function of current density for the total emission (triangle), bottom emission (rectangle) and top emission (circle) from the reference transparent OLED without any light extraction layers: in (a) with the micro-cone array on the top side and the micro-lens array at the bottom side; in (b), with the micro-cone array on the top and a half sphere lens on the bottom side; and in (c), schematic diagrams of the structure of the OLEDs are displayed as the inset of (a)-(c). (d)-(e), Normalized angle dependent emission intensities from the (d) bottom and (e) top sides of the OLED with the microstructures on both sides (circle) are compared with the reference OLED (rectangle). Lambertian emission patterns are displayed as dashed lines. (f)-(g), Angle dependent emission spectra from the OLEDs (f) with the microstructures and (g) without the microstructures.

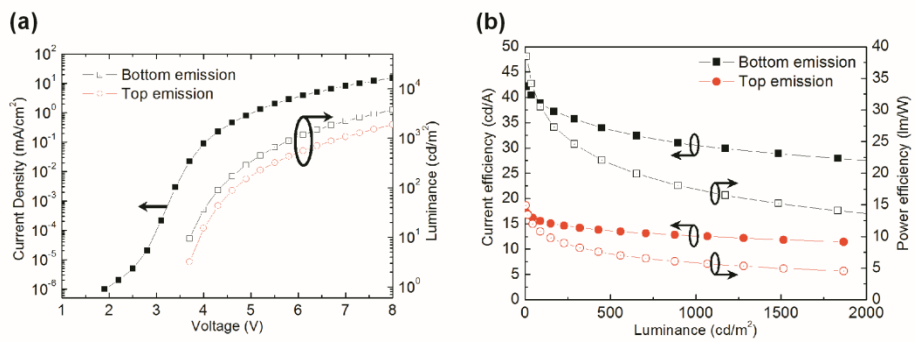


Figure 6.4 Characteristics of the reference transparent OLED. (a) Voltage dependent current density and corresponding luminance. (b) Current and power efficiencies as a function of luminance

integration of the microstructures to the OLED leads to a unified emission spectrum independent of the viewing angle (Fig. 6.3f), in contrast to the reference OLED which shows a significant variation of the emission spectra (Fig. 6.3g).

The advantage of the transparent OLED for the reduction of the SP and absorption loss is demonstrated in Fig. 6.5a-c, which displays the results of the coupled mode analysis using the classical dipole model.^{41,42} Cases of three different devices are used for the analysis as a function of the thickness of the electron transporting layer (ETL): (a) a top emission OLED with a 100 nm thick Al layer and a 20 nm thick Ag layer as the bottom and top electrodes, respectively; (b) a bottom emission OLED with a 100 nm thick Al layer and a 60 nm IZO layer as the top and bottom electrodes, respectively; and (c) a transparent OLED with an ITO (70 nm) layer and an IZO (60 nm) layer as the bottom and top electrodes, respectively. The same organic layers shown in Fig. 3a-c were used in the three devices, and the thickness of the hole transporting layer was optimized to get the maximum EQE values in each device (Fig. S3). A PL quantum yield (q) of 1 and an isotropic orientation¹²⁰ of the emitting dyes were assumed in the simulation. The top emission OLED (a) with the metal/metal electrodes showed a large SP result and an absorption loss of about 52%. This value can be reduced at the expense of a low EQE if the thickness of the ETL increases. OLED (b), with the metal/transparent conducting oxide (TCO) electrodes, exhibited a reduced SP and absorption losses with increasing ETL thickness. Nevertheless, the SP and absorption loss result was over 25% which is much higher than the result of 7% of the transparent OLEDs (c) with the TCO/TCO electrodes. The much smaller SP loss in the transparent OLEDs originates from the much lower free electron

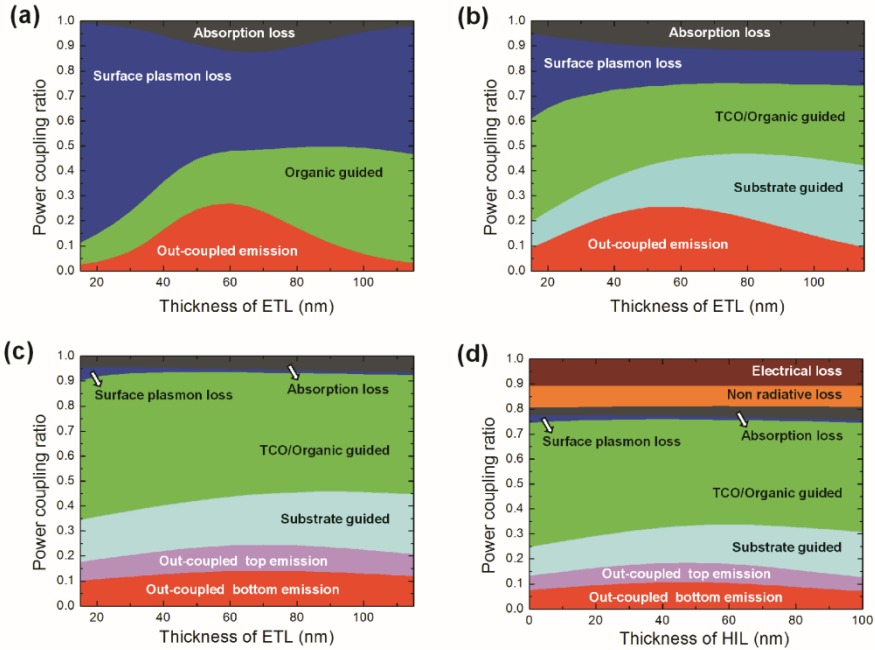


Figure 6.5 Mode analyses of the top emission, bottom emission and transparent OLEDs. The power coupling ratio simulated using the classical dipole model for (a) the top emission OLED with a metal cathode and anode, (b) the top emission OLED with a metal cathode and IZO anode, and (c) the transparent OLED with an ITO cathode and IZO anode. The photoluminescent quantum yield of the emitter is assumed to be 1 with a random orientation in the simulation. The device structures for the simulation are displayed in Figure S3. (d), simulated power coupling ratio of the reference transparent OLED where the optical loss coming from the PL quantum yield of 0.91 and the electrical loss of 11% are included in the simulation to fit with the experimental EQE value of 18.2%.

density in the TCO electrodes than metal electrodes. These results clearly indicate that there is much larger amount of extractable light (~93% of the emitted light) in the transparent OLED than in the OLEDs with the metal/metal or metal/TCO electrodes. It is interesting to note that the maximum out-coupling efficiency without any extra light extraction layers has the highest value, at 27%, in the top emission OLED with the metal/metal electrodes, followed by the metal/TCO electrodes, with a result of 26%. The OLED with the TCO/TCO electrodes showed the lowest out-coupling efficiency of 23% among the three OLEDs, because of the weakest microcavity effect.⁸⁷ We performed the mode analysis using a more realistic measured value of $q_{\text{PL}}=0.91$ for the 8 wt% Ir(ppy)₃ doped CBP and an isotropic orientation of the emitting dipoles.^{14,121,122} An electrical loss of 11% was applied in the simulation to match with the experimentally obtained EQE value (18.2%) in the OLED. The results are shown in Fig. 6.5d. The total extractable portion of the emitted light is 75.7%, including the substrate mode, the waveguide modes in the organic layer and the TCOs.

In addition, the extraction of the confined light inside the transparent OLED by integrating the microstructures was simulated using a 3 dimensional geometrical ray tracing method (LightTools). Two different combinations of light extraction structures on the top and bottom electrodes were selected for the simulation: a MCA (top)/MLA (bottom) and a MCA (top)/half-sphere (bottom). The MCA and MLA are assumed to have the fill factors of 100% and 90%, respectively. The height and the refractive index of the microstructures and the half sphere were systematically varied in the simulation to investigate their effects on light extraction. The diameter of the micro-cones was fixed at 60 μm in the simulation. A 2 mm \times 2 mm planar

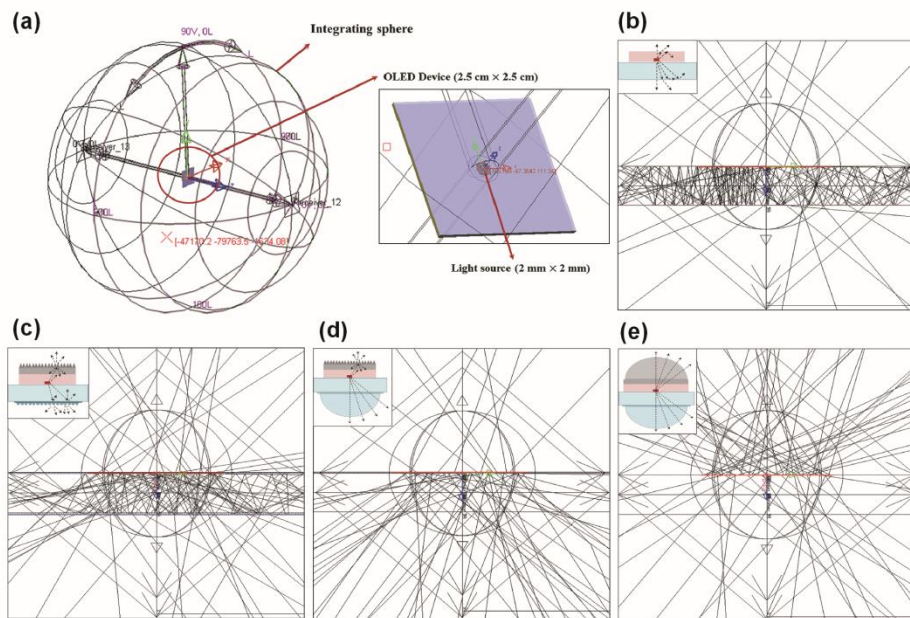


Figure 6.6 Geometry and results of 3 dimensional ray tracing. (a) Geometry of the ray tracing used for the simulation. A 2 mm x 2 mm planar light source on a 2.5 cm x 2.5 cm glass substrate is located at the center of an integrating sphere used as the detector. The planar light source consists of homogeneously spread 25,000 isotropic point sources in the square emissive area. (b)-(e), Ray tracing images of (b) the reference OLED, (c) the OLED with MCA/MLA, (d) the OLED with MCA/a half sphere, and (e) the OLED with 10 mm hemispheres on the both sides of the OLED. The simulation was performed using the LightTools .

light source located in the middle of the organic layer was used for the ray tracing, where the planar light source consisted of homogeneously spread 25,000 isotropic point sources in the square emissive area (see Fig. 6.6). The simulated incremental ratios of the EQE values compared to the reference OLED without the extraction structures are displayed in Fig. 6.7a-d as functions of the height (h) and the refractive index (n) of the structures. The light extraction increases as the refractive indices of the extraction structures approach the underlying TCOs due to the reduction of the reflection at the interfaces. The extraction efficiencies increase as the height of the microstructures and the half-sphere increases up to 35 nm, corresponding to the radius of each of the microlenses for the MLA and 80 nm for the MCA. Further increases of the heights in both structures give either the same extraction efficiency (MLA) or a reduced one (MCA). The trend is the same as has been previously reported in the literature.³⁴ The simulation results show that an enhancement of 2.7 times is possible for the OLED with the light extraction structures in Fig. 6.1a, where the micro-cones are characterized by $h \sim 80 \mu\text{m}$ and $n \sim 1.8$, and the micro-lenses are characterized by $h \sim 35 \mu\text{m}$ and $n \sim 1.52$. Even a higher enhancement of 3.45 times is possible for the OLED with the extraction structure of the MCA/half sphere with a diameter of 10 mm and $n \sim 1.52$. Application of the reference EQE value of 18.2% to the simulation results predicts that EQE values of 49.1% for the OLED with the MCA/MLA structure and of 62.8% for the OLED with the MCA/half-sphere lens are achievable, respectively. These theoretically predicted values are well matched with the experimentally obtained EQE values (47.3% for the OLED with the MCA/MLA structure and 62.9% for the OLED with the MCA/half sphere structure). Additionally, we carried out the simulation of

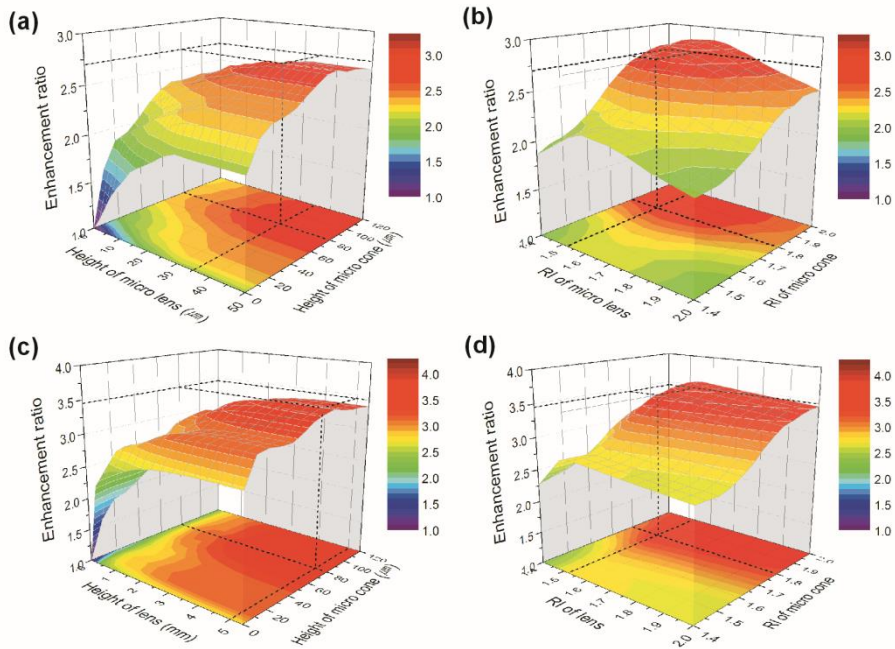


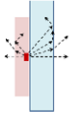
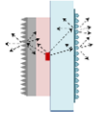
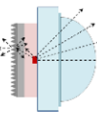
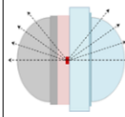
Figure 6.7 Simulation results of outcoupling enhancement ratio by the light extraction structures. Outcoupling enhancement ratios of the OLEDs with the MCA/MLA (a), (b) and with the MCA/half-sphere lens (c), (d) as functions of the height (a), (c) and the refractive index (b), (d) of the microcones, microlenses and the half-sphere. A 3 dimensional ray tracing simulation tool (LightTools) was used for the simulation. The MCA and MLA were assumed to have fill factors of 100% and 90%, respectively, and the diameter of the micro-cones was fixed to 60 μm in the simulation. A 2 mm \times 2 mm planar light source located in the middle of the organic layer was used for the ray tracing where the planar light source consisted of 25,000 homogeneously spread isotropic point sources in the square emissive area. Refractive indices of 1.52 and 2.0 were used for the glass substrate and IZO, respectively.

light extraction using two half-spheres (10 mm in diameter) attached on both sides of the transparent OLED. The refractive indices of the lenses are assumed to match with the underlying TCO. The increment ratio of the radiant flux is 4.24 times in this case, corresponding to the EQE value of 77.2% for the transparent OLEDs. If we assume that all the confined light in the OLED can be extracted by the two half sphere lenses, the ray tracing method gives a very good consistency with the simulation result based on the dipole model. All the simulation results are summarized in Table 6.1.

6.4 Simulation methods

Methodology of optical mode analysis: We used the classical dipole model to simulate the coupled power of various optical modes.⁴² This model is based on the classical electromagnetic theory with full vectorial scheme, where a molecular excited state is treated as an oscillating point dipole. The power dissipations of a dipole embedded in the optical microcavity was calculated as a function of the in-plane wave vector (k_x) and wavelength and classified into the optical modes through dividing power dissipation by the in-plane wave vector. The mode analysis was performed under the assumptions: First, the dipole radiators are embedded in the emitting layer as a sheet and the emitters are randomly distributed, which is a reasonable assumption for Ir(ppy)₃ in CBP.¹²⁰ Second, the emission zone is located at the center of the emitting layer. Third, the intrinsic PL quantum yield of the phosphorescent dye is assumed to be 91% that is a reasonable value for Ir(ppy)₃ in CBP. The complex refractive indices of all organic materials were measured by spectroscopic

Table 6.1 Quantum efficiency & Power efficiency for devices

Device structures	Experimental results @0.02 mA/cm ² , 3.7 V			Simulation results		
	EQE (%) (Bottom/Top)	Power Efficiency (lm/W)	Enhancement ratio	CPS model EQE (%)	LightTools Enhancement ratio	Calculated EQE (%)
 Reference	18.2 (13.0/5.2)	53.4		18.2		–
 Top Micro cone arrays Bottom Micro lens arrays	47.3 (31.8/15.5)	138.7	2.60		2.70	49.1
 Top Micro cone arrays Bottom Hemisphere lens	62.9 (53.6/9.3)	185.3	3.46		3.45	62.8
 Top Hemisphere lens Bottom Hemisphere lens	–	–		75.7 ^[a]	4.24	77.2

[a] This value is the summation of the power discipations to air mode and waveguide mode under the assumption that both modes can be extracted by the two hemispherical lenses.

ellipsometer.¹²³ The refractive indices of ITO, glass and IZO were found in elsewhere.¹²⁴⁻¹²⁶ The detailed procedure and formulation of the optical modeling have been described before [3,23,29,33]. Methodology of geometrical optics simulation: We performed the geometrical simulation by using a commercialized 3-dimensional optical simulation program (LightTools). Graphical illustration of the geometry and results of 3 dimensional ray tracing is displayed in Figure 5.3. A 2 mm x 2 mm planar light source located in the middle of the organic layer was used for the ray tracing, where the planar light source consisted of homogeneously spread 25,000 isotropic point sources in the square emissive area. The angle dependent spectrum and intensity of the light source obtained from the classical dipole model were used for the simulation. Radiant flux from the planar light source was integrated using a spherical detector surrounding the source, where the distance between the detecting surface and the light source was set to infinite. The same refractive indices as the mode analysis were used in the simulation. Three different geometries of MCA/OLED/MLA, MCA/OLED/half sphere and half sphere/OLED/half sphere were simulated. The MCA and MLA were assumed to have the fill factors of 100% and 90%, respectively. The height and the refractive index of the microstructures and the half sphere were systematically varied in the simulation to investigate their effects on light extraction. The diameter of the micro-cones was fixed at 60 μm in the simulation.

6.5 Conclusion

In summary, we demonstrated through simulation that the surface plasmon and intrinsic absorption loss in OLEDs can be significantly reduced by using a metal free transparent OLED based on TCO electrodes, in contrast to other OLEDs with metal electrodes, maximizing the total amount of extractable light. By integrating microstructures on both sides of a transparent OLED to extract the confined light, we have experimentally realized an OLED with an EQE value of 47.3%, enhanced from 18.2% without the microstructures. The efficiency was enhanced further to 62.9% by integrating a micro-cone array on one side and a half-sphere lens on the other side. The experimental results are well described by a combined simulation of the classical dipole model and the 3 dimensional ray tracing method. The simulation predicts that EQEs over 60% are possible by using the microstructures on both surfaces without any internal light extraction layer if the electrical loss is minimized and a phosphorescent dye with a photo luminescent quantum yield of 1 is used. Moreover, the transparent OLED with the microstructures showed no color shift with viewing angle. A simple process which combined the high efficiency and no color shift suggests the great potential of our device for application in solid state lighting.

Bibliography

- [1] A. Bernanose, M. Comte and P. Vouaux, *J Chim Phys Pcb* 50 (1), 64 (1953).
- [2] A. Bernanose and P. Vouaux, *J Chim Phys Pcb* 50 (4), 261 (1953).
- [3] H. Kallmann and M. Pope, *Nature* 186 (4718), 31-33 (1960).
- [4] H. Kallmann and M. Pope, *J Chem Phys* 32 (1), 300-301 (1960).
- [5] C.W. Tang, S. A. Vanslyke and C. H. Chen, *J Appl Phys* 65 (9), 360-3616 (1989).
- [6] S. J. Su, T. Chiba, T. Takeda and J. Kido, *Adv Mater* 20 (11), 2125-2130 (2008).
- [7] M. G. Helander, Z. B. Wang, J. Qin, M. T. Geiner, D. P. Puzzo, Z. W. Liu and Z. H. Lu, *Science* 332 (6032), 944-947 (2011).
- [8] Y.-S. Park, S. Lee, K.-H. Kim, J.-H. Lee and J.-J. Kim *Adv. Funct. Mater.* 23, 4914 (2013).
- [9] J. Kido, K. Nagai, Y. Okamoto and T. Skotheim, *Appl Phys Lett* 59 (21), 2760-2763 (1991)
- [10] T. R. Hebner, C. C. Wu, D. Marcy, M. H. Lu and J. C. Sturm, *Appl Phys Lett* 72 (5), 519-521 (1998)
- [11] D. A. Pardo, G. E. Jabbour and N. Peyghambarian, *Adv Mater* 12 (17), 1249 (2000).
- [12] P. Kopola, M. Tuomikoaki, R. Suhonen and A. Maaninen, *Thin Solid Film* 517 (19), 5757-5762 (2009)
- [13] M.A. Baldo, D. F. O'Brien, Y. You, A. Shoustikov, S. Sibley, M. E. Thompson and S. R. Forrest, *Nature* 395 (6698), 151-154 (1998).

- [14] C. Adachi, M. A. Baldo, M. E. Thompson, S.R. Forrest, *J. Appl. Phys.* 90, 5048 (2001)
- [15] Y. Kawamura, K. Goushi, J. Brooks, J. Brown, H. Sasabe and C. Adachi, *Appl. Phys. Lett.* 86, 071104 (2005)
- [16] S. Nowy, B. C. Krummacher, J. Frischeisen, N. A. Reinke, and W. Brütting, *J. Appl. Phys.* 104, 123109, (2008).
- [17] R. Meerheim, M. Furno, S. Hofmann, B. r. Lüssem, K. Leo, *Appl. Phys. Lett.* 97, 253305 (2010).
- [18] H. Ishii, K. Sugiyama, E. Ito, and K. Seki. *Advanced Materials* 11(8) 605–625 (1999).
- [19] I. G. Hill, D. Milliron, J. Schwartz, and A. Kahn. *Applied Surface Science.* 166 354–362 (2000).
- [20] K. Seki, N. Hayashi, H. Oji, E. Ito, Y. Ouchi, and H. Ishii. *Thin Solid Films* 393 298–303 (2001).
- [21] H. Sasabe , J.-I. Takamatsu , T. Motoyama , S. Watanabe , G. Wagenblast , N. Langer , O. Molt , E. Fuchs , C. Lennartz , and J. Kido, *Adv. Mater.* 22(45) 5003–5007 (2010).
- [22] L. Xiao, S.-J. Su, Y. Agata, H. Lan, and J. Kido, *Adv. Mater.* 21(12) 1271 (2009).
- [23] S.-J. Su, Y. Takahashi, T. Chiba, T. Takeda, *Adv. Funct. Mater.* 19(8) 1260-1267 (2009).
- [24] S.-Y. Kim, W.-I. Jeong, C. Mayr, Y.-S. Park, K.-H. Kim, J.-H. Lee, C.-K. Moon, W. Brütting and J.-J. Kim, *Adv. Funct. Mater.* 23, 3896 (2013).
- [25] J. -S. Kim, P. K. H. Ho, N. C. Greenham, R. H. Friend, *J. Appl. Phys.* 88, 1073 (2000).
- [26] C. F. Madigan, M. H. Lu, J. C. Sturm, *Appl. Phys. Lett.* 76, 1650 (2000).
- [27] M. H. Lu, J. C. Sturm, *J. Appl. Phys.* 91, 595 (2002).

- [28] L. H. Smith, J. A. E. Wasey and W. L. Barnes, *Appl Phys Lett* 84 (16), 2986-2988 (2004).
- [29] C. C. Wu, C. L. Lin, P. Y. Hsieh and H. H. Chiang, *Appl Phys Lett* 84 (20), 3966-3968 (2004).
- [30] C. L. Lin, T. Y. Cho, C. H. Chang and C. C. Wu, *Appl Phys Lett* 88, (8) (2006).
- [31] C. L. Mulder, K. Celebi, K.M. Milaninia and M. A. Baldo, *Appl Phys Lett* 90, (21) (2007).
- [32] C. L. Lin, H. C. Chang, K. C. Tien and C. C. Wu, *Appl Phys Lett* 90, (7) (2007).
- [33] W. I. Jeong, S. Y. Kim, J. J. Kim and J. W. Kang, *Chem Phys* 355 (1), 25-30 (2009).
- [34] Y. Sun, S. R. Forrest, *J. Appl. Phys.* 100, 073106 (2006).
- [35] C.-J. Yang, S.-H. Liu, H.-H. Hsieh, C.-C. Liu, T.-Y. Cho, C.-C. Wu, *Appl. Phys. Lett.* 91, 253508 (2007).
- [36] M. Thomschke, S. Reineke, B. Lüssem, K. Leo, *Nano Letters.* 12, 424 (2012).
- [37] A. Badano and J. Kanicki, *J. Appl. Phys.* 90, 1827 (2001).
- [38] S. J. Lee, A. Badano, and J. Kanicki, *IEEE J. Sel. Top. Quantum Electron.* 10, 37 (2004).
- [39] J. J. Shiang and A. R. Duggal, *J. Appl. Phys.* 95, 2880 (2004).
- [40] J. J. Shiang, T. J. Faircloth, and A. R. Duggal, *J. Appl. Phys.* 95, 2889 (2004).
- [41] R. R. Chance, A. Prock, and R. Silbey, *Adv. Chem. Phys.* 37, 1 (1978).
- [42] W. L. Barnes, *J. Mod. Opt.* 45, 661 (1998).

- [43] M. Furno, R. Meerheim, S. Hofmann, B. Lüsse, and K. Leo, *Phys. Rev. B.* 85, 115205 (2012).
- [44] Y. R. Do, Y. -C. Kim, Y. -W. Song, Y. -H. Lee, *J. Appl. Phys.* 96, 7629 (2004).
- [45] A. Chutinan, K. Ishihara, T. Asano, M. Fujita, S. Noda, *Org. Electron.* 6, 3 (2005).
- [46] A. O. Altun, S. Jeon, J. Shim, J. -H. Jeong, D. -G. Choi, K. -D. Kim, J. -H. Choi, S. -W. Lee, E. -S. Lee, H. -D. Park, J. R. Youn, J. -J. Kim, Y. -H. Lee, J. -W. Kang, *Org. Electron.* 11, 711. (2010).
- [47] M. K. Callens, H. Marsman, L. Penninck, P. Peeters, H. Groot, J. M. Meulen, and K. Neyts, *Opt. Express.* 22, A589 (2014).
- [48] J.-W. Kim, J.-H. Jang, M.-C. Oh, J.-W. Shin, D.-H. Cho, J.-H. Moon, and J.-I. Lee, *Opt. Express.* 22, 498 (2014).
- [49] H. Greiner, *J. J. Appl. Phys.* 46, 4125 (2007).
- [50] G. Gaertner, H. Greiner, *Proc. of SPIE.* 6999, 69992T-1 (2008).
- [51] G. Gu, V. Bulovic, P. E. Burrows, S. R. Forrest and M. E. Thompson, *Appl. Phys. Lett.* 68, 2606 (1996).
- [52] S.R. Forrest, *Org. Electron.* 4, 45 (2003).
- [53] S. Chen, L. Deng , J. Xie , L. Peng , L. Xie , Q. Fan , and W. Huang, *Adv. Mater.* 22, 5227 (2010).
- [54] S. Hofmann, M. Thomschke, B. Lüsse, and K. Leo, *Opt. Express.* 19, 1250 (2011).
- [55] E. Najafabadi, K. A. Knauer, W. Haske, C. Fuentes-Hernandez, and B. Kippelen, *Appl. Phys. Lett.* 101, 023304 (2012).

- [56] M. Thomschke, S. Reineke, B. Lüssem, and K. Leo, *Nano Letters*. 12, 424 (2012).
- [57] C. C. Wu, C. W. Chen, C. L. Lin, and C. J. Yang, *J. Disp. Technol.* 1 (2), 248 (2005).
- [58] J.-H. Lee, D.-S. Leem, J.-J. Kim, *Org. Electron.* 11, 2055 (2008)
- [59] D. -S. Leem, S.-Y. Kim, J.-H. Lee, and J.-J. Kim, *J. Appl. Phys.* 106, 063114 (2009).
- [60] J.-H. Lee, P.-S. Wang, H.-D. Park, C.-I. Wu, J.-J. Kim, *Org. Electron.* 12, 1763 (2011)
- [61] J.-H. Lee, J.-J. Kim, *Journal of Information Display.* 14, 39 (2013)
- [62] A. B. Djurusic, and A. D. Rakic, *Appl. Opt.* 41, 7650 (2002).
- [63] C.-C. Wu, C.-L. Lin, P.-Y. Hsieh, and H.-H. Chiang, *Appl. Phys. Lett.* 84, 3966 (2004).
- [64] J.-H. Lee, K.-Y. Chen, C.-C. Hsiao, H.-C. Chen, C.-H. Chang, Y.-W. Kiang, and C. C. Yang, *J. Disp. Tech.* 2, 130 (2006).
- [65] S. Hofmann, M. Thomschke, P. Freitag, M Furno, B. Lüssem, and K. Leo, *Appl. Phys. Lett.* 97, 253308 (2010).
- [66] H. Riel, S. Karg, T. Beierlein, W. Rieß, and K. Neyts, *J. Appl. Phys.* 94, 5290 (2003).
- [67] C.W. Chen, C.L. Lin, and C.C. Wu, *Appl. Phys. Lett.* 85 (13), 27 (2004).
- [68] X. W. Zhang, H.P. Lin, J. Li, L. Zhang, B. Wei, X. Y. Jiang, Z. L. Zhang, *J. Luminance.* 132, 1 (2008).

- [69] S. Hofmann, R. Nitsche, M Furno, and K. Leo, *Appl. Phys. Lett.* 94, 083303 (2009)
- [70] J. Yamamori, S. Hayashi, T. Koyama, and Y. Taniguchi, *Appl. Phys. Lett.* 78, 3343 (2001).
- [71] T. Dobbertin, M. Kroeger, D. Heithecker, D. Schneider, D. Metzdorf, H. Neuner, E. Becker, H.-H. Johannes, and W. Kowalsky, *Appl. Phys. Lett.* 82(2), 284 (2003).
- [72] S. Chena, R. Songb, J. Wangb, Z. Zhaob, Z. Jieb, Y. Zhaob, B. Quanb, W. Huangb, S. Liub, *J. Luminance.* 128, 1143 (2008).
- [73] J. Meyer, T. Winkler, S. Hamwi, S. Schmale, H.-H. Johannes, T. Weimann, P. Hinze, W. Kowalsky and T. Riedl, *Adv. Mater.* 20, 3839 (2008).
- [74] H. Lin, J. Yuy, S. Lou, J. Wang and Y. Jiang, *J. Mater. Sci. Technol.* 24 (2), (2008).
- [75] J.-H. Lee, S. Lee, J.-B. Kim, J.-H. Jang, J.-J. Kim, *J. Mater. Chem.* 22, 15262 (2012).
- [76] C. E. Small, S.-W. Tsang, J. Kido, S. K. So, and Franky So, *Adv. Funct. Mater.* 22, 3261 (2012).
- [77] E. Najafabadi, K. A. Knauer, W. Haske, and B. Kippelen, *Org. Electron.* 14, 1271 (2013).
- [78] J.-B. Kim, J.-H. Lee, C.-K. Moon, S.-Y. Kim and J.-J. Kim, *Adv. Mater.* 25, 3571 (2013).

- [79] S. Lee, K.-H. Kim, D. Limbach, Y.-S. Park and J.-J. Kim, *Adv. Funct. Mater.* 23, 4105 (2013)
- [80] S. Hofmann, M. Thomschke, B. Lüssem, K. Leo, *Opt. Express.* 19, A1250 (2011).
- [81] M. Thomschke, S. Reineke, B. Lüssem, K. Leo, *Nano Letters.* 12, 424 (2012).
- [82] T. Schwab, S. Schubert, S. Hofmann, M. Fröbel, C. Fuchs, M. Thomschke, L. Müller-Meskamp, K. Leo, M.C. Gather, *Adv. Opt. Mater.* 1, 707 (2013).
- [83] H. Becker , S. E. Burns , R. H. Friend , *Phys. Rev. B.* 56. 1893-1905 (1997).
- [84] J. A. E. Wasey, A. Safonov, I. D. W. Samuel, W. L. Barnes, *Opt. Commun.* 183, 109-121 (2000).
- [85] J. -S. Kim, P. K. H. Ho, N. C. Greenham, R. H. Friend, *J. Appl. Phys.* 88, 1073 (2000).
- [86] H.-W. Lin, C.-L. Lin, H.-H. Chang, Y.-T. Lin, C.-C. Wu, Y.-M. Chen, R.-T. Chen, Y.-Y. Chien, K.-T. Wong. *J. Appl. Phys.* 95, 881 (2004).
- [87] H.-W. Lin, C.-L. Lin, C.-C. Wu, T.-C. Chao, K.-T. Wong, *Appl. Phys. Lett.* 87, 071910 (2005).
- [88] H.-W. Lin, C.-L. Lin, C.-C. Wu, T.-C. Chao, K.-T. Wong, *Org. Electron.* 8, 189-197 (2007).
- [89] J. Frischeisen, D. Yokoyama, A. Endo, C. Adachi, W. Brütting, *Org. Electron.* 12, 809-817 (2011).
- [90] F. Michael, J. Frischeisen, D. S. Setz, D. Michaelis, B. C. Krummacher, T. D. Schmidt, W. Brütting, N. Danz, *Org. Electron.* 12, 1663-1668 (2011).
- [91] P. Liehm, C. Murawski, M. Furno, B. Lüssem , K. Leo, M. C. Gather,

- Appl. Phys. Lett. 101, 253304 (2012).
- [92] K.-H. Kim, C.-K. Moon, J.-H. Lee, S.-Y. Kim, J.-J. Kim, Adv. Mater. 26, 3844 (2014).
- [93] W. -I. Jeong, S. Y. Kim, J. -J. Kim, and J. W. Kang, Chemical Physics. 355, 25 (2009).
- [94] J. C. de Mello, H. F. Witmann, R. H. Friend, Adv. Mater. 9, 230 (1997).
- [95] S.-Y. Kim, J.-J. Kim, Org. Electron. 1, 1010-1015 (2010).
- [96] S. Möller, S. R. Forrest, J. Appl. Phys. 91, 3324 (2002).
- [97] H. Kwon, Y. Yee, C. -H. Jeong, H. -J. Nam, J.-U. Bu, J. Micromech. Microeng. 2008, 18, 065003.
- [98] T. Tsutsui, M. Yahiro, H. Yokogawa, K. Kawano, M. Yokoyama, Adv. Mater. 13, 1149-1152 (2001).
- [99] Y. R. Do, Y. -C. Kim, Y. -W. Song, Y.-H. Lee, J. Appl. Phys. 96, 7629 (2004).
- [100] T. Nakamura, H. Fujii, N. Juni, N. Tsutsumi, Opt. Rev. 13, 104-110 (2006).
- [101] Y. Sun, S. R. Forrest, Nature Photon. 2, 483-487 (2008).
- [102] S. Jeon, J. -W. Kang, H. -D. Park, J. -J. Kim, J. R. Youn, J. Shim, J. -H. Jeong, D. -G. Choi, K. -D. Kim, A. O. Altun, S. -H. Kim, Y. -H. Lee Kim, S. Jeon, J. -H. Jeong, Appl. Phys. Lett. 92, 223307 (2008).
- [103] H. -H. Cho, B. Park, H. -J. Kim, S. Jeon, J. -H. Jeong, J. -J. Kim, Appl. opt. 49, 21, 4024-4028 (2010).
- [104] H. -H. Cho, B. Park, H. -J. Kim, J. Shim, S. Jeon, J. -H. Jeong, J. -J. Kim, Currr. Appl. Phys.10, e139-2142 (2010).
- [105] C.-C. Liu, S.-H. Liu, K.-C. Tien, M.-H. Hsu, H.-W. Chang, C.-K. Chang, C.-J. Yang, C.-C. Wu, Appl. Phys. Lett. 94, 103302 (2009).

- [106] Y. Jin, J. Feng, X.-L. Zhang, Y.-G. Bi, Y. Bai, L. Chen, T. Lan, Y.-F. Liu, Q.-D. Chen, H.-B. Sun, *Adv. Mater.* 24, 1187 (2012).
- [107] T. Schwab, C. Fuchs, R. Scholz, A. Zakhidov, K. Leo, M. C. Gather, *Opt. Express.* 22, 7524 (2014).
- [108] E. Wrzesniewski, S.-H. Eom, W. T. Hammond, S. Lee, E. P. Douglas, J. Xue, *Small.* 8, 2647 (2012).
- [109] J.-H. Lee, P.-S. Wang, H.-D. Park, C.-I. Wu, J.-J. Kim, *Org. Electron.* 12, 1763 (2011).
- [110] S. Reineke, F. Linder, G. Schwartz, N. Seidler, K. Walzer, B. Lüssem, K. Leo, *Nature.* 459, 234-238 (2009).
- [111] J.-B. Kim, J.-H. Lee, C.-K. Moon, J.-J. Kim, *Appl. Phys. Lett.* 104, 073301 (2014).
- [112] J.-B. Kim, J.-H. Lee, C.-K. Moon, S.-Y. Kim, J.-J. Kim, *Org. Electron.* 15, 2715-2718 (2014).
- [113] W. H. Koo, S. M. Jeong, F. Araoka, K. Ishikawa, S. Nishimura, T. Toyooka, H. Takezo, *Nature Photon.* 4, 222-226 (2010).
- [114] A. O. Altun, S. Jeon, J. Shim, J. -H. Jeong, D. -G. Choi, K. -D. Kim, J. -H. Choi, S. -W. Lee, E. -S. Lee, H. -D. Park, J. R. Youn, J. -J. Kim, Y. -H. Lee, J. -W. Kang *Org. Electron.* 11, 711-716 (2010).
- [115] W. H. Koo, W. Youn, P. Zhu, X.-H. Li, N. Tansu, F. So, *Adv. Funct. Mater.*, 22, 3454-3459 (2012).
- [116] Z. B. Wang, M. G. Helander, J. Qiu, D. P. Puzzo, M. T. Greiner, Z. M. Hudson, S. Wang, Z. W. Liu, Z. H. Lu, *Nature Photon.* 5, 753-757 (2011).
- [117] S. Nowy, J. Frischeisen, W. Brütting, *Proc. of SPIE.* 7415 74151C (2009).

- [118] S. R. Forrest, D. D. C Bradley, M. E. Thomson, *Adv.Mater.* 15, No.13 (2003).
- [119] I. Tanaka, S. Tokito, *Jpn. J. Appl. Phys.* 43, 7733-7736 (2004).
- [120] W. Brütting, J. Frischeisen, T. D. Schmidt, B. J. Scholz, C. Mayr, *phys. status solidi a.* 1-22 (2012).
- [121] Y. Kawamura, K. Goushi, J. Brooks, J. J. Brown, H. Sasabe, C. Adachi, *Appl. Phys. Lett.* 86, 071104 (2005).
- [122] W. -I. Jeong, S. Y., Kim, J.-J. Kim, J. W. Kang, *Chem. Phys.* 355, 25-30 (2009).
- [123] Refractive indices were measured by KRISS (Korea Research Institute of Standards and Science).
- [124] R. A. Synowicki, *Thin Solid Films.* 394, 313–314 (1998).
- [125] E. D. Palik and G. Ghosh, *Handbook of optical constants of solids.* (Academic Press, San Diego, 1998)
- [126] Y. S. Jung, J. Y. Seo, D. W. Lee, D. Y. Jeon, *Thin Solid Films.* 445, 63-71 (2003).

초록

유기발광소자는 디스플레이와 조명산업에 사용되기 위해 고효율과 고품질의 색 특성이 요구 된다. 본 학위 논문에서는 유기발광소자에서 발생하는 광 손실을 분석과 함께 광 추출을 위한 수치모사 방법을 소개한다. 더하여, 인버티드 타입의 상부 발광소자와 투명소자에 광 추출 구조를 적용하여, 실험과 이론 분석을 수행하였고 높은 효율과 고품질의 색 특성을 얻었다.

제1장에서는 유기발광소자의 구동원리와 내부, 외부 양자효율을 결정하는 요소와 광 손실의 주된 원인인 표면 플라즈몬 현상에 대해 정리하였다. 제2장에서는 광 추출 구조가 적용 된 유기발광소자의 광학 분석 방법을 제안 하였다. 고전 쌍극자 모델과 선형광학계 분석법을 융합하여 적용한 분석법을 개발하여, 각도에 따른 광의 세기 분포, 상부 구조물의 광 추출 특성, 유기발광소자가 이루는 각도에 따른 반사율을 모델링 하여 광 추출 구조가 적용된 유기 발광소자의 광 추출 효율 수치모사 방법을 제안하였다. 제3장에서는 투명 전도성 산화물 전극을 상부 전극으로 사용하는 상부 발광 형 유기발광소자를 구현하고 광학 특성을 분석하였다. 일반적인 상부 발광 형 유기발광소자는 얇은 금속을 상부 전극으로 사용하기 때문에 외부 양자 효율이 최대가 되는 소자 구조 적용 시 공진 효과의 영향으로 인하여 각도에 따른 스펙트럼의 변화가 크고, 금속 전극이 양방향으로 구성되어 표면 플라즈몬으로 인한 에너지 손실이 크다. 제3-1장에서는 상부 전극을 투명 전도성 산화물 상부 전극으로 사용함으로써 높은 양자 효율을 얻는 구조에서도 공진구조에 의한 광 세기의 파장의존성이 줄어 시야 각에 따른 스펙트럼 변화가 적은 소자

를 제작하였다. 결과로 110 cd/A 색 좌표의 각도에 따른 변화가 0~60도의 범위에서 $dx=0.02$, $dy=0.02$ 인 결과를 얻었다. 이에 더하여, 제3-2장에서는 수평 배향율이 높은 발광체를 상부 발광 형 유기발광소자에 적용하였다. 분자의 수평: 수직 배향율이 0.78:0.22인 Ir(ppy)₂tmd를 사용하여 소자를 제작하였고 결과로 120.7 cd/A의 전류효율, 27.6%의 외부양자효율을 갖은 인광 초록 발광 소자를 제작하였다. 또한, 수평 배향율과 발광체의 절대발광효율을 변수로 하여 수평 배향율과 절대 발광효율이 모두 100%일 경우 44.7%의 외부양자효율까지 도달할 수 있는 이론적인 한계치를 계산하였다. 제4장에서는 백색의 상부 발광 형 유기발광소자를 무 반사 특성을 갖는 기능 층을 적용하여 제작하였다. 전도성 산화물 전극을 기반으로 하는 상부 발광 형 유기발광소자의 상부에 굴절률이 낮은 LiF ($n=1.39 @550 \text{ nm}$)를 파장의 길이의 1/4에 해당하는 위상정합 조건에 대한 두께 적용 시 모든 가시 광 영역의 범위에서 4%이하의 반사율을 얻을 수 있음을 보였다. 이를 백색의 상부 발광 형 유기발광소자에 적용하여 색 온도 2200K 와 3000K의 흑체 복사를 만족하는 상태에서 각도에 따른 스펙트럼의 변화가 0 ~ 60도 까지 $dx=0.02$, $dy=0.01$ 을 유지하며, 외부 양자 효율이 각각 18.8% 와 16.9%인 고 효율과 함께 고품질의 색 특성을 얻을 수 있는 결과를 얻었다. 제5장에서는 금속 산화물 전극기반의 상부 발광 형 유기발광소자에 직접 광 추출 구조를 제작, 적용하였다. 유기물을 육각배열의 다공이 형성된 금속 마스크를 사용하여 진공 증착 법을 이용하였고 증착속도를 점차 줄이는 방법으로 표면의 곡률을 만들어 미소렌즈구조물을 형성하였다. 결과로 27.6%의 외부양자효율이 44.7%로, 120.7 cd/A의 전류효율이

217.2 cd/A로 증가한 결과를 얻었다. 이는 제2장에서 소개된 광 추출 효율 수치모사방법을 통하여 선행분석 되었으며, 양자효율에 대한 추출 증가 량의 비교를 통하여 이론계산과 실험결과가 잘 일치 함을 보였다. 이에 더하여, 상부 구조물의 굴절률정합으로 인한 공진 효과가 상쇄로 각도에 따른 스펙트럼이 발광체의 본연의 발광특성에 가까워 지는 결과를 얻었고, 광 추출 구조가 발광체와 매우 가까운 거리로 직접 적용 되어 픽셀 블러링 현상이 거의 없는 디스플레이에 적용 가능성을 보여주는 결과를 얻었다. 제6장에서는 표면플라즈몬 효과가 극소화된 양 방향에 투명 전도성 산화물 전극을 사용한 유기발광 소자에 광 추출 구조를 적용하였다. 플라즈몬 손실이 극소화된 소자는 이상적인 경우 90%이상의 양자효율이 추출 가능한 소자내부 도파 광으로 변환됨을 보였으며, 실제 절대 발광 효율과 전기적인 손실을 고려한 내부 추출 가능 총 광량을 계산을 통하여 산출하였다. 18.2%의 외부양자효율을 갖는 투명소자의 양방향에 미세렌즈구조를 반구 형과 원뿔 형으로 각각 하부와 상부에 적용하여 47.3%을 하부 유리 기판상에 반구 렌즈를 적용하여 62.9%의 외부 양자 효율을 얻었다. 이러한 광 추출 증가 량의 결과는 고전쌍극자 모델과 삼차원 광 추적 모델을 혼합 적용 한 수치모사 방법을 통하여 분석 되었다.

주요어: 광학 모드 분석, 표면 플라즈몬 손실, 광 추출 수치모사, 투명전극 기반 인버티드 유기발광 다이오드

학번: 2011-30932

CURRICULUM VITAE

Kim Jung-Bum

Department of Materials Science and Engineering,

Seoul National University, Seoul, 151-742, Korea

+82-2-875-2412(office), +82-2-889-8702(fax)

E-mail: kjbum@snu.ac.kr

Education

2011.9 ~ 2015.2 **Ph.D.** in Department of Materials Science and

Engineering, Seoul National University, Seoul, Korea

Supervisor: Prof. Jang-Joo Kim

Thesis: "Optical analysis method for light extraction and transparent top electrode based inverted organic light emitting diodes with high efficiency and high color quality"

2003.2 ~ 2005.2 **M.S.** in Department of Physics, Hanyang University,

Seoul, Korea

Supervisor: Prof. Cha-Hwan Oh

Thesis: "Four-wave mixing based on electromagnetically induced transparency on standing wave pump field in Cs vapor cell"

1995.3 ~ 1999.2 **B.S.** in Department of Physics, Hanyang University,

Seoul, Korea

Experiences

2005.1 ~ 2011.9 **LG. Chem. Research Park,**

IT&E Materials R&D, Manager

Professional Activities

A. Membership:

- Member of the SPIE
- Member of the Polymer Society of Korea

Research Interests

Organic Light Emitting Diodes, Optical Mode Analysis, Surface Plasmonic Loss, Optical Simulation Methodology, Inverted Organic Light Emitting Diode, Nano and Micro Structures for light manipulation.

Professional Skills

Organic electronic device fabrication, device characteristics measurement, EL emission pattern measurement, UV-visible-NIR absorption spectroscopy, Photoluminescence (PL) spectroscopy, Electroluminescence (EL) spectroscopy, Absolute PL quantum yield measurement, FE-SEM, AFM, XPS, UPS, surface profiler, Optical simulation programs (LightTools, SETFOS)

List of Awards

1. Jung-Bum Kim, “Enhanced light out-coupling from surface plasmonic loss minimized transparent organic light-emitting diodes”, Best Student Paper Award, 2nd Place, Organic Photonics + Electronics, SPIE Optics + Photonics, 2013.
2. Jung-Bum Kim, “Highly enhanced light extraction from surface plasmonic loss minimized organic light emitting diodes”, Best paper award, The Polymer Society of Korea, 2013.

List of Publication

1. **Jung-Bum Kim**, Chang-Ki Moon, Jeong-Hwan Lee and Jang-Joo Kim, “Highly efficient inverted top emitting white organic light emitting diodes with high color quality using broadband anti-reflective top electrode”, *In preparation*.
2. **Jung-Bum Kim**, Jeong-Hwan Lee, Chang-Ki Moon, Kwon-Hyeon Kim and Jang-Joo Kim, “Highly enhanced light extraction from organic light emitting diodes with little image blurring and good color stability”, *In preparation*.
3. **Jung-Bum Kim** ‡, Seung-Hoon Han ‡, Kiyull Yang, Soon-Ki-Kwon, Jang-Joo Kim and Yun-Hi Kim “Highly efficient deep-blue phosphorescence from heptafluoropropyl-substituted iridium complexes”, *Chem. Commun.* DOI: 10.1039/c4cc07768g, 2014.

‡ These authors contributed equally to this work.
4. **Jung-Bum Kim**, Jeong-Hwan Lee, Chang-Ki Moon, Kwon-Hyeon Kim and Jang-Joo Kim, “Highly efficient inverted top emitting organic light emitting diodes using a horizontally oriented green phosphorescent emitter”, *Organic Electronics* 15, 2715–2718. (2014)
5. **Jung-Bum Kim** ‡, Jeong-Hwan Lee ‡, Chang-Ki Moon, and Jang-Joo Kim, “Highly efficient inverted top emitting organic light emitting diodes using a transparent top electrode with color stability on viewing angle”, *Applied Physics Letters* 104, 073301. (2014)

‡ These authors contributed equally to this work.

6. Yang Doo Kim, Kyeong-Hoon Han, Sang-Jun Park, **Jung-Bum Kim**, Ju-Hyeon Shin, Jang Joo Kim, and Heon Lee “Enhanced light extraction efficiency in organic light emitting diodes using a tetragonal photonic crystal with hydrogen silsesquioxane”, *Optics Letters*, 39, 20, 5901 (2014)

7. **Jung-Bum Kim**, Jeong-Hwan Lee, Chang-Ki Moon, Sei-Yong Kim and Jang-Joo Kim, “Highly Enhanced Light Extraction from Surface Plasmonic Loss Minimized Organic Light-Emitting Diodes”, *Advanced Materials* 25, 3571–3577. (2013)

8. Jeong-Hwan Lee, Sunghun Lee, **Jung-Bum Kim**, JunHyuk Jang and Jang-Joo Kim, “A high performance transparent inverted organic light emitting diode with 1,4,5,8,9,11-hexaazatriphenylene-hexacarbonitrile as an organic buffer layer”, *Journal of Materials Chemistry*, 22, 15262 (2012)

List of Presentations

1. **Jung-Bum Kim**, Jeong-Hwan Lee, Chang-Ki Moon, Sei-Yong Kim, Jang-Joo Kim "Highly Enhanced Light Out-coupling from Surface Plasmonic Loss Minimized Transparent Organic Light-Emitting Diodes", 2014 Materials Fair, September 25, 2014, Korea
2. **Jung-Bum Kim**, Jeong-Hwan Lee, Chang-Ki Moon, and Jang-Joo Kim, "Highly efficient inverted top emitting organic light emitting diodes using a transparent top electrode with color stability on viewing angle", SPIE Optics+Photonics 2014, Aug 17-21 (Aug 20), 2014, USA
3. **Jung-Bum Kim**, Jeong-Hwan Lee, Chang-Ki Moon and Jang-Joo Kim "Highly Efficient Inverted Top Emitting Organic Light Emitting Diode Using a Transparent Top Electrode", The 14th International Meeting on Information Display (iMiD 2014), August 26-29, 2014, Korea
4. **Jung-Bum Kim**, Jeong-Hwan Lee, Chang-Ki Moon, Sei-Yong Kim, Jang-Joo Kim "Highly Enhanced Light Out-coupling from Surface Plasmonic Loss Minimized Transparent Organic Light-Emitting Diodes", 10th International Conference on Electroluminescence and Organic Optoelectronics (ICEL), August 31-September 3, 2014, Germany
5. **Jung-Bum Kim**, Jeong-Hwan Lee, Chang-Ki Moon, Sei-Yong Kim, Jang-Joo Kim "Enhanced Light Extraction from Surface Plasmonic Loss Minimized Organic Light-Emitting Diodes", The 5th International Conference on White LEDs and Solid State Lighting, June 1-5 (June 2), 2014, Korea
6. **Jung-Bum Kim**, Jeong-Hwan Lee, Chang-Ki Moon, Sei-Yong Kim, and Jang-Joo Kim, "Enhanced light out-coupling from surface plasmonic loss minimized transparent organic light-emitting diodes",

The 5th International Workshop on Flexible & Printable Electronics 2013 (IWFPE 2013), November 20-22 (November 21), 2013, Korea

7. **Jung-Bum Kim**, Jeong-Hwan Lee, Chang-Ki Moon, Sei-Yong Kim, and Jang-Joo Kim, "Enhanced light out-coupling from surface plasmonic loss minimized transparent organic light-emitting diodes", 5th Asian Conference on Organic Electronics (A-COE 2013), November 13-15 (November 14), 2013, Korea
8. Chang-Ki Moon, Sei-Yong Kim, **Jung-Bum Kim**, Jeong-Hwan Lee, and Jang-Joo Kim, "Optical analysis of external quantum efficiency & total extractable light amount in OLEDs with different electrode types", KJF-ICOMEF 2013 (KJF International Conference on Organic Materials for Electronics and Photonics), August 28-31 (August 30), 2013, Korea
9. Chang-Ki Moon, Sei-Yong Kim, **Jung-Bum Kim**, Jeong-Hwan Lee, and Jang-Joo Kim, "Optical analysis of external quantum efficiency & total extractable light amount in OLEDs with different electrode types", IMID 2013 (The 13th International Meeting on Information Display), August 26-29 (August 29), 2013, Korea
10. Jeong-Hwan Lee, Sunghun Lee, **Jung-Bum Kim**, Junhyuk Jang, Hyo Jung Kim, and Jang-Joo Kim, "Hexaazatriphenyl-Hexanitrile (HATCN) as an anode buffer layer for high performance transparent inverted OLEDs", SPIE Optics+Photonics 2013, 25-29 August (27 August), 2013, USA
11. **Jung-Bum Kim**, Jeong-Hwan Lee, Chang-Ki Moon, Sei-Yong Kim, and Jang-Joo Kim, "Enhanced light out-coupling from surface plasmonic loss minimized transparent organic light-emitting diodes", SPIE Optics+Photonics 2013, 25-29 August (26 August), 2013, USA
12. Jeong-Hwan Lee, Sunghun Lee, **Jung-Bum Kim**, JunHyuk Jang, Jang-Joo Kim, "Hexaazatriphenylene-Hexanitrile (HATCN) buffer layer for high performance transparent inverted OLEDs", IWFPE 2012, 2012.11.16(2012.11.14-16)

13. Jeong-Hwan Lee, Sunghun Lee, **Jung-Bum Kim**, JunHyuk Jang and Jang-Joo Kim, " Hexaazatriphenylene-Hexanitrile Buffer layer for high performance transparent inverted organic light-emitting diodes", IMID 2012, Aug. 28, 2012

List of Patents

1. Yeon Keun Lee, Dae Hee Lee, Moon Soo Park, Yun Hye Hahm, **Jung-Bum Kim**, Mun Kyu Joo. “ORGANIC ELECTROLUMINESCENT DEVICE AND METHOD FOR FABRICATING THE SAME”, US8687145 , Apr. 1, 2014.
2. Min-Soo Kang, Jeoung-Kwen Noh, Se-Hwan Son, **Jung-Bum Kim**. “STACKED ORGANIC LIGHT EMITTING DIODE”, US8687854, Jan. 28, 2014.
3. Min-Soo Kang, Jeoung-Kwen Noh, Se-Hwan Son, **Jung-Bum Kim**. “STACKED ORGANIC LIGHT EMITTING DIODE”, EP2299786, Mar. 26, 2014.
4. Dong-Hoon Lee, Kong Kyeom Kim, Jae Soon Bae, Dae Woong Lee, **Jung-Bum Kim**. “PYRENE DERIVATIVES AND ORGANIC ELECTRONIC DEVICE USING PYRENE DERIVATIVES”, TWI428313, Mar. 1, 2014.
5. Min-Soo Kang, Se-Hwan Son, Hyeon Choi, **Jung-Bum Kim**. “ORGANIC LED AND MANUFACTURING METHOD THEREOF”, US8455896, Jun. 4, 2013.
6. In Ho Hwang, Hyeon Choi, Min Jeoung Lee, Dong-Hoon Lee, Kong Kyeom Kim, Jae Soon Bae, Dae Woong Lee, **Jung-Bum Kim**. “ORGANIC THIN FILM TRANSISTOR”, JP5031584, Jul. 6, 2012.
7. In Ho Hwang, Hyeon Choi, Min Jeoung Lee, Dong-Hoon Lee, Kong Kyeom Kim, Jae Soon Bae, Dae Woong Lee, **Jung-Bum Kim**. “ORGANIC THIN FILM TRANSISTOR”, TWI376807, Nov. 11, 2012.

8. Min-Soo Kang, Jeoung-Kwen Noh, Yun Hye Hahm, **Jung-Bum Kim**, Jong-Seok Kim, Jung-Hyoung Lee. “ORGANIC LIGHT EMITTING DEVICE HAVING IMPROVED LIGHT-EMITTUBG EFFICIENCY AND METHOD FOR FABRICATING THE SAME”, US8253127, Aug. 28, 2012.
9. Jung-Hyung Lee, **Jung-Bum Kim**. “FABRICATION METHOD FOR ORGANIC ELECTRONIC DEVICE AND ORGANIC ELECTRONIC DEVICE FABRICATED BY THE SAME METHOD”, US8338223, Dec. 25, 2012.
10. Jae Seung Lee, Jung-Hyung Lee, **Jung-Bum Kim**. “ORGANIC LIGHT EMITTING DIODE AND METHOD FOR PREPARING THEREOF”, CN101496192, Apr. 25, 2012.
11. Jung-Hyung Lee, **Jung-Bum Kim**. “FABRICATION METHOD FOR ORGANIC ELECTRONIC DEVICE AND ORGANIC ELECTRONIC DEVICE FABRICATED BY THE SAME METHOD”, JP4908583, Jan. 20, 2012.
12. Jung-Hyung Lee, **Jung-Bum Kim**. “FABRICATION METHOD FOR ORGANIC ELECTRONIC DEVICE AND ORGANIC ELECTRONIC DEVICE FABRICATED BY THE SAME METHOD”, EP1996672, Nov. 21, 2012.
13. Jung-Hyung Lee, **Jung-Bum Kim**. “FABRICATION METHOD FOR ORGANIC ELECTRONIC DEVICE AND ORGANIC ELECTRONIC DEVICE FABRICATED BY THE SAME METHOD”, CN101405366, Aug. 29, 2012.
14. Jung-Hyung Lee, **Jung-Bum Kim**. “FABRICATION METHOD FOR ORGANIC ELECTRONIC DEVICE AND ORGANIC ELECTRONIC DEVICE FABRICATED BY THE SAME METHOD”, JP4837774, Oct. 7, 2011.

15. Jung-Hyung Lee, **Jung-Bum Kim**, Yun Hye Hahm. “FABRICATION METHOD FOR ORGANIC LIGHT EMITTING DEVICE AND ORGANIC LIGHT EMITTING DEVICE FABRICATED BY THE SAME METHOD”, CN101379885, Jan. 26, 2011.
16. Min-Soo Kang, Jeung-Kwen Noh, Yun Hye Hahm, **Jung-Bum Kim**, Jong-Seok Kim, Jung-Hyoung Lee. “ORGANIC LIGHT EMITTING DEVICE HAVING IMPROVED LIGHT-EMITTING EFFICIENCY AND METHOD FOR FABRICATING THE SAME”, CN101606436, Jun. 8, 2011.
17. Jung-Hyung Lee, Jae Seung Lee, **Jung-Bum Kim**. “METHOD OF MANUFACTURING ORGANIC LIGHT EMITTING DEVICE AND ORGANIC LIGHT EMITTING DEVICE MANUFACTURED BY USING THE METHOD”, US7935977, May. 3, 2011.
18. Dong-Hoon Lee, Kong Kyeom Kim, Jae Soon Bae, Dae Woong Lee, **Jung-Bum Kim**. “PYRENE DERIVATIVES AND ORGANIC ELECTRONIC DEVICE USING PYRENE DERIVATIVES”, JP4987724, May. 11, 2011.
19. In Ho Hwang, Hyeon Choi, Min Jeung Lee, Dong-Hoon Lee, Kong Kyeom Kim, Jae Soon Bae, Dae Woong Lee, **Jung-Bum Kim**. “ORGANIC THIN FILM TRANSISTOR”, CN101107716, Sep. 14, 2011.
20. Jae Seung Lee, **Jung-Bum Kim**, Young Chul Lee. “ORGANIC LIGHT EMITTING DEVICE HAVING SURFACE-TREATED BOTTOM ELECTRODE”, US8054796, Nov. 15, 2011.
21. Jung-Hyung Lee, **Jung-Bum Kim**, Yun Hye Hahm. “FABRICATION METHOD FOR ORGANIC LIGHT EMITTING DEVICE AND ORGANIC LIGHT EMITTING DEVICE FABRICATED BY THE SAME METHOD”, JP4824776, Sep. 16, 2011.

22. Jung-Hyung Lee, **Jung-Bum Kim**, Yun Hye Hahm. “FABRICATION METHOD FOR ORGANIC LIGHT EMITTING DEVICE AND ORGANIC LIGHT EMITTING DEVICE FABRICATED BY THE SAME METHOD”, TWI338393, Mar. 1, 2011.
23. Jung-Hyung Lee, **Jung-Bum Kim**. “FABRICATION METHOD FOR ORGANIC ELECTRONIC DEVICE AND ORGANIC ELECTRONIC DEVICE FABRICATED BY THE SAME METHOD”, CN101438627, Nov. 8, 2010.
24. Jung-Hyung Lee, **Jung-Bum Kim**. “FABRICATION METHOD FOR ORGANIC ELECTRONIC DEVICE AND ORGANIC ELECTRONIC DEVICE FABRICATED BY THE SAME METHOD”, TWI328300, Aug. 1, 2010.
25. Dong-Hoon Lee, Kong Kyeom Kim, Jae Soon Bae, Dae Woong Lee, **Jung-Bum Kim**. “PYRENE DERIVATIVES AND ORGANIC ELECTRONIC DEVICE USING PYRENE DERIVATIVES”, US7745819, Jun. 29, 2010.
26. In Ho Hwang, Hyeon Choi, Min Jeoung Lee, Dong-Hoon Lee, Kong Kyeom Kim, Jae Soon Bae, Dae Woong Lee, **Jung-Bum Kim**. “ORGANIC THIN FILM COMPRISING PYRENE DERIVATIVES”, US 7714323, May. 11, 2010.